



Strongly scattering media in nature:  
From studying light transport properties  
to harnessing natural materials for 3D  
microfabrication

---

Dominic T. Meiers



Strongly scattering media in nature:  
From studying light transport properties  
to harnessing natural materials for 3D  
microfabrication

Dissertation

Dominic T. Meiers

Vom Fachbereich Physik der Rheinland-Pfälzischen  
Technischen Universität Kaiserslautern-Landau zur  
Verleihung des akademischen Grades „Doktor der  
Naturwissenschaften“ genehmigte Dissertation

Betreuer: Prof. Dr. Georg von Freymann

Zweitgutachter: Prof. Dr. Artur Widera

Datum der wissenschaftlichen Aussprache: 01.12.2023

DE-386



# Abstract

Functional structures as well as materials provided by nature have always been a great source of inspiration for new technologies. Adapting and improving the discovered concepts, however, demands a detailed understanding of their working principles, while employing natural materials for fabrication tasks requires suitable functionalization and modification.

In this thesis, the white scales of the beetle *Cyphochilus* are examined in order to reveal unknown aspects of their light transport properties. In addition, the monomer of the material they are made of is utilized for 3D microfabrication.

White beetle scales have been fascinating scientists for more than a decade because they display brilliant whiteness despite their small thickness and the low refractive index contrast. Their optical properties arise from highly efficient light scattering within the disordered intra-scale network structure.

To gain a better understanding of the scattering properties, several previous studies have investigated the light transport and its connection to the structural anisotropy with the aid of diffusion theory. While this framework allows to relate the light scattering to macroscopic transport properties, an accurate determination of the effective refractive index of the structure is required. Due to its simplicity, the Maxwell–Garnett mixing rule is frequently used for this task, although its constraint to particle and feature sizes much smaller than the wavelength is clearly violated for the scales.

To provide a correct calculation of the effective refractive index, here, finite-difference time-domain simulations are used to systematically examine the impact of size effects on the effective refractive index. Deploying this simulation approach, the Maxwell–Garnett mixing rule is shown to break down for large particles. In contrast, it is found that a quadratic polynomial function describes the effective refractive index in close approximation, while its coefficients can be obtained from an empirical linear function. As a result, a simple mixing rule is reported that unambiguously surpasses classical mixing rules when composite media containing large feature sizes are considered. This is important not only for the accurate description of white beetle scales, but also for other turbid media, such as biological tissues in opto-biomedical diagnostics.

Describing light transport by means of diffusion theory moreover neglects any coherent effects, such as interference. Hence, their impact on the generation of brilliant whiteness is currently unknown. To shed a light on their role, spatial- and time-resolved light scattering spectromicroscopy is applied to investigate the scales and a model structure of them based on disordered Bragg stacks. For both structures the occurrence of weakly localized photonic modes, i.e., closed scattering loops, is observed, which is further verified in accompanying simulations. As shown in this thesis, leakage from these random photonic modes contributes at least 20% to the overall reflected light. This reveals the importance of coherent effects for a complete

---

description of the underlying light transport properties; an aspect that is entirely missing in the purely diffusive transport presumed so far. Identifying the importance of weak localization for the generation of brilliant whiteness paves the way to further enhance the design of efficient optical scattering media, an issue that recently drawn great attention.

Unlike their plant-based counterparts, rigid carbohydrates, such as chitin, are currently unavailable for 3D microfabrication via direct laser writing, despite their great significance in the animal kingdom for the construction of functional microstructures. To overcome this gap, the monomeric unit of chitin, N-acetyl-D-glucosamine, is here functionalized to serve as a photo-crosslinkable monomer in a non-hydrogel photoresist. Since all previous photoresists based on animal carbohydrates are in the form of hydrogel formulations, a new group of photoresists is established for direct laser writing.

Moreover, it is exhibited that the sensitization effect, previously used only in the context of UV curing, can be successfully transferred to direct laser writing to increase the maximum writing speed. This effect is based on the beneficial combination of two photoinitiators. In this, one photoinitiator is an efficient crosslinking agent for the monomer used, but a rather poor two-photon absorber. The other photoinitiator (called sensitizer) possesses, conversely, a much higher two-photon absorption coefficient at the applied wavelength but is not well suited as a crosslinking agent. In combination, the energy absorbed by the sensitizer is passed to the photoinitiator, resulting in the formation of radicals needed to start the polymerization. As this greatly increases the rate at which the photoinitiator is radicalized, resists containing a photoinitiator and a sensitizer are shown to outperform resists containing only one of the components. Deploying the sensitization effect in direct laser writing therefore offers a simple way to individually tune the crosslinking ability and the two-photon absorption properties by combining existing compounds, compared to the costly chemical synthesis of novel, customized photoinitiators.

## Kurzfassung

In der Natur vorhandene funktionelle Strukturen sowie Materialien sind seit jeher eine Inspirationsquelle für die Entwicklung neuer Technologien gewesen. Die Adaption und Modifikation der gefundenen Konzepte erfordert jedoch ein genaues Verständnis der zugrundeliegenden Funktionsprinzipien, während natürliche Materialien oftmals funktionalisiert und modifiziert werden müssen, um sie für Fertigungszwecke einsetzen zu können.

In der vorliegenden Dissertation werden die strahlend weißen Schuppen des Käfers *Cyphochilus* hinsichtlich bisher unbekannter Aspekte ihrer Lichttransporteigenschaften untersucht. Darüber hinaus wird die Monomereinheit des Materials, aus dem sie bestehen, funktionalisiert, um das Monomer für die 3D Mikrofabrikation nutzbar zu machen.

Seit über einer Dekade faszinieren die weißen Käferschuppen Wissenschaftler, da sie trotz ihrer geringen Dicke und des kleinen Brechungsindexkontrasts eine strahlend weiße Färbung aufweisen. Diese optische Eigenschaft kommt durch die äußerst effiziente Streuung des Lichts in der ungeordneten Netzwerkstruktur im Inneren der Schuppen zustande.

Um die Streueigenschaften besser zu verstehen, wurde in etlichen, bisherigen Veröffentlichungen der Lichttransport und seine Verbindung zu der strukturellen Anisotropie des Netzwerks mit Hilfe der Lichtdiffusionstheorie untersucht. Dieser Ansatz erlaubt es zwar die Streueigenschaften anhand makroskopischer Transporteigenschaften zu beschreiben, dafür wird aber eine genau Bestimmung des effektiven Brechungsindex der Schuppe benötigt. Für dessen Berechnung wird regelmäßig die Mischregel nach Maxwell-Garnett aufgrund ihrer Einfachheit verwendet. Die Gültigkeit dieser Regel ist allerdings beschränkt auf Partikel beziehungsweise Strukturdetails die viel kleiner als die Wellenlänge des Lichts sind, eine Bedingung, die von den Schuppen nicht erfüllt wird.

Um eine korrekte Berechnung des effektiven Brechungsindex zu ermöglichen, werden in dieser Arbeit Simulationen genutzt, die auf der Methode der Differenzenquotienten im Zeitbereich beruhen und eine systematische Untersuchung des Einflusses von Größeneffekten erlauben. Unter Zuhilfenahme dieser Methode wird gezeigt, dass die Maxwell-Garnett Mischregel in der Tat im Fall großer Partikelgrößen versagt. Im Gegenzug wird allerdings festgestellt, dass eine quadratische Funktion, deren Koeffizienten durch eine empirisch gefundene, lineare Funktion festgelegt werden, in der Lage ist in diesem Regime den effektiven Brechungsindex in guter Näherung zu beschreiben. Demzufolge wird hier eine neue, einfache Mischregel präsentiert, deren Genauigkeit die Genauigkeit etablierter Mischregeln im Fall von Materialien mit großen Strukturdetails klar übertrifft. Neben einer korrekten Beschreibung der Käferschuppen ist diese Formel auch für andere ungeordnete Medien interessant, z.B. bei der Beschreibung von biologischem Gewebe im Zusammenhang mit optischen Diagnostikverfahren.

---

Eine weitere Schwäche der bisherigen Beschreibung des Lichttransport mittels Diffusionstheorie besteht in der Vernachlässigung sämtlicher kohärenter Effekte, beispielsweise Interferenzeffekte, wodurch deren Einfluss auf die Erzeugung der Weißfärbung unbekannt ist. Um die Rolle dieser Effekte zu beleuchten, wird das Streulicht einer Käferschuppe sowie einer Modellstruktur der Käferschuppen, die sich aus ungeordneten Braggspiegeln zusammensetzt, mit Hilfe eines spektro-interferometrischen Experiments orts- und zeitaufgelöst untersucht. Für beide Strukturen wird das Auftreten von schwach lokalisierten, photonischen Moden, d.h. geschlossenen Streupfaden, festgestellt, was durch entsprechende Simulationen zusätzlich bestätigt wird. Ferner wird beobachtet, dass Streuverluste dieser Moden für mindestens 20% des reflektierten Lichts verantwortlich sind. Kohärente Effekte, die im Bild des rein diffusiven Lichttransports völlig vernachlässigt werden, sind folglich unerlässlich für eine vollständige Beschreibung der Transporteigenschaften. Die Identifizierung des Einflusses der schwachen Lokalisation auf das brillante Weiß ebnet damit den Weg für weitere Optimierungen effizienter, optischer Streumedien, ein Forschungsfeld, das in den letzten Jahren stark an Bedeutung gewonnen hat.

Im Gegensatz zu festen, pflanzenbasierten Polysacchariden, stehen feste Polysaccharide tierischen Ursprungs, wie beispielsweise Chitin, bislang nicht für die 3D Mikrofabrikation mittels direktem Laserschreiben zur Verfügung, obwohl sie im Tierreich eine große Rolle als Material zur Erzeugung funktioneller Strukturen einnehmen. Um diese Lücke zu schließen, wird in der vorliegenden Arbeit die Monomereinheit des Chitins, N-acetyl-D-glucosamin, so funktionalisiert, dass sie als vernetzbares Monomer in Photolacken verwendet werden kann, die kein Hydrogel bilden. Da bisherige tierische Polysaccharide immer in Form von Hydrogellacken verwendet wurden, begründen die präsentierten Lacke damit eine neue Materialklasse für das direkte Laserschreiben.

Darüber hinaus wird die erfolgreiche Adaption des sogenannten Sensibilisierungseffekt gezeigt, der bisher nur aus dem Kontext der UV-Belichtung bekannt ist und mit dessen Hilfe die maximale Schreibgeschwindigkeit beim direkte Laserschreiben erhöht werden kann. Dieser Effekt basiert auf der vorteilhaften Kombination zweier Photoinitiatoren, von denen einer das verwendete Monomer effizient vernetzen kann, dabei aber einen relativ kleinen Zwei-Photonen-Absorptionsquerschnitt aufweist. Der zweite auch Sensibilisator genannte Initiator besitzt dagegen einen großen Zwei-Photonen-Absorptionsquerschnitt, ist dafür aber weniger gut geeignet die Polymerisierung zu initialisieren. In Kombination gibt der Sensibilisator die absorbierte Energie an den Photoinitiator ab, der dann wiederum in Radikale zerfällt, die die Polymerisierung starten. Da dadurch die Rate der erzeugten Photoinitiatorradikale deutlich erhöht wird, übertreffen Lacke, die sowohl den Photoinitiator als auch den Sensibilisator enthalten, die Lacke, die nur eine der beiden Komponenten enthalten. Durch Kombination geeigneter Initiatoren ist es daher möglich die Vernetzungsfähigkeit und den Zwei-Photonen-Absorptionsquerschnitt unabhängig voneinander zu optimieren, ohne dass dafür die aufwendige chemische Synthese neuer Photoinitiatoren mit maßgeschneiderten Eigenschaften nötig wird.



# Contents

<b>Abstract</b>	<b>iii</b>
<b>Kurzfassung</b>	<b>v</b>
<b>List of acronyms</b>	<b>ix</b>
<b>1 Introduction</b>	<b>1</b>
<b>2 Theoretical background</b>	<b>5</b>
2.1 Photonic crystals . . . . .	5
2.1.1 Generation of the photonic band structure in 1D . . . . .	6
2.2 Disordered photonic structures . . . . .	9
2.2.1 White beetle scales as a role model for efficient scattering . . .	10
2.2.2 Disordered Bragg stacks model of white beetle scales . . . . .	13
2.3 Light transport and scattering in disordered media . . . . .	17
2.3.1 Radiative transport equation and diffusion theory . . . . .	18
2.3.2 Weak localization and coherent backscattering . . . . .	22
2.3.3 Anderson localization . . . . .	23
2.4 Effective medium theory . . . . .	24
2.4.1 Maxwell–Garnett mixing rule . . . . .	26
2.4.2 Bruggeman mixing rule . . . . .	28
<b>3 Methods</b>	<b>31</b>
3.1 Numerical methods . . . . .	31
3.1.1 Finite-difference time-domain simulations . . . . .	31
3.1.2 Monte Carlo simulations . . . . .	35
3.1.3 Force-biased algorithm for random sphere packing generation .	40
3.2 Experimental methods . . . . .	42
3.2.1 Direct laser writing . . . . .	42
3.2.2 Time-resolved light scattering spectromicroscopy . . . . .	46
3.2.3 Non-linear absorption measurements . . . . .	48

<b>4</b>	<b>Effective refractive index calculation for composite media with large particles</b>	<b>53</b>
4.1	Simulation setup and its validation . . . . .	54
4.2	Derivation of a mixing rule applicable to large particles . . . . .	59
4.3	Limitations of the mixing rule . . . . .	62
4.4	Comparison to other mixing rules and potential applications . . . . .	64
<b>5</b>	<b>Study of weak localization effects on brilliant whiteness generation</b>	<b>67</b>
5.1	Fabrication of the DBS structure . . . . .	67
5.2	Light scattering spectromicroscopy on brilliant white media . . . . .	70
5.3	Numerical investigation of different transport regimes . . . . .	75
5.4	Contribution of distinct transport regimes to the whiteness . . . . .	79
<b>6</b>	<b>Developing of bio-based resists and establishing the sensitization effect for DLW</b>	<b>81</b>
6.1	Chemical functionalization of N-acetyl-D-glucosamine . . . . .	82
6.2	DLW in NAG-based photoresists . . . . .	85
6.3	Identifying appropriate sensitizer–photoinitiator pairs . . . . .	87
6.4	Deploying the sensitization effect for DLW . . . . .	89
<b>7</b>	<b>Outlook</b>	<b>93</b>
7.1	Synthesis of bifunctional cellulose diacetate derivatives . . . . .	94
7.2	DLW in photoinitiator-free cellulose-based resists . . . . .	95
<b>8</b>	<b>Conclusions</b>	<b>99</b>
	<b>References</b>	<b>103</b>
	<b>Publications</b>	<b>123</b>
	<b>Curriculum vitae</b>	<b>127</b>
	<b>Acknowledgements</b>	<b>129</b>

## List of acronyms

<b>ATA</b>	average- $T$ -matrix approximation	<b>DMAP</b>	4-dimethylaminopyridine
<b>BG</b>	Bruggeman	<b>DMF</b>	dimethyl formamide
<b>CCD</b>	charge-coupled device	<b>DMSO</b>	dimethyl sulfoxide
<b>CDA</b>	cellulose diacetate	<b>FDTD</b>	finite-difference time-domain
<b>CPA</b>	coherent potential approximation	<b>FTIR</b>	Fourier transform infrared
<b>DETC</b>	7-diethylamino 3-thenoylcoumarin	<b>ITX</b>	isopropyl thioxanthone
<b>DBS</b>	disordered Bragg stacks	<b>MG</b>	Maxwell–Garnett
<b>DCC</b>	N,N- dicyclohexylcarbodiimide	<b>NAG</b>	N-acetyl-D-glucosamine
<b>DLW</b>	direct laser writing	<b>NMR</b>	nuclear magnetic resonance
		<b>PML</b>	perfectly matched layer
		<b>SEM</b>	scanning electron microscopy



# 1 Introduction

Throughout thousands of years of evolution, mankind has not only drawn inspiration from nature to construct devices that perform increasingly complex tasks but has also found appropriate building materials in nature. While in early times macroscopic structures have been successfully copied and refined, current focus is on investigating, decoding and replicating the functional principles of natural micro- and nanostructures for advanced applications.<sup>1,2</sup> An example of such biomimetic structures are adhesive tapes that are based on dry adhesion via synthetic setae.<sup>3,4</sup> These structures are inspired by natural setae, which are hair-like microstructures found at the toes of geckos that enable geckos to climb even on molecularly flat surfaces.<sup>5</sup>

As modeling natural structures has become more sophisticated over time, the use of natural materials has also drastically changed. For centuries natural materials such as wood have been mainly served as a cheap and potent building material. Nowadays, its fundamental building block, namely cellulose, is utilized for the creation of composite media with superior properties, for example as films exhibiting radiative cooling or as compostable bioplastics.<sup>6–8</sup> Moreover, recent developments enable 3D printing of natural materials such as cellulose on the nano- and microscale,<sup>9</sup> paving the way not only for realistic biomimicries but also for creating new functionalities using natural materials.

While nature provides solutions for designing mechanical, acoustic, chemical, or thermal properties,<sup>1,2</sup> its strategies for tailoring optical properties are of particular interest for a wide range of applications, including displays, coloration, sensors, solar energy harvesting and many more.<sup>10–13</sup> Prominent examples of natural optical systems are structural colors, as those shown in Fig. 1.1 by a selection of various arthropods. Structural coloration arises from light scattering, refraction, diffraction, and interference in nanophotonic structures, in contrast to pigmentation, which is based on selective absorption.<sup>14</sup>

The first correct presumptions about the fundamental principle underlying chromatic structural colors, for instance exhibited by different butterflies, beetles and spiders (Fig. 1.1a–e), have been made almost 400 years ago.<sup>15</sup> In contrast, unveiling the physics behind the generation of brilliant whiteness (cf. Fig. 1.1f,g) started barely more than a decade ago with studying the beetle *Cyphochilus*, shown in Fig. 1.1g.<sup>16</sup>

While structures exhibiting chromatic colors usually involve optimization only for a small wavelength range, light of all wavelengths must lose its directional information due to multiple scattering in order to create an angle-independent, bright whiteness.<sup>17</sup> This requires sufficiently long optical path lengths, which can be either reached in thick samples or with high refractive index materials.<sup>18,19</sup> With a total thickness of only a few wavelengths, *Cyphochilus* scales, however, manage to achieve a comparable whiteness by efficient light scattering in the disordered intra-scale network structure made of chitin, i.e., a low refractive index material.<sup>16</sup>

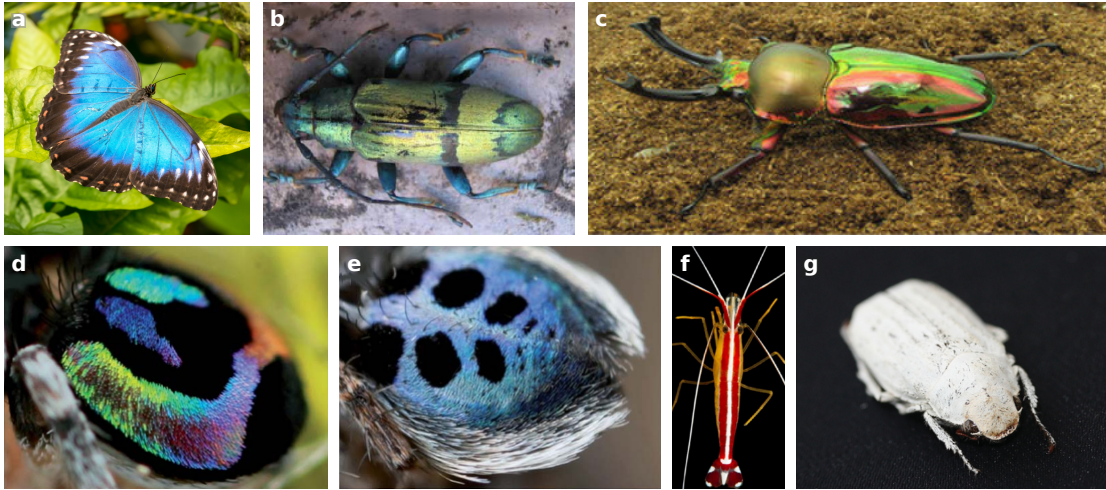


Figure 1.1: Photographs of arthropods exhibiting various structural coloration. **a**, *Morpho* butterfly (*Morpho peleides*) showing an angle-independent brilliant blue coloration. **b**, Longhorn beetle (*Tmesisternus isabellae*) exhibiting a golden color in the dry state that changes upon wetting. Adapted from Ref. <sup>31</sup> **c**, Rainbow stag beetle (*Phalacrognathus muelleri*) revealing a noticeably iridescent appearance, which gives rise to its common name. Taken from Ref. <sup>32</sup> **d,e** Two different peacock spiders displaying an iridescent coloration (*Maratus robinsoni*, **d**) or an angle-independent blue coloration (*Maratus nigromaculatus*, **e**). Adapted from Ref. <sup>33</sup> **f,g**, Beside chromatic appearance, brilliant whiteness can also originate from light scattering in nanostructures as revealed by the Pacific cleaner shrimp (*Lysmata amboinensis*, **f**) and white scarab beetles (*Cyphochilus insulanus*, **g**). (**f**) is adapted from Ref. <sup>17</sup> and (**g**) is adapted from Ref. <sup>22</sup>

Since its first description, understanding the details of light scattering and transport in this complex intra-scale network attracted the interest of several researchers,<sup>20–30</sup> as scattering optimization is important in many of the applications mentioned above. In addition, the fabrication of white, nonhazardous materials is crucial to replace harmful whiting agents such as  $\text{TiO}_2$ , especially since its use as a food additive has been prohibited in the European Union.<sup>17</sup>

To uncover how the optical properties originate from structural characteristics such as the anisotropy of the disordered network, many studies use the framework of light diffusion.<sup>21,22,26,28–30</sup> While this approach allows to determine useful quantities such as macroscopic transport properties, it also possesses some weak points, which are addressed in this thesis.

The description of light transport as a diffusive process assumes the underlying heterogeneous medium to behave as an effective medium quantified by an effective refractive index.<sup>34</sup> While several mixing rules are presented in the literature that enable the calculation of an effective refractive index, these formulas are in general only valid if the features of the heterogeneous medium are much smaller than the wavelength.<sup>35</sup> In the case of beetle scales, however, the diameter of the network struts can reach a few hundred microns and thus be in the same order of magnitude as the wavelength of visible light.<sup>24</sup>

---

In order to accurately compute the effective refractive index for such structures, a new mixing rule is empirically derived in this thesis, which provides useful results for particle diameters up to three-quarters of the wavelength. For this purpose, finite-difference time-domain (FDTD) simulations are applied to systematically study the influence of size effects on the effective refractive index. While the novel mixing rule is deduced for random sphere packings, it is also shown to deliver reasonable predictions for brilliant white structures. It thereby outperforms established mixing rules, such as the Maxwell–Garnett mixing rule, which is used so far.<sup>21,22,28,29</sup>

Beside the difficulty to determine a suitable effective refractive index to obtain reliable results from diffusion theory, this approach also possesses a fundamental disadvantage, as it neglects coherent light propagation and hence does not include interference effects at all. However, the appearance of coherent backscattering in *Cyphochilus* scales clearly indicates the presence of interference effects,<sup>26</sup> as this effect arises from constructive interference of two counter-propagating waves.<sup>36,37</sup>

For this reason, coherent light transport mechanisms in the beetle scales as well as in a model structure of the scales based on disordered Bragg stacks (DBS), are investigated using time-resolved spectromicroscopy experiments.<sup>38,39</sup> The occurrence of weakly localized photonic modes is thereby identified and leakage from these random photonic modes is shown to considerably contribute to the brilliant whiteness of both structures. To verify the experimental results, fully coherent FDTD simulations are compared to incoherent Monte Carlo simulations, which offers additional insights into intrinsic scattering behavior.

As stated in the beginning, studying natural media is not only worthwhile regarding their functional structures, but also from a materials perspective. Since many functional structures, such as brilliant white beetle scales, possess features on the nano- and micrometer scale, 3D microfabrication of natural materials is of particular interest.

One of the most flexible approaches for realizing three-dimensional structures is the optical lithography technique of direct laser writing (DLW). In this approach, polymerization of the photoresist is initialized by a non-linear process, usually two-photon absorption, that only occurs in regions of high intensity, i.e., in the narrow focus of a femtosecond laser beam. Since this strongly confines the polymerized volume in all three dimensions, nearly arbitrary 3D structures from submicron to centimeter scales can be realized.<sup>40,41</sup> Due to its versatility, DLW finds application in numerous fields where precise control over microscopic features is demanded, for instance, in microfluidics,<sup>42–44</sup> micro-optics,<sup>45–47</sup> life science,<sup>48–50</sup> or biomimetics.<sup>51–53</sup>

Among numerous materials that can be patterned via DLW, there is a wide range of biomaterials, both animal and plant sourced. Animal-based materials, including various proteins<sup>54</sup> and a few carbohydrates such as hyaluronan and chitosan,<sup>55–58</sup> are predominantly applied in hydrogel formulations, yielding soft materials. While soft materials often find application in biomedical tasks, rigid materials play also an important role as building material in the animal kingdom, e.g., chitin. In contrast to

rigid plant-based carbohydrates such as cellulose,<sup>9</sup> rigid animal-based carbohydrates are not yet available for DLW.

Using functionalized N-acetyl-D-glucosamine (NAG), which is the monomeric unit of chitin, a novel photoresist is developed in this thesis. As this resist is a non-hydrogel formulation, a new category of rigid animal-based resists is set up.

While NAG-based resists are shown to be suitable for 3D printing, the attainable printing speeds are rather low. To overcome this problem, it is demonstrated that the sensitization effect known from pigmented UV curing can be successfully transferred to DLW, resulting in a remarkable writing speed enhancement.

In pigmented UV curing, the absorption by the pigments in the lacquer can largely exceed the absorption by the used photoinitiator, leading to an overall slow curing speed. However, adding a second photoinitiator (called sensitizer) that absorbs at a longer wavelength, this shielding effect can be circumvented. Under the condition that the sensitizer is capable to transfer the absorbed energy to the photoinitiator, the photoinitiator can be cleaved in highly reactive radicals without absorbing light by itself.<sup>59</sup>

While no such shielding effect occurs in DLW, since the photoresists used are transparent at the applied wavelength, a mismatch between this wavelength and the two-photon absorption maximum of the desired photoinitiator can result in a similar effect. As shown here, adding a suitable sensitizer that possesses a two-photon absorption maximum close to the wavelength used indeed surpasses (in terms of printing speed) resists containing only a sensitizer or a photoinitiator.

The presented thesis is structured as follows. In Ch. 2, a brief review of light propagation in ordered and disordered structures is given and the previous findings regarding the physics behind white beetle scales are highlighted. In addition, an overview of different classical mixing rules is given.

In Ch. 3, the simulation approaches used in the context of this thesis are reviewed first. Subsequently, the different experimental setups are shown and briefly discussed.

The derivation of a mixing rule for large particles is presented in Ch. 4. The chapter is completed by comparing the new and established mixing rules.

In Ch. 5 different transport regimes occurring in white beetle scales are identified and dissected using spectromicroscopy measurements. In addition, the experimental results are verified using accompanying simulations.

The development of a new photoresist based on the monomeric unit of chitin is shown in Ch. 6. Moreover, the successful utilization of the sensitization effect for DLW is reported.

In Ch. 7, an outlook on potential further research is given. In particular, a route of synthesizing photoinitiator-free bio-based resists is presented and first printing results are displayed. The thesis is closed with concluding the main results in Ch. 8.



## 2 Theoretical background

This chapter is intended to provide the reader with an overview of theoretical concepts needed in the context of this thesis. Besides discussing the fundamentals of ordered and disordered photonic structures, different light scattering and propagation mechanisms in disordered media are highlighted. These are crucial for a detailed analysis of light transport in brilliant white media, such as the *Cyphochilus* scales. In addition, techniques to express the permittivity of a disordered medium as an effective one are reviewed, since the effective permittivity is a basic quantity in the description of diffusive light transport in random media.

### 2.1 Photonic crystals

To understand light propagation and accompanying optical effects in disordered media, it is crucial to discuss the concept of periodic, i.e., ordered, photonic structures at first. A periodic photonic structure also called a photonic crystal is the photonic counterpart of a crystalline solid.<sup>60</sup> In a crystal, electrons are moving in a periodic, electronic potential produced by a lattice of atomic cores.

Solving the Schrödinger equation for an electron in such a periodic potential yields as eigenfunctions the so-called Bloch functions. Thereby, a Bloch function describes a plane wave with a periodically modulated amplitude which possesses the same periodicity as the underlying lattice.<sup>61</sup> The spacing between the corresponding eigenstates is so small that they form continuous bands leading to the well-known electronic band structure. The eigenvalues appear to be periodic in the reciprocal space since the crystal lattice exhibits a translational invariance. Therefore, the description of the band structure can be reduced to the first Brillouin zone without loss of generality.<sup>61</sup>

In analogy to a ‘real’ crystal, a photonic crystal can be created by a periodic arrangement of materials with different permittivity.<sup>60,62,63</sup> As shown below, light waves capable to propagate in such a structure are described by Bloch functions as well. Hence, the corresponding eigenvalues also form bands resulting in a photonic band structure. Tailoring the design of the photonic crystal, and thus of the resulting photonic band structure, provides a mighty tool for manipulating the flow of light in such a structure. It is for example possible to create a complete photonic band gap, so that any light within the frequency range of the band gap is unable to propagate inside the photonic crystal independent of the direction of incidence and polarization.<sup>64,65</sup> Below, the generation of a photonic band structure is discussed for the case of a 1D photonic crystal.

### 2.1.1 Generation of the photonic band structure in 1D

The case of a 1D photonic crystal is considered for two reasons. First, the 1D case is the most intuitive in respect of understanding the formation of bands and band gaps. Second, a 1D photonic crystal, also known as Bragg mirror or Bragg reflector, is the base for a model of brilliant white beetle scales, which is used in Ch. 5 to help investigating different light transport phenomena in such media. The discussion shown below is based on the explanation in Ref. <sup>60</sup>.

A 1D photonic crystal consists in one direction (here:  $z$ -direction) of two alternating layers with different permittivities (cf. Fig. 2.1). The spatial period in  $z$ -direction is presumed to have a value of  $a$  while every layer is infinitely expanded in the  $x$ - and  $y$ -directions. It is assumed that light impinges in the  $z$ -direction, thus only the  $z$ -component of the wave vector  $k$  is unequal to zero. To simplify the notation  $k = k_z$  can be written without introducing confusion. Since the description can be reduced to the first Brillouin zone, only wave numbers in the range of  $-\pi/a < k \leq \pi/a$  have to be considered.

Fig. 2.2 displays the resulting band structure for three different index contrasts and an equal layer thickness of  $a/2$ . In the trivial case both layers are composed of the same material. This is equal to an isotropic medium with an imagined periodicity in the  $z$  direction. The allowed modes in an isotropic medium with permittivity  $\epsilon$  lie along the light line, which is given by

$$\omega(k) = \frac{c_0 k}{\sqrt{\epsilon}}, \quad (2.1)$$

for all wave vectors  $k$ . However, due to the imagined periodicity the description can still be restricted to the first Brillouin zone. In consequence, the light line has to be folded back at the edge of the Brillouin zone as shown in Fig. 2.2, left panel for a

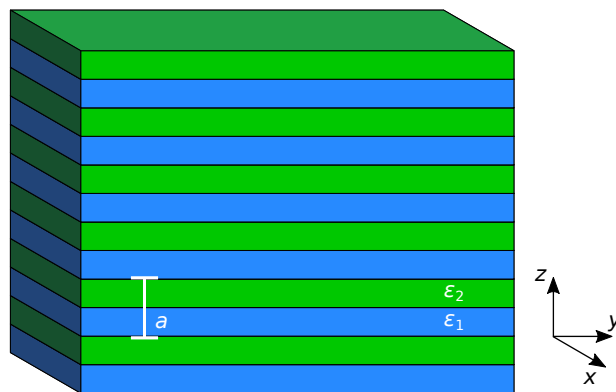


Figure 2.1: Sketch of a 1D photonic crystal consisting of two alternating layers with permittivities  $\epsilon_1$  and  $\epsilon_2$ , respectively. The uniform layers are infinitely expanded in  $x$ - and  $y$ -direction and infinitely stacked in  $z$ -direction with a spatial period of  $a$ .

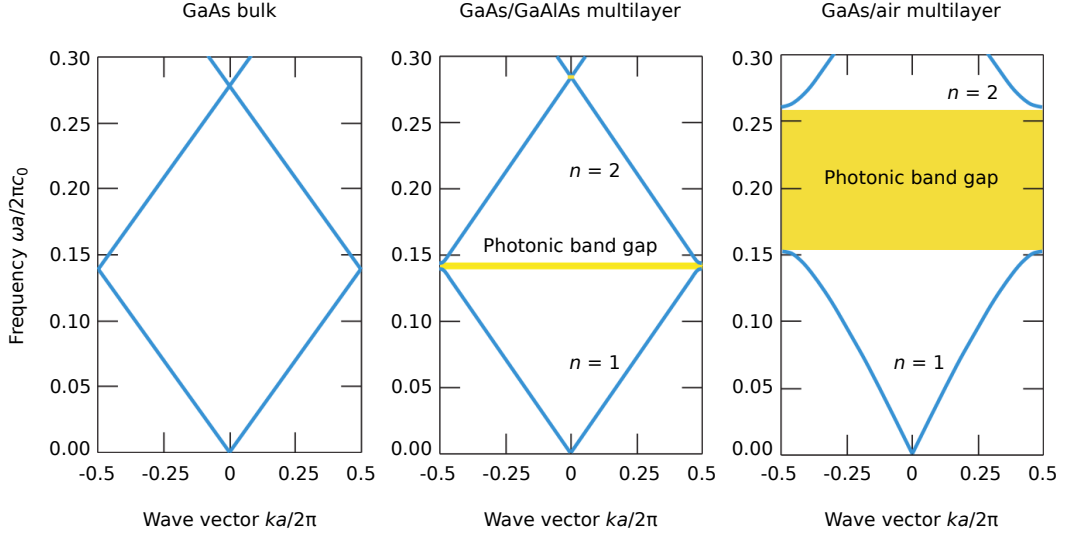


Figure 2.2: Photonic band structures computed for different 1D photonic crystals. The left panel shows a solid block of GaAs ( $\epsilon = 13$ ). The center panel displays a multilayer structure composed of GaAs and GaAlAs layers ( $\epsilon = 12$ ) and the right panel one consisting of GaAs and air layers ( $\epsilon = 1$ ). The layer thickness is  $a/2$  for every layer. Taken from Ref. <sup>60</sup> The figure is excluded from the CC BY license of this thesis.

material with  $\epsilon = 13$ . Thereby, physics is not altered by the introduced periodicity, since the band structure supports the forward and backward propagation of light of any frequency with a group velocity given by the slope of the light line.

While the chosen description seems to be unnecessarily complicated for an isotropic structure, things are different when permittivity contrast starts to increase. For a nearly homogeneous medium with a small permittivity contrast, for example  $\epsilon_2/\epsilon_1 = 13/12$ , as assumed in Fig. 2.2, center panel, the band structure barely deviates from the isotropic case with one exception. Around the cross points of the light lines, frequency regions open up where no allowed modes can be found, independent of the wave vector. Since these regions appear as gaps in the band structure, they are called photonic band gaps.

The generation of band gaps can be understood when the electric field mode profiles of the modes directly below and above the band gap are regarded. For the first photonic band gap displayed in Fig. 2.2, center panel, these modes are at the edge of the Brillouin zone, i.e.,  $k = \pm\pi/a$ . For the corresponding wavelength of  $\lambda = 2a$  two different standing waves can be found which are compatible with the symmetry of the photonic crystal's unit cell. The anti-nodes of the standing wave can either be centered in the region of higher permittivity (Fig. 2.3a) or centered in the region of lower permittivity (Fig. 2.3b). Accordingly, the energy density of the electric field is stronger concentrated in the region of higher or lower permittivity, as revealed in Fig. 2.3c and d, respectively. Thus, both modes observe a different effective permittivity which leads to a splitting of the corresponding frequencies and hence to the photonic band gap.

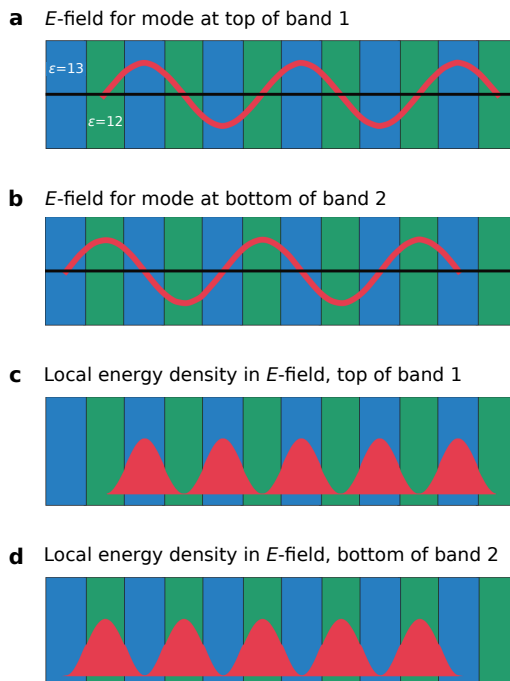


Figure 2.3: Field distribution of different modes in a 1D photonic crystal. **a,b**, Electric field of the Bloch wave obtained for  $k = \pi/a$  at the lower (**a**) and upper edge (**b**) of the first bandgap displayed in Fig. 2.2, center panel. **c,d**, Corresponding local energy density of the electric field at the lower (**c**) and upper edge (**d**) of the first bandgap. Taken from Ref. <sup>60</sup> The figure is excluded from the CC BY license of this thesis.

Since many photonic crystals use a dielectric medium as high and air as low permittivity material, the mode exhibiting a concentration of electric field in the layers with higher permittivity is generally called dielectric mode. This mode is found at the low frequency edge of the band gap, hence the band below the band gap is also referred as dielectric band. At the upper edge of the band gap the air mode (which is also called air mode even if the low permittivity medium is not air) is found. Consequently, the band above the band gap is denoted as air band.

Increasing the permittivity contrast further results in a broader band gap since the bigger difference in the effective permittivities leads to an enlarged frequency splitting. Fig. 2.2, right panel shows this behavior for the case of  $\epsilon_1 = 1$  and  $\epsilon_2 = 13$ .

Beside the permittivity contrast, the thickness of the layers also influences the size of the band gap. For a fixed permittivity contrast, the size of the band gap is maximized when all layers possess an optical thickness of  $\lambda/4$ . In this case the waves which are partially reflected at each layer are all in phase and the ratio between the size  $\Delta\omega$  and the mid-frequency  $\omega_m$  of the first band gap is given by

$$\frac{\Delta\omega}{\omega_m} = \frac{4}{\pi} \sin^{-1} \left( \frac{|\sqrt{\epsilon_1} - \sqrt{\epsilon_2}|}{\sqrt{\epsilon_1} + \sqrt{\epsilon_2}} \right). \quad (2.2)$$

Analyzing the entire band structure of a 1D photonic crystal reveals that in general all consecutive bands are divided by a band gap. The band gaps appear either at the edge of the Brillouin zone, as it can be discerned in Fig. 2.2, center panel for the first band gap or in the middle of the Brillouin zone as it can be seen for the second band gap. In the special case of a  $\lambda/4$ -stack, however, bands are degenerate at  $k = 0$ , so that band gaps only open up at the edge of the Brillouin zone. The mid-frequency of the  $j$ th band gap

$$\omega_{m,j} = \frac{2\pi c_0}{\lambda_j}, \quad (2.3)$$

can then be easily found applying the Bragg condition for a  $\lambda/4$ -stack:

$$\lambda_j = 4n_1d_1/(2j - 1) = 4n_2d_2/(2j - 1), \quad j \in \mathbb{N}, \quad (2.4)$$

where  $d_1$  and  $d_2$  are the thicknesses of the two different layers. It should be further noted that the group velocity, which is given by the slope of the respective band, goes to zero at the edge of a band gap, as it can be also observed in Fig. 2.2. This is in perfect accordance with the expectations because standing waves which are obtained at the edge of the Brillouin zone do not transport any energy.

While in a 1D photonic crystal complete photonic band gaps open up at every permittivity contrast unequal to one, in 2D and 3D photonic crystals complete band gaps (i.e., for all propagation and polarization directions) are only obtained for certain geometries and sufficient permittivity contrasts.<sup>64,65</sup>

## 2.2 Disordered photonic structures

As described in the previous section, a perfectly ordered structure made up of two different dielectric media is a useful tool to form light transport due to the generated photonic band structure. However, to fully unlock the potential of such structures for manipulating the flow of light and hence for various applications, functional defects might be introduced.

For example, altering the optical thickness of one layer in a 1D photonic crystal creates a cavity, which features a defect state within the photonic band gap.<sup>60</sup> Since this defect mode cannot propagate inside the periodic part of the photonic crystal, it is spatially confined around the defect layer leading to a field intensity enhancement, which can be several orders of magnitude. These high fields are deployed, e.g., to build miniaturized optical gas sensors with high sensitivity.<sup>66,67</sup> Introducing a line of defects in a 2D photonic crystal generates a photonic band due to the coupling of many defect states. This band lies within the band gap of the surrounding photonic crystal. Therefore, a so-called coupled resonator optical waveguide (CROW) can be created, which allows to guide light around sharp bends with low losses.<sup>68,69</sup>

While inserting tailored defects in photonic crystals enables new functionalities as exemplified above, the largest part of the structure remains perfectly ordered. In consequence, it is still possible to calculate a photonic band structure which determines the light propagation inside the structure.<sup>60</sup> In contrast, many photonic structures, especially those found in natural systems, deviate from a perfectly ordered system not only at specific sites but possess disorder throughout the entire structure. In such media, the lack of order prevents the definition of a band structure to describe light transport. Therefore, other approaches have to be established, which take multiple scattering processes into account (see Sec. 2.3).

Disordered photonic structures, on the one hand, deliver a potent platform to investigate fundamental physics, especially transport phenomena in the context of different types of disorder, while on the other hand various practical applications are found.<sup>70</sup> Understanding the light propagation inside random media is, for example, crucial to develop imaging and sensing approaches which involve turbid media, such as biological tissue,<sup>71</sup> and hence yielding new opto-biomedical devices.<sup>72–74</sup> Similar applications can be found in other research areas dealing with remote sensing of random and turbid media, e.g., in geoscience, atmospheric science or astrophysics.<sup>75–78</sup> Beyond sensing application, disorder is also applied as a powerful design tool to create sophisticated optical materials for example for random lasing,<sup>79,80</sup> radiative cooling<sup>81,82</sup> or structural coloration.<sup>83–85</sup>

Within the group of structural colors brilliant whiteness takes a special position, because all wavelengths of the visible spectrum have to be randomly scattered at an equal amount. Hence, optically thick structures are required to obtain opacity.<sup>18,19</sup> In white paint formulations, this is commonly achieved by multiple scattering in a random dispersion of particles with high refractive index, e.g., TiO<sub>2</sub> particles.<sup>27</sup> In contrast, nature provides concepts to obtain a similar whiteness in ultrathin structures using solely low refractive index materials. Thereby, highly optimized structures are involved belonging to the strongest scattering structures known, which rely on low refractive index materials.<sup>21</sup>

The most prominent representative, brilliant white scales of the beetle *Cyphochilus*, is reviewed in the next section, since studying the light transport properties of these scales is at the heart of this thesis. The short review is intended to portray the key steps in this research field and to highlight important findings. In addition, a simple model of the white beetle scales is presented, which is deployed in simulations to support the evaluation of different light propagation mechanisms within the scales.

### 2.2.1 White beetle scales as a role model for efficient scattering

In 2007, the beetle *Cyphochilus* was firstly described by Vukusic *et al.* regarding the exceptional brilliance and whiteness of its ultrathin scales.<sup>16</sup> A photograph revealing the whiteness of a *Cyphochilus* beetle is shown in Fig. 2.4a. Using scanning electron microscopy (SEM) of sectioned scales, they found inside the scales a complex net-

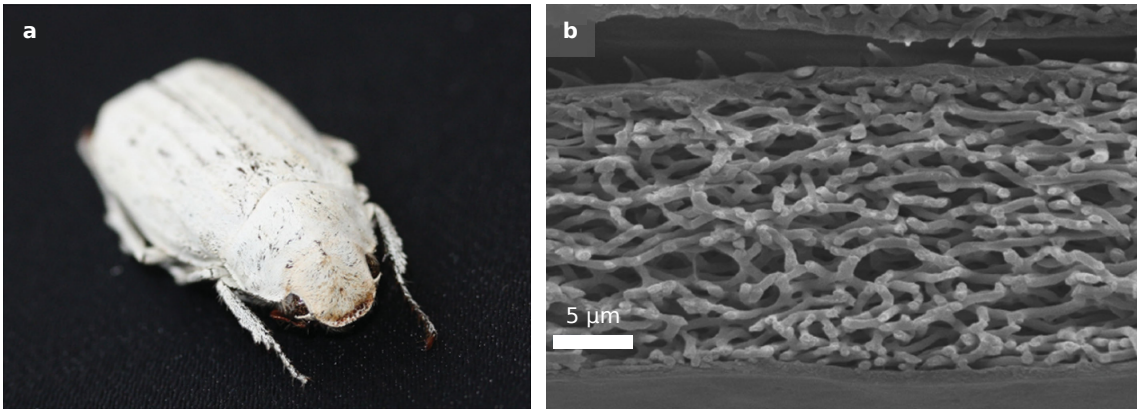


Figure 2.4: **a**, Photograph of a *Cyphochilus* beetle. The about  $250\ \mu\text{m}$  long scales, which cover the beetle's body almost entirely, exhibit the brilliant white coloration. **b**, SEM micrograph of a sectioned single scale, showing the complex intra-scaled network structure composed of chitin fibrils. Adapted from Ref. <sup>22</sup>

work structure composed of chitin fibrils with typical diameters between  $200\ \text{nm}$  and  $250\ \text{nm}$ , as displayed in Fig. 2.4b. Comparing the Fourier transform of this network structure with diffraction patterns obtained from the scales, the network structure has been identified to be responsible for the generation of whiteness.

To answer the question of whether single or multiple scattering processes are predominant in the scales, Burrese *et al.* performed time-of-flight measurements.<sup>21</sup> They recorded the time profile of femtosecond laser pulses after propagation through a scale, revealing a significant temporal broadening of the impinging pulses due to multiple scattering inside the network structure. Thereby, the last part of the pulse tail was found to exponentially decaying with a remarkably long lifetime of  $\tau \approx 140\ \text{fs}$ . In addition, they provided the first estimation of the transport mean free path inside the scales of  $l_t = 1.47\ \mu\text{m}$ , which was calculated applying isotropic diffusion theory.<sup>21</sup>

Since the intra-scale network structure possesses structural anisotropy—the fibrils are predominately oriented in-plane, i.e., perpendicular to the incident direction of light—the same group investigated its influence on the optical properties in a following publication.<sup>22</sup> Using anisotropic diffusion theory, they could indeed show that the network is optimized for scattering in the direction normal to the scale's surface at the cost of a weaker scattering perpendicular to this direction. In this study the respective transport mean free path was calculated to lie between  $0.9$  and  $1.6\ \mu\text{m}$ , showing that the network belongs to the strongest scattering structures made from low refractive index materials.<sup>21,22</sup>

From a today's point of view, however, the provided values are questionable since the first papers assumed filling fractions of the chitin network in the range between  $60\%$  and  $70\%$  as well as scale thicknesses between  $5$  to  $7\ \mu\text{m}$ .<sup>16,21,22</sup> These are in clear contrast to more recent estimations of around  $30\%$  filling fraction and roughly  $12\ \mu\text{m}$  thickness.<sup>27,28</sup> Most likely these discrepancies arise from different preparation

methods. Various drying procedures of the scales prior to measurement might lead to substantial shrinkage effects and hence to a densification of the network structure with accordingly higher filling fractions and smaller scale thicknesses. However, the main influence may be caused by sectioning of the scales. Sectioning procedures such as focused ion beam milling can lead to severe deformation of the scales and their inner network due to the release of mechanical stress when the outer shell of the scale is cut open, as demonstrated by Burg *et al.*<sup>27</sup> Thus, a 3D X-ray computed tomography scan of an intact scale<sup>27</sup> delivers more reliable results than estimations based on 2D SEM images of sectioned scales.<sup>16,21,22</sup> In consequence, using the exact filling fraction beside a more accurate anisotropic light diffusion theory, Lee *et al.* recently reported an effective transport mean free path of  $l_t = 1.85 \mu\text{m}$ .<sup>28</sup> This value is larger than previous calculations but still exceptionally small for low refractive index scattering structures.

To achieve these outstanding scattering properties, the network structure has been evolutionarily optimized, as concluded by Wilts *et al.*<sup>24</sup> Using ptychographic X-ray computed tomography of a sectioned scale, they provided the first 3D computer model of the inner network structure, which was used to study the influence of the network's morphology on the optical properties. The conducted FDTD simulations have confirmed the anisotropy of light transport inside the network, yielding a peak reflectance of around 65% for normal incidence in contrast to roughly 50% peak reflectance perpendicular to the normal direction. In addition, they investigated various stretching and scaling of the entire network as well as changing the filling fraction by adjusting the thickness of the fibrils. This resulted in only minor improvements of the reflectance at the expense of increasing size or weight of the scales. This is detrimental to flying insects and thus reveals the high degree of optimization of the scales.

While structural properties of the intra-scale network and their impact on optical properties were intensively studied, a basic model structure gaining insight into the underlying functional principle was still missing. Using the 3D data provided by Wilts *et al.*,<sup>24</sup> we developed such a model, which is based on Bragg stacks with tailored disorder in respect of the layer thickness and distribution (see Sec. 2.2.2).<sup>25</sup> This disordered Bragg stacks (DBS) model is capable to fully reproduce the optical properties of the complex network structure in the visible spectral range, while it retains a simple structure defined by a small set of parameters. With the help of this model, it was proven that structures exhibiting brilliant chromatic coloration, e.g., those found in various *Morpho* butterflies, are divided from strongly scattering, white structures just by the amount of disorder, as originally speculated by Vukusic *et al.* in the first publication.<sup>16</sup>

Subsequently, different other model structures were presented which were intended to not merely model the *Cyphochilus* scales, but to investigate strongly scattering, low refractive index structures in general. In 2D simulations, Jacucci *et al.* used spherical and elliptical particles with different aspect ratios to study the influence of



form and structural anisotropy independently.<sup>86</sup> They found that elongated particles, which are preferentially oriented in-plane, show a significant better performance than systems based on isotropic particles.

Studying 3D structures composed of cylindrical rods that are placed along the steps of a random walk, Utel *et al.* revealed as well that in-plane orientation of the rods maximizes the reflectance.<sup>19</sup> Moreover, both studies showed that a filling fraction in the range of 30–40% yields the highest integrated reflectance, which is in agreement with the filling fraction featured by the scales' network structure. In both cases, however, it was shown that the proposed structures can be designed to even exceed the reflectance of the white beetle scale. They thus unveiled further potential for whiteness and scattering optimization, once the limitations imposed in natural systems, such as available generation routes, are dropped.

In another publication Jacucci *et al.* reported the first observation of coherent effects in white beetle scales.<sup>26</sup> They measured the scattering of laser light in the backward direction, observing a coherent backscattering cone, which is a typical feature of weak localization (cf. Sec. 2.3.2).

Burg *et al.* addressed the question how *Cyphochilus* scales' structure evolves *in vivo* by comparing them to spinodal structures.<sup>27</sup> Due to the similarity between both structure types, they concluded that liquid–liquid phase separation via spinodal decomposition is most likely the underlying generation process. However, Lee *et al.* found that the surface free energy is not minimized in the case of the intra-scale structure as it would be expected for a late-stage spinodal decomposition.<sup>29</sup> Instead, a similar process is assumed, which results in smooth fibrils at a tenable surface free energy, since the absence of surface irregularities was shown to be favorable for brilliant whiteness in anisotropic structures.

Determination of the exact generation route is indeed a difficult task. Haataja *et al.* have recently shown that brilliant whiteness can be achieved in any disordered system if second order statistical features, such as the correlation length and the filling fraction, as well as anisotropy are properly adjusted.<sup>30</sup> In consequence, many different topologies and thus generation paths could be underlying.

That brilliant whiteness is not limited to a certain topology can also be seen from various artificial structures, which were fabricated through the years. Among others, supercritical CO<sub>2</sub> foaming,<sup>87,88</sup> electrospinning,<sup>89–91</sup> and various phase separation approaches<sup>27,92–94</sup> have been applied, yielding a great variety of different structures, which mimic or even surpass the whiteness of the scales.

### 2.2.2 Disordered Bragg stacks model of white beetle scales

While there are exact digital replicas of *Cyphochilus* scales' inner structure obtained by computed tomography,<sup>24,27</sup> in many situations a simple model is required that enables large scale simulations at low computational cost as well as easy variation of

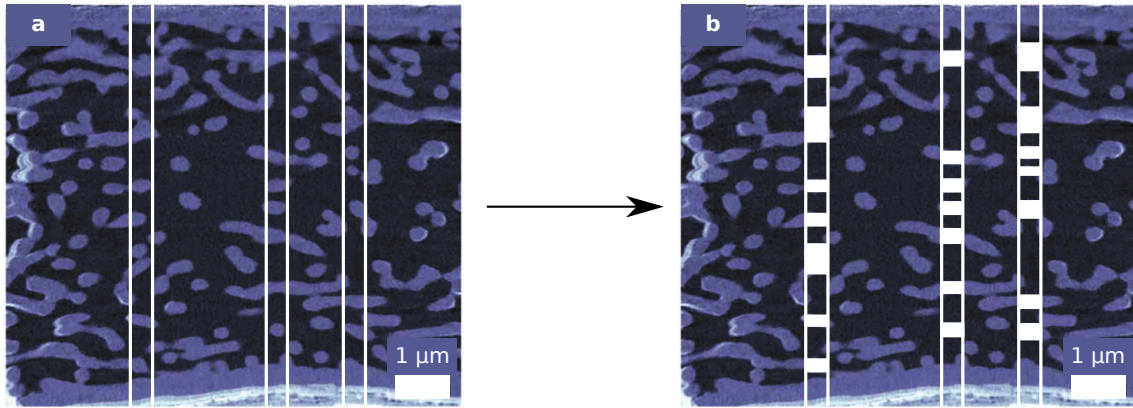


Figure 2.5: Sketch of the basic idea behind the development of the DBS model. **a**, 2D cross section through the 3D tomography scan of a *Cyphochilus* scale provided by Wilts *et al.*<sup>24</sup> The purple regions represent the chitin fibrils, while black regions refer to air. The sections considered in **(b)** are marked by white lines. **b**, Replacing the chitin fibrils with rectangular blocks (white) of the same thickness reveals the layered structure of the intra-scale network. Adapted from Ref.<sup>95</sup>

structural properties. Below, the development of such a model structure is described following the explanations given in Refs.<sup>25,95</sup>

As described in the previous section, it is well known that the intra-scale network features structural anisotropy.<sup>21,22,24,28</sup> The chitin fibrils are preferably directed in-plane, i.e., perpendicular to the normal incidence direction of light, which gives rise to a layer-like structure. Regarding the 2D cross section through the 3D replica of the network in Fig. 2.5a, the layered arrangement of fibrils can be discerned, e.g., in the regions highlighted by the white lines. This becomes even clearer when the fibrils are replaced by simple, rectangular blocks of fitting thickness, as displayed in Fig. 2.5b.

However, the replacement with blocks reveals not only the layered arrangement, but resembles a renowned photonic structure, that is a Bragg stack or 1D photonic crystal, respectively (cf. Sec. 2.1.1). In contrast to a regular Bragg stack two differences can be observed. First, the dielectric layers (i.e., the white blocks) possess different thicknesses instead of a constant one. Second, the distance between consecutive blocks is not constant, as exhibited by the occurrence of partially big gaps in Fig. 2.5b.

Using these findings, the model structure is derived in the following way.<sup>25,95</sup> As a starting point, a Bragg stack is chosen that is composed of chitin and air layers (see Fig. 2.6a, right-hand side). The thickness of the chitin layer is selected to match the mean value of the fibril diameter distribution, which is 230 nm as given by Wilts *et al.*<sup>24</sup> The refractive index of chitin is  $n_{\text{chitin}} = 1.55$ .<sup>96</sup> Accordingly, to construct a  $\lambda/4$ -stack, the thickness of the air layer is set to 357 nm (cf. Eq. (2.4)). As expected for a Bragg stack with these dimensions, the reflectance spectrum reveals a pronounced second order stop band around 475 nm, as shown in Fig. 2.6a. Note that this stop

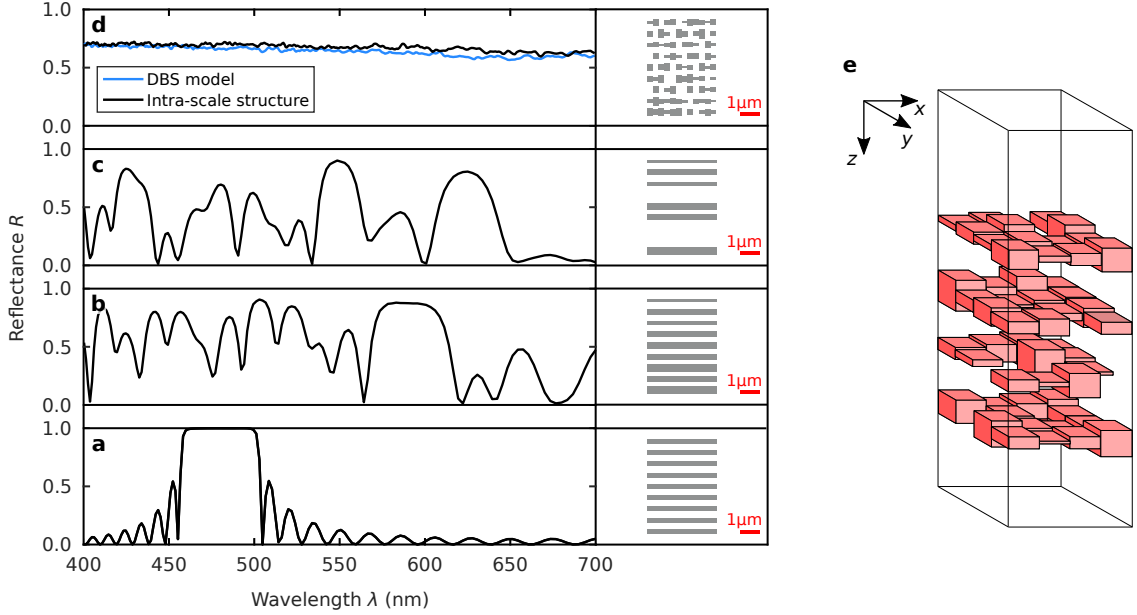


Figure 2.6: Evolution of the DBS model. **a–d**, Each panel displays a 2D sketch of the structure (right) and its corresponding reflectance calculated by FDTD simulation (left), showing a periodic Bragg stack (**a**), a periodic Bragg stack with varying layer thickness (**b**), a periodic Bragg stack with varying layer thickness and randomly omitted layers (**c**), and the final DBS model composed of many different stacks (**d**), which are constructed as presented in (**c**). For comparison, the reflectance obtained for the replica of the intra-scale structure provided by Wilts *et al.*<sup>24</sup> is additionally displayed in (**d**) (blue curve). **e**, 3D sketch of the DBS model structure. Adapted from Ref.<sup>25</sup>

band is referred to as second order because in the case of  $\lambda/4$ -stacks stop bands only open up at the edge of the Brillouin zone, as explained in Sec. 2.1.1.

While the Bragg stack reaches a high reflectance, its range is limited to certain wavelengths resulting in a chromatic rather than a white appearance. Therefore, in the next step disorder is introduced by varying the thickness of the chitin layers according to the diameter distribution measured by Wilts *et al.*<sup>24</sup> The resulting structure and reflectance spectrum are shown in Fig. 2.6b. Here, a relatively high reflectance can be observed for many different wavelengths inside and outside of the original stop band. The introduced disorder thus leads to a broadening of the stop band at the expense of a lower peak reflectance.

Next, one third of the layers are randomly omitted as displayed in Fig. 2.6c. This is done to account for the partially bigger gaps observed in Fig. 2.5b and to reduce the optical crowding effect. Optical crowding occurs if scattering centers are placed in proximity, leading to an overlap of their radiation fields.<sup>16,18,97</sup> Because of this overlap, a cluster of nearby scattering centers effectively acts as a large, single scattering center with the adverse effect of reduced lateral and backward scattering.<sup>98</sup>

Composing many of such disordered stacks, the final model is obtained (Fig. 2.6d). A 2D sketch is here used for clearness, however, the actual model is a real 3D

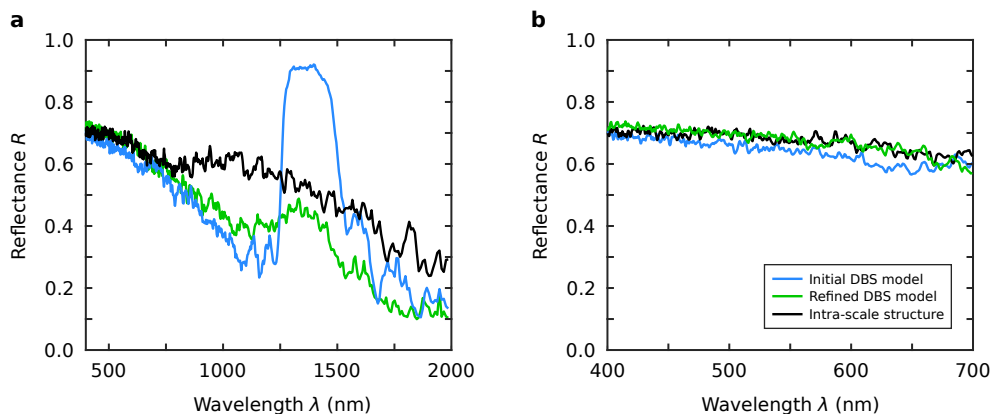


Figure 2.7: Reflectance of different brilliant white scattering media. **a**, Comparison between the initial DBS model (blue curve), the refined DBS model (green curve), and the exact replica of the intra-scale structure (black curve) with respect to their reflectance in the visible and near infrared spectral range. **b**, Close-up view of the visible spectral range shown in **a**. According to Ref. <sup>95</sup>

structure, as presented in Fig. 2.6e. The footprint of each individual stack is chosen to be  $300 \times 300 \text{ nm}^2$ . A subwavelength footprint of individual stacks is needed to achieve sufficient lateral scattering, which is crucial for whiteness. Indeed, disordered Bragg stacks with large footprints are found in nature, which exhibit a reflectance comparable to that of the beetle scales but appear gold or silver in color.<sup>15,99–101</sup> Conversely, the footprint must not be chosen too small, otherwise the onset of optical crowding drastically reduces the reflectance, as shown in Ref. <sup>95</sup>

Using a proper footprint of the stacks, the reflectance of the DBS model in the visible spectral range is in perfect agreement with the reflectance obtained from the exact replica of the intra-scale structure, as shown in Fig. 2.6d. In addition, great conformance is also found for other optical properties like the intensity distribution in the far field or the time-of-flight, demonstrating that the proposed DBS structure can fully model the optical properties of the beetle scales in the visible spectral range.<sup>25</sup>

Nevertheless, some differences are found in the near infrared range as revealed in Fig. 2.7a. As stated above, the Bragg stack underlying the DBS model possesses a second order stop band in the visible spectral range, which broadens when disorder is introduced. In contrast, the first order stop band which lies around 1400 nm is more robust in respect of disorder, largely preserving a stop band in the near infrared. In this wavelength range, however, the reflectance of the intra-scale network structure exhibits a broader feature rather than a distinct stop band.

To account for this, the DBS model can be refined by adopting further disorder. So far, the center-to-center distance between consecutive chitin layers is kept constant, so that only the omission of layers leads to positional disorder. Therefore, additional positional disorder is implemented using a normal distributed center-to-center distances instead of a constant one, yielding the refined model (for model parameter see

Ref. <sup>25</sup>). As displayed in Fig. 2.7a (green line), the stop band in the near infrared is mostly diminished in comparison to the initial DBS model (blue line), being closer to the behavior shown by the intra-scale network structure (black line). Nevertheless, there is still a discrepancy especially in the range around 1000 nm. The deviations might arise from the fact, that the DBS model is a strictly layered structure without any interconnection between the layers, while the network structure also possesses struts which are oriented out-of-plane. With a mean length around  $1\ \mu\text{m}$ ,<sup>24</sup> these struts may lead to optical features in the near infrared, which cannot be captured by the DBS model.

However, in the visible spectral range, which is of main interest, the refined model mimics the reflectance of the beetle scales with barely any difference at all, even slightly outperforming the initial model (cf. Fig. 2.7b). It hence can be used to support the investigation and dissection of different light transport mechanisms in white beetle scales. An overview of various light propagation mechanisms in strongly scattering media is provided in the next section.

## 2.3 Light transport and scattering in disordered media

To describe light transport in disordered photonic media, the concept of photonic band structure cannot be used because of the absence of a strict periodicity. Instead, to obtain an exact solution, Maxwell's equations have to be solved while considering the microscopic nature of the disordered medium.<sup>102–106</sup> Since Maxwell's equations fully include the wave character of electromagnetic radiation, this is the most rigorous approach because all kinds of interference effects are preserved. Analytic solutions, however, can be given only in a very limited number of scenarios due to the high complexity of the problem for an arbitrary random medium.<sup>106</sup>

Thus, in most cases numerical approaches such as the FDTD (see Sec. 3.1.1), the pseudospectral time-domain<sup>107,108</sup> or the superposition  $T$ -matrix method<sup>109,110</sup> are applied to solve Maxwell's equations and calculate light propagation in random media. A drawback of all methods is the strong increase of required memory and computational time with growing sample volume or number of scattering particles, respectively.<sup>110,111</sup> This generally inhibits their application to problems where the feature or sample size is orders of magnitudes larger than the wavelength of the incident light.<sup>112</sup>

To deal with large, disordered media too, a common strategy is to discard the wave character of electromagnetic radiation and to consider the transport of power through the random medium instead.<sup>105,106</sup> In the corresponding transport theory, the (scalar) radiative transfer or radiative transport equation is used to describe the light propagation in the medium. While the radiative transport equation can be analytically solved in some cases, it is often more convenient to use diffusion theory, which is an approximation of the radiative transport equation, or numerical methods such as Monte Carlo simulations (see Sec. 3.1.2).<sup>112</sup>

Although interference effects are not natively included in the radiative transport equation and diffusion theory, their predictions suffice to describe light transport in disordered media in many practical cases.<sup>102,113–115</sup> Using diffusion theory with gain, it is even possible to model certain aspects of random lasing in agreement with experimental observations. The validity of such a description, however, strongly depends on whether interference effects are sufficiently averaged out and thus on the experimental setup, e.g., usage of long excitation pulses or averaging over multiple laser shots.<sup>80</sup>

In contrast, if interference effects cannot be neglected, the scalar radiative transport equation and diffusion theory fail to calculate light transport correctly. In this case the basic concept has to be extended to take wave properties such as polarization into account, resulting in the vector radiative transport equation.<sup>106</sup> Applying techniques like electric field Monte Carlo simulations, the propagation of polarized light in disordered media can be calculated.<sup>116</sup> Since the electric field and phase is traced in this approach, coherent properties are preserved and interference effects such as speckle pattern or coherent backscattering are directly obtained.<sup>112,116,117</sup> However, recording the photon pathway and the entry and exit point on the entrance facet of the sample, the coherent backscattering cone can be also reconstructed from the results of scalar theories and simulations, respectively.<sup>26,118</sup>

Since the radiative transport equation is an important and frequently used tool for describing light transport in disordered media, its concept and in particular its approximation, namely diffusion theory, will be elucidated in the next section. Subsequently, different mechanisms of light localization are discussed, which can become crucial for light scattering and transport in random media while not being captured by original radiative transport equation and diffusion theory.

### 2.3.1 Radiative transport equation and diffusion theory

The transport theory of light is a heuristic theory which relies on the transport of power through a random medium.<sup>102,105,106</sup> In transport theory, the radiance  $I(\mathbf{r}, \hat{\mathbf{s}})$  is considered as the base quantity. Assuming an excitation source with a narrow bandwidth, such as a laser, and a detector with a sufficient bandwidth, the radiance is the average flux density at the point  $\mathbf{r}$  within a unit solid angle around the direction  $\hat{\mathbf{s}}$  (with unit  $\text{Wm}^{-2} \text{sr}^{-1}$ ).<sup>106</sup>

The radiance in the random medium must satisfy the transport equation. The radiative transport equation states that the change of radiance in direction  $\hat{\mathbf{s}}$  is given by the decrease of radiance because of absorption and scattering out of direction  $\hat{\mathbf{s}}$  and the increase of radiance due to light which is scattered from other directions  $\hat{\mathbf{s}}'$  into direction  $\hat{\mathbf{s}}$ . Mathematically this is described by<sup>119</sup>

$$\hat{\mathbf{s}} \cdot \nabla I(\mathbf{r}, \hat{\mathbf{s}}) = -\gamma_{\text{ext}} I(\mathbf{r}, \hat{\mathbf{s}}) + \frac{\gamma_{\text{s}}}{4\pi} \int p(\hat{\mathbf{s}}, \hat{\mathbf{s}}') I(\mathbf{r}, \hat{\mathbf{s}}') d\omega'. \quad (2.5)$$

Here,  $\gamma_{\text{ext}} = \gamma_{\text{s}} + \gamma_{\text{a}}$  is the extinction coefficient with  $\gamma_{\text{s}}$  and  $\gamma_{\text{a}}$  being the scattering and absorption coefficients, respectively,  $p(\hat{\mathbf{s}}, \hat{\mathbf{s}}')$  is the phase function and  $d\omega'$  is the differential solid angle around the direction  $\hat{\mathbf{s}}'$ . Instead of the coefficients, the corresponding mean free paths are often given such as the scattering mean free path  $l_{\text{s}} = \gamma_{\text{s}}^{-1}$  and so forth.

If the phase function is normalized

$$\int_{4\pi} p(\hat{\mathbf{s}}, \hat{\mathbf{s}}') d\omega' = 1, \quad (2.6)$$

it represents the probability density function for scattering from direction  $\hat{\mathbf{s}}'$  to direction  $\hat{\mathbf{s}}$ ,<sup>119</sup> i.e., the scattering characteristic of the medium is embodied in the phase function.<sup>102,106</sup> In case of symmetric scattering about the incident direction, the phase function only depends on the angle  $\theta$  between  $\hat{\mathbf{s}}$  and  $\hat{\mathbf{s}}'$ . In many practical cases the Henyey–Greenstein formula, which was originally developed to describe diffusive interstellar radiation,<sup>120</sup> is a suitable approximation for the phase function:

$$p(\theta) = \frac{W_0(1 - g^2)}{(1 + g^2 - 2g \cos \theta)^{3/2}}, \quad (2.7)$$

with the albedo  $W_0 = \gamma_{\text{s}}/\gamma_{\text{ext}}$  and the anisotropy factor  $g = \langle \cos \theta \rangle$ .<sup>106</sup> In general, the anisotropy factor lies between -1 and 1, where the three special cases  $g = 0$ ,  $g = -1$ , and  $g = 1$  represent isotropic scattering, pure backward scattering, and pure forward scattering, respectively.<sup>113,119,120</sup> For most scatterers, however, the anisotropy factor is greater than 0,<sup>113</sup> hence the scattering is more pronounced in the forward direction (see for example Table III in Ref.<sup>119</sup> for an overview of various biological tissues). The albedo can take values between 0 and 1, ranging from an entirely absorbing to a purely scattering medium.

In the common scenario of using a laser as light source, the radiance  $I = I_{\text{c}} + I_{\text{d}}$  within the random medium can be divided into the coherent radiance  $I_{\text{c}}$  and the diffusive radiance  $I_{\text{d}}$ .<sup>106</sup> In that, the coherent radiance is the undeflected incident radiance attenuated by scattering and absorption losses, i.e., it satisfies Beer's law.<sup>119</sup> It is important to note that the term *coherent* here refers to the propagation of a beam from a coherent light source but does not imply that coherent effects are captured (since they are not included at all in the radiative transport equation). The diffusive radiance contains the light which is scattered out of the original beam direction. It can be exactly described with an infinite sum of Legendre polynomials.<sup>119</sup>

Depending on the albedo two different approximations can be made. For a small albedo ( $W_0 < 0.5$  for a plane wave,  $W_0 < 0.9$  for a narrow beam) the absorption predominates over scattering, thus the coherent radiance is much larger than the diffusive radiance.<sup>106</sup> In consequence, the total radiance can be approximated by the coherent radiance and the first-order scattering solution can be used (see e.g. Ref.<sup>102</sup> for details). In contrast, for an albedo close to 1, i.e., a weakly absorbing

medium such as countless biological tissues, the diffusive radiance dominates the total radiance, and the diffusion approximation holds true.

In diffusion theory only the first (isotropic) and second (slight forward directed) term of the sum of Legendre polynomials are considered.<sup>119</sup> Using this approximation, the transport equation (2.5) reduces to the following diffusion equation:

$$(\nabla^2 - \kappa^2)\psi_d(\mathbf{r}) = -\mathbf{Q}(\mathbf{r}), \quad (2.8)$$

with the diffusive radiant fluence rate  $\psi_d(\mathbf{r})$ .<sup>106,119</sup> In general, the radiant fluence rate is the integration of the radiance over all angles:<sup>106</sup>

$$\psi(\mathbf{r}) = \int_{4\pi} I(\mathbf{r}, \hat{\mathbf{s}}) d\omega. \quad (2.9)$$

In the diffusive regime, where scattering dominates absorption, the actual effective attenuation coefficient is approximated by the constant  $\kappa$  with

$$\kappa^2 = 3\gamma_a(\gamma_s(1 - g) + \gamma_a), \quad (2.10)$$

while the source term in Eq. (2.8) is given by

$$\mathbf{Q}(\mathbf{r}) = 3\gamma_s(\gamma_{\text{ext}} + g\gamma_a)\mathbf{F}_0(\mathbf{r}) \exp(-\tau), \quad (2.11)$$

with the incident irradiance or radiant flux density  $\mathbf{F}_0(\mathbf{r})$ .<sup>106,119</sup> The irradiance is generally calculated via

$$\mathbf{F}(\mathbf{r}) = \int_{4\pi} I(\mathbf{r}, \hat{\mathbf{s}}) \hat{\mathbf{s}} d\omega. \quad (2.12)$$

The optical depth  $\tau$  is given by

$$\tau = \int_0^l \gamma_{\text{ext}} dl, \quad (2.13)$$

where  $l$  is the distance along the propagation direction of the incident beam from the input facet to the point  $\mathbf{r}$  within the random medium.

So far only time-independent (steady-state) transport of light was considered. Regarding the propagation of a light pulse  $\psi(\mathbf{r}, t)$  through the random medium, the pulse can be split into a coherent and diffusive portion too. During propagation of the coherent pulse, light is scattered which creates the diffusive pulse  $\psi_d(\mathbf{r}, t)$ . The diffusive pulse satisfies the equation:

$$\left(\nabla^2 - \frac{3}{v_e^2} \frac{\partial^2}{\partial t^2} - \frac{1}{D} \frac{\partial}{\partial t} + \kappa^2\right)\psi_d(\mathbf{r}, t) = 0, \quad (2.14)$$

with the diffusion coefficient or diffusivity  $D$ .<sup>106</sup>



To classify light transport in random media, it is convenient to introduce the transport mean free path  $l_t$  which is defined as<sup>113</sup>

$$l_t = \frac{l_s}{1 - g}. \quad (2.15)$$

The transport mean free path is the distance which must be traveled by light until all information about its incident direction is lost. For isotropic scattering ( $g = 0$ ) this is the case after the first scattering event, hence the transport mean free path equals the scattering mean free path as it can be directly seen from Eq. (2.15). For forward scattering ( $g > 0$ ), however, several scattering events are needed resulting in a transport mean free path which is larger than the scattering mean free path (with the limit  $l_t \rightarrow \infty$  for  $g = 1$ ).

Moreover, the transport mean free path is directly related to the diffusivity, linking the properties of steady-state and dynamic transport of light via

$$D = \frac{1}{3}v_e l_t, \quad (2.16)$$

where  $v_e$  is the (energy) transport velocity.<sup>121</sup> In absence of resonance scattering, the transport velocity is approximately obtained as phase velocity  $v_e = c_0/n_{\text{eff}}$ , with the effective refractive index of the medium  $n_{\text{eff}}$  (see Sec. 2.4).<sup>21,121,122</sup> Nevertheless, for frequencies in vicinity of scatterers' Mie resonances, the transport velocity can be significantly lower than the phase velocity.<sup>121-123</sup>

Applying appropriate boundary condition (see e.g., Refs.<sup>102,106</sup>) to account for semi-finite or finite samples which possess at least one interface with the ambient medium, the framework presented above can be used to calculate the light diffusion in random media. However, in experiments light propagation inside the random medium is hardly accessible, hence quantities such as the total transmission are more expedient. The total transmission through a slab of random medium with thickness  $L$  is given by

$$T_{\text{tot}} = \exp(-L/l_s) + \frac{(l_t + z_e) - (l_t + z_e + L) \exp(-L/l_s)}{L + 2z_e}, \quad (2.17)$$

with the extrapolation length  $z_e$ .<sup>124</sup> The extrapolation length is calculated according to:

$$z_e = \frac{2l_t}{3} \frac{1 + \bar{R}}{1 - \bar{R}}, \quad (2.18)$$

where  $\bar{R}$  is the reflectance of the interface between random and ambient medium averaged over all possible incident angles.<sup>124</sup> If the ambient medium is air, the reflectance can be calculated using Fresnel's law in combination with the effective refractive index of the random medium,<sup>125</sup> while ambient media with higher refractive index require a more advanced modeling of the boundary reflection.<sup>126</sup>

The term  $\exp(-L/l_s)$  in Eq. (2.17) belongs to the unscattered, ballistic photons passing through the slab. Except for very thin slabs (i.e.,  $L \ll l_t$ ), their portion can be neglected yielding the simple expression:<sup>21,22,124</sup>

$$T_{\text{tot}} = \frac{l_t + z_e}{L + 2z_e}. \quad (2.19)$$

In general Eq. (2.17) and Eq. (2.19) are obtained for isotropic scattering. Nevertheless, it is shown that these equations also pertain for anisotropic scattering with a comparable accuracy than in the isotropic case.<sup>124</sup>

So far only isotropic light transport is considered, which is expected to occur for scattering media without structural anisotropy. Note that isotropic light transport does not exclude scattering anisotropy, but it is characterized by scalar (direction-independent) quantities such as transport mean free path, scattering mean free path, diffusivity and so forth. Hence, to describe anisotropic light transport the scalar quantities are replaced by corresponding tensors and the anisotropic diffusion equation must be solved, as explained in more detail in the literature.<sup>113,127,128</sup> However, replacing the scalar transport mean free path with the appropriate entry of the transport mean free path tensor, the expressions for the total transmittance given above are also valid for anisotropic light transport.<sup>22</sup>

### 2.3.2 Weak localization and coherent backscattering

The phenomenon of weak localization was originally described for electrons multiply scattered by impurities in a semiconductor or metal.<sup>129,130</sup> Since this effect relies on the fundamental concept of reciprocity,<sup>131</sup> it is not limited to electrons but can occur for all kinds of wave in disordered media, for instance electromagnetic waves.<sup>36,37,132</sup> Thereby, weak localization is the most robust interference effect obtained in random media and is usually considered a precursor to Anderson localization, which is briefly discussed in the next section.<sup>131</sup>

Weak localization can be understood in real space regarding the transport from point A to point B through wave packets traveling along different paths.<sup>37,130</sup> The total probability of approaching B from A is given by the square of the sum over the probabilities of all possible paths, i.e., the coherent sum. In that, different paths generally differ in length and thus in phase. This results in averaging out all interference terms and the coherent sum becomes equal to the incoherent sum.<sup>37</sup> However, there is one exception. When A and B coincide, i.e., in the case of closed loops, two contributions are obtained from each path because of two opposite propagation directions. These counter-propagating waves are in phase, hence they interfere constructively. This results in a twice as high probability than in the incoherent case leading to localization.<sup>130</sup>

Usually, weak localization is observed as coherent backscattering, giving rise to a characteristic peak of enhanced intensity around the backscattering direction.<sup>36</sup>

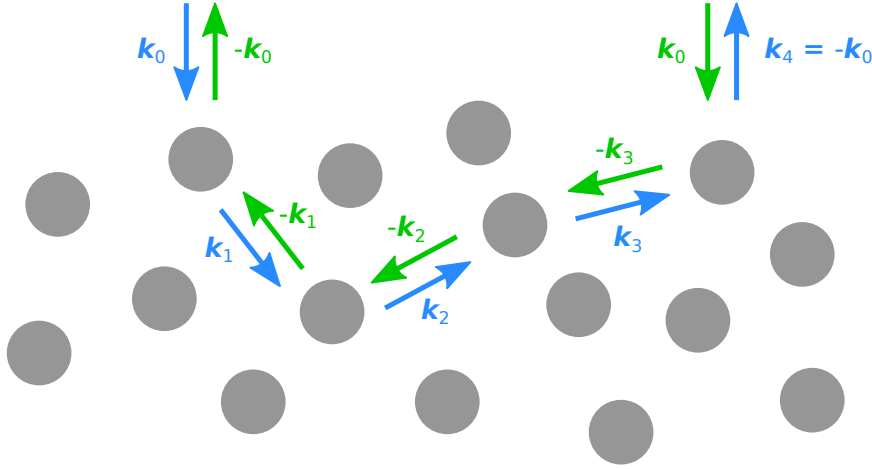


Figure 2.8: Illustration of two counter-propagating waves undergoing  $m = 4$  scattering events in a disordered medium as indicated by their respective wave vectors (blue and green). Due to phase matching between both waves, constructive interference occurs leading to an enhanced intensity in the backscattering direction.

coherent backscattering does not necessarily involve closed loops inside the medium, however, the underlying principle remains the same as explained in the following.

Illuminating the sample with a plane wave with wave vector  $\mathbf{k}_0$ , the wave undergoes  $m$  elastic scattering events represented by the series  $\mathbf{k}_0, \mathbf{k}_1, \mathbf{k}_2, \dots, \mathbf{k}_m$ , with  $\mathbf{k}_i$  being the wave vector after the  $i$ th scattering event as displayed in Fig. 2.8. For  $\mathbf{k}_m = -\mathbf{k}_0$ , i.e., in the backscattering direction, the wave propagating along the counter-direction  $\mathbf{k}_0, -\mathbf{k}_{m-1}, \dots, -\mathbf{k}_1, \mathbf{k}_m$  is in phase and constructive interference leads to a backscattering intensity which is theoretically twice the incoherent background.<sup>36</sup> In reality, stray light as well as single scattering can reduce the enhancement to a value less than 2.<sup>131</sup>

For angular deviations from the backscattering direction, a phase shift between both waves is introduced. If these deviations are sufficiently small, a minor phase shift is obtained such that interference effects are preserved. Hence, the coherent backscattering cone possesses a finite angular width, which is found to be on the order of  $\lambda/l_t$ , revealing the connection between the transport properties of random media and localization effects.<sup>36,37</sup>

### 2.3.3 Anderson localization

As stated in the previous section, weak localization can be seen as a precursor of Anderson localization which is also renowned as strong localization. This connection is based on the fact that Anderson localization also arises from localization in a random medium due to the formation of closed loops.<sup>133</sup> In contrast to weak localization which occurs beside diffusive transport, Anderson localization requires the interference of *all* scattered waves. Therefore, diffusion is completely absent.<sup>37,133</sup>

In consequence, transport comes to an entire halt and a metal-insulator transition is obtained at the onset of Anderson localization in electronic systems.<sup>134</sup>

As in the case of weak localization, the concept of Anderson localization is not limited to electrons but can be transferred to all type of waves.<sup>134</sup> However, a necessary condition to obtain Anderson localization in a random medium is the satisfaction of the (modified) Ioffe-Regel criterion  $kl_t \leq 1$ ,<sup>135</sup> i.e., the transport mean free path must be smaller than the wavelength. For light, this condition is very tough to achieve in 3D systems since absorption-free, strongly scattering media composed of high refractive index materials are required.<sup>134</sup> Indeed, several potential measurements of 3D Anderson localization of light are reported,<sup>135–137</sup> which later turned out not to be loophole-free,<sup>138,139</sup> remaining the challenge up to this day. In lower dimensional systems, however, Anderson localization of light could be already shown.<sup>140–142</sup>

## 2.4 Effective medium theory

The treatment of light propagation in disordered media completely on a microscopic scale becomes a virtually impossible task as soon as the sample size significantly exceeds the wavelength as discussed in Sec. 2.3. Instead, at a sufficient sample size the light ‘sees’ many different microscopic arrangements, so that its transport is rather affected by averaged quantities than specific local configurations. This enables to describe light transport using macroscopic quantities, e.g., by means of diffusion theory.<sup>113</sup> In that, the transport between two consecutive scattering events—note that the average distance is given by the macroscopic scattering mean free path—is characterized by the propagation in a homogeneous medium possessing an average or effective refractive index.<sup>34,121,122</sup>

While diffusion theory is a simple, yet elegant and efficient way to describe light transport in many random scattering media, the evaluation of appropriate macroscopic material properties can be complicated. In fact, a homogenization approach is needed which allows to describe the actual heterogeneous medium with its spatially varying permittivity as a homogeneous one owing an effective permittivity.<sup>143</sup> Such an approach must take at least the permittivities as well as the volume fractions of all constituents into account. However, for arbitrarily complex composite media, for example metamaterials, microscopic details such as the shape and size of individual scatterers might be considered too.

Because composite media with feature sizes on the scale of the wavelength are abundant, e.g., in nature,<sup>2,123</sup> evaluating an appropriate effective permittivity has attracted researchers’ interest for more than a century.<sup>144</sup> Thereby, numerous methods have been proposed over the years. The most approaches, however, rely on one of two fundamental concepts of homogenization, which are also deployed in the description of the electronic structure of alloys.<sup>145</sup> Hence, it is convenient to categorize different methods by their relation to the counterpart in alloy theory.<sup>144,146</sup>

The first class contains methods which are related to the average- $T$ -matrix approximation (ATA).<sup>147,148</sup> These approaches assume small inclusions being dispersed in a host matrix, i.e., in a homogeneous background. In that, the permittivity is taken as the sum of the permittivity of the background as homogeneous part  $\epsilon_h$  and a perturbation  $\delta\epsilon$  representing the inhomogeneous part.<sup>146,149</sup> From this starting point, the respective  $T$  matrices are obtained by solving Maxwell's equations using Green's function. Calculating ensemble averages of  $T$  matrices, a formula for the effective permittivity can be derived (for details see e.g., Refs. <sup>146,149</sup>). The most famous representative of this group is the Maxwell–Garnett mixing rule, which was presented in 1904 by J. C. Maxwell Garnett.<sup>150</sup>

The second class comprises approaches being akin to the coherent potential approximation (CPA).<sup>151</sup> At first glance, this concept appears to be quite similar to the ATA, since the permittivity is also treated as a homogeneous part with a perturbation, while Maxwell's equations are solved.<sup>146</sup> However, there is a fundamental difference between both approximations. In the CPA, the homogeneous part is assumed to be the effective medium itself (i.e.,  $\epsilon_h = \epsilon_{\text{eff}}$ ), instead of the background medium. Thus, in the case of the CPA a self-consistent mean-field approach is obtained, while methods related to the ATA are non-self-consistent.<sup>144,146</sup> A formula for the effective permittivity can be deduced by demanding the self-consistency (further details can be found e.g., in Refs. <sup>146,152</sup>). The Bruggeman mixing rule, published in 1935 by D. A. G. Bruggeman,<sup>153</sup> established this class of methods and is still one of the most frequently used mixing rules.<sup>144,154</sup>

Before the Maxwell–Garnett and Bruggeman mixing rule are covered in more depth in Secs. 2.4.1 and 2.4.2, respectively, some fundamental notes should be taken. First, in most literature, methods belonging to the class of ATA as well as CPA are denoted as *effective medium theory*, since they allow for calculating the effective permittivity of a heterogeneous medium. However, only techniques relying on the CPA are effective medium theories in the actual sense because the term *effective medium theory* refers to the assumption that every inclusion is surrounded by the same effective medium.<sup>144,146</sup> Nevertheless, due to their similar outcome, both concepts can be considered in the same context, as it is done here.

Second, because of distinct presumptions, various methods possess different limitations. For example, ATA-like concepts are in principle only valid for small volume fractions, since the overall perturbation of the homogeneous background induced by inclusions must be small.<sup>146</sup> Contrarily, techniques relying on the CPA can conceptually handle higher filling fractions as further discussed in Sec. 2.4.2.<sup>146</sup> However, depending on the microscopic details of the composite medium, also ATA-like methods can provide reasonable results at higher filling fractions.<sup>155–157</sup> In general, it should be borne in mind that all homogenization techniques are approximations and that it is not possible to represent all properties of heterogeneous media by effective quantities in any situation.<sup>35,144,158</sup> Therefore, these methods should be used cautiously and their validity might be tested case by case.

Third, the concept of homogenizing material properties is not exclusive for permittivity but a rather general concept, which can be applied for heat and thermal conductivity, elasticity, permeability and many more.<sup>143,144,159</sup> Indeed, methods initially developed to compute the effective permittivity are often transferred to calculate the effective conductivity and vice versa.<sup>152</sup>

### 2.4.1 Maxwell–Garnett mixing rule

There are several ways to derive the Maxwell–Garnett mixing rule.<sup>35</sup> Since it belongs to the class of ATA-like methods as mentioned above, it can be indeed obtained from the ATA in the limit of small filling fractions.<sup>149</sup> Here, a different approach is presented, which provides additional insights in the underlying idea and reveals potential strategies to extend the original version.<sup>35</sup>

For the derivation of the Maxwell–Garnett mixing rule, a separated grain structure is supposed. This structure type is also known as cermet structure (a portmanteau of the words *ceramic* and *metal*) due to the similar geometry of this kind of composite medium.<sup>155</sup> Fig. 2.9a shows a sketch of a separated grain structure, consisting of a background medium with permittivity  $\epsilon_1$ , which encloses grains with the permittivity  $\epsilon_2$ . Thereby, grains are not in contact with each other, and their typical diameter  $d$  is assumed to be much smaller than the wavelength of light, that means  $d \ll \lambda$ . Since this structure type enables an unambiguous assignment of the host medium and the inclusions (in contrast to the Bruggeman case regarded in the next section), it is convenient to rename the permittivities here according to  $\epsilon_h = \epsilon_1$  and  $\epsilon_i = \epsilon_2$ .

In general, the effective permittivity  $\epsilon_{\text{eff}}$  can be obtained as the proportional constant between the average displacement field  $\bar{\mathbf{D}}$  (note that the bar indicates average quantities) and the average electric field  $\bar{\mathbf{E}}$  within the composite medium:<sup>160</sup>

$$\bar{\mathbf{D}} = \epsilon_{\text{eff}} \bar{\mathbf{E}}. \quad (2.20)$$

In addition, the displacement field is also related to the average polarization  $\bar{\mathbf{P}}$  via

$$\bar{\mathbf{D}} = \epsilon_h \bar{\mathbf{E}} + \bar{\mathbf{P}}. \quad (2.21)$$

Regarding the dipole moment  $\bar{\mathbf{p}}$  of each scatterer, the polarization is given by

$$\bar{\mathbf{P}} = n \bar{\mathbf{p}}, \quad (2.22)$$

with the density of dipole moments  $n$ .<sup>160</sup> In this, it is assumed that all dipole moments are identical. For various dipole moments, Eq. (2.22) can be easily extended by summarizing the product of dipole moment and respective volume density for all different types of dipoles. The dipole moment can be calculated using the polarizability  $\alpha$  and the local electric field  $\bar{\mathbf{E}}_{\text{local}}$ :

$$\bar{\mathbf{p}} = \alpha \bar{\mathbf{E}}_{\text{local}}. \quad (2.23)$$

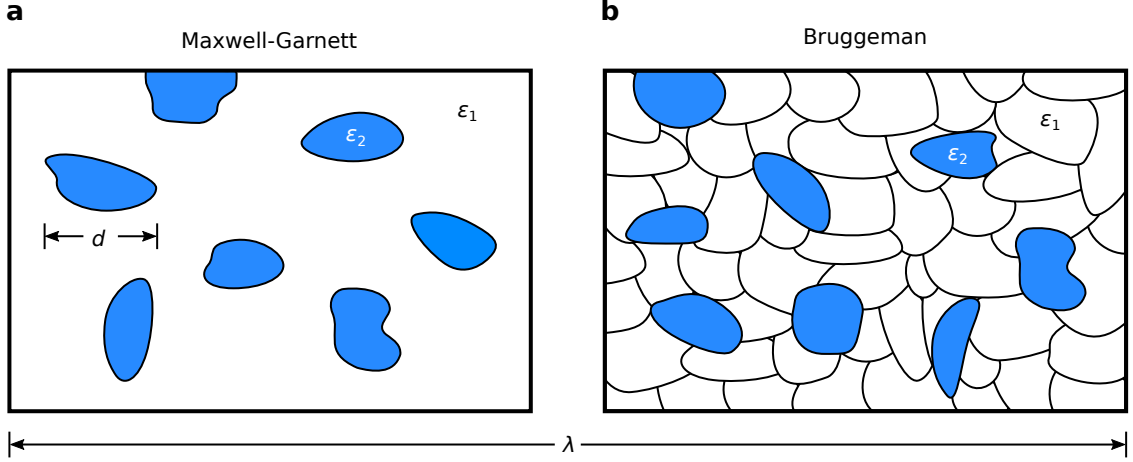


Figure 2.9: **a**, Illustration of a composite medium as assumed by the Maxwell–Garnett mixing rule. The background medium (white, permittivity  $\epsilon_1$ ) contains inclusions (blue, permittivity  $\epsilon_2$ ), which are small against the wavelength, i.e.,  $d \ll \lambda$ . **b**, Sketch of a composite medium consisting of two constituents as presumed by the Bruggeman mixing rule. The entire medium is made up of grains of two different constituents (white and blue) with permittivity  $\epsilon_1$  and  $\epsilon_2$ , respectively. Every grain is small against the wavelength. The figure is redrawn from Ref. <sup>161</sup> with slight adaptation of the color scheme. ©American Meteorological Society. Used with permission. The figure is excluded from the CC BY license of this thesis.

The local field is composed of the average field in the medium and an internal field induced by distant, surrounding scattering particles. Note that the collective contribution of all nearby scattering particles is zero in almost all random media.<sup>162</sup> To determine the internal field, an imaginary sphere is assumed around the scattering particle, which has a charge density on its surface induced by the external, neighboring particles. The internal field is then received as the resulting field at the center of this sphere.<sup>162</sup> The corresponding local field is given by<sup>160,162</sup>

$$\bar{\mathbf{E}}_{\text{local}} = \bar{\mathbf{E}} + \frac{\bar{\mathbf{P}}}{3\epsilon_h}. \quad (2.24)$$

Inserting Eq. (2.24) in Eq. (2.23) and subsequently in Eq. (2.22) yields:

$$\bar{\mathbf{P}} = n\alpha\left(\bar{\mathbf{E}} + \frac{\bar{\mathbf{P}}}{3\epsilon_h}\right). \quad (2.25)$$

Using Eq. (2.21) and Eq. (2.20), the polarization can be also given by

$$\bar{\mathbf{P}} = \bar{\mathbf{D}} - \epsilon_h \bar{\mathbf{E}} = (\epsilon_{\text{eff}} - \epsilon_h) \bar{\mathbf{E}}. \quad (2.26)$$

Inserting Eq. (2.26) in Eq. (2.25) finally delivers an expression for the effective permittivity:<sup>160</sup>

$$\frac{\epsilon_{\text{eff}} - \epsilon_h}{\epsilon_{\text{eff}} + 2\epsilon_h} = \frac{n\alpha}{3\epsilon_h}, \quad (2.27)$$

which is in this implicit form renowned as Clausius–Mossotti relation.<sup>35,160,162,163</sup>

Starting with the Clausius–Mossotti relation, the challenge of calculating the effective permittivity reduces to the problem of determining an appropriate polarizability  $\alpha$  for the scattering particles. In the simplest case, the inclusions are assumed to be spheres with a radius  $a$  much smaller than the wavelength. Thus, the electrostatic value for the polarizability of a sphere embedded in a background medium can be used, which is given by<sup>160</sup>

$$\alpha = 4\pi\epsilon_h a^3 \frac{\epsilon_i - \epsilon_h}{\epsilon_i + 2\epsilon_h}. \quad (2.28)$$

Inserting this polarizability in the Clausius–Mossotti relation yields:

$$\frac{\epsilon_{\text{eff}} - \epsilon_h}{\epsilon_{\text{eff}} + 2\epsilon_h} = f \frac{\epsilon_i - \epsilon_h}{\epsilon_i + 2\epsilon_h}, \quad (2.29)$$

where  $f = (4/3)\pi a^3 n$  is the filling fraction of inclusions. Writing Eq. (2.29) in its explicit form gives the Maxwell–Garnett (MG) mixing rule:<sup>35,150,163</sup>

$$\epsilon_{\text{eff}} = \epsilon_{\text{MG}} = \epsilon_h \frac{\epsilon_i(1 + 2f) + 2\epsilon_h(1 - f)}{\epsilon_i(1 - f) + \epsilon_h(2 + f)}. \quad (2.30)$$

As it can be discerned from Eq. (2.30), the Maxwell–Garnett mixing rule only depends on the permittivity of host medium and inclusions, as well as the filling fraction of the inclusions. Thus, only little information about the composite medium is required to calculate the effective permittivity according to the Maxwell–Garnett mixing rule. On the downside, the Maxwell–Garnett mixing rule is only valid in the long-wavelength limit where the inclusions can be represented by (electrostatic) dipoles, i.e., effects which arise from the finite size of the inclusions are not captured.

However, considering the presented framework, several strategies to include size effects have been proposed.<sup>35,164–166</sup> The essence of these approaches is to replace the electrostatic polarizability by more realistic polarizabilities incorporating size effects, for instance taking magnetic or higher-order multipole terms into account.<sup>35,163</sup>

### 2.4.2 Bruggeman mixing rule

As in the case of the Maxwell–Garnett mixing rule, the Bruggeman mixing rule can be deduced in different ways. While there are various mathematically rigorous derivations,<sup>153,167–169</sup> in the following a rather argumentative approach is used, which highlights the differences in the fundamental concept of the Maxwell–Garnett and Bruggeman mixing rule. The given argumentation is oriented at the one provided in Ref.<sup>163</sup>

First, the assumption that all inclusions are made up of the same material is omitted. Instead, inclusions with different permittivities  $\epsilon_j$ ,  $j = 1, 2, \dots, N$  are supposed.



Applying the procedure exhibited in Sec. 2.4.1 for every sort of inclusion individually, Eq. (2.29) can be extended in the following way:

$$\frac{\epsilon_{\text{eff}} - \epsilon_{\text{h}}}{\epsilon_{\text{eff}} + 2\epsilon_{\text{h}}} = \sum_{j=1}^N f_j \frac{\epsilon_j - \epsilon_{\text{h}}}{\epsilon_j + 2\epsilon_{\text{h}}}, \quad (2.31)$$

with  $f_{\text{h}} = 1 - \sum_{j=1}^N f_j$ . From Eq. (2.31) it can be seen that the role of different inclusions can be interchanged ( $\epsilon_j \longleftrightarrow \epsilon_k$  and  $f_j \longleftrightarrow f_k$ , with  $j, k \in 1, \dots, N$ ) without changing the equation. Thus, the inclusions enter the equation symmetrically, as expected, since there is nothing that distinguishes one inclusion from the others. The host medium, in contrast, does not enter the equation symmetrically, as it can be seen if the permutation  $\epsilon_{\text{h}} \longleftrightarrow \epsilon_j$  and  $f_{\text{h}} \longleftrightarrow f_j$  with  $j \in 1, \dots, N$  is applied.<sup>161,163</sup>

For the case of similar materials, e.g., pure dielectric materials, the only reason to discriminate between the host medium and the inclusions is the volume fraction, which is so far assumed to be much larger for the host than for the inclusions. However, for composite media where the filling fraction of the inclusions is comparable to that of the host, the assignment as ‘host’ and ‘inclusions’ becomes arbitrary, and the applicability of the Maxwell–Garnett mixing rule is highly questionable.<sup>163</sup>

The Bruggeman mixing rule circumvents this problem since all constituents enter the mixing rule symmetrically. This enables, at least theoretically, the computation of the effective permittivity at all volume fractions.<sup>163</sup> For the Bruggeman mixing rule a slightly different geometry of the composite medium is presumed, as illustrated in Fig. 2.9b. In contrast to the separated grain structure (see Fig. 2.9a), the whole composite medium is composed of grains belonging to different constituents, hence a host medium is absent.<sup>161,168</sup>

However, regarding the medium as an effective medium, every grain is considered to be embedded in a homogeneous (host) medium possessing the effective permittivity (see Sec. 2.4). Hence, the permittivity of the effective medium must occur in the Bruggeman mixing rule as the permittivity of the host (i.e.,  $\epsilon_{\text{h}} = \epsilon_{\text{eff}}$ ). For the corresponding filling fraction  $f_{\text{h}} = 0$  is obtained, since the effective (host) medium is generated by all other grains, which are already considered with their respective filling fractions. Applying these arguments to Eq. (2.31) yields the Bruggeman (BG) mixing rule:

$$\sum_{j=1}^N f_j \frac{\epsilon_j - \epsilon_{\text{BG}}}{\epsilon_j + 2\epsilon_{\text{BG}}} = 0, \quad (2.32)$$

with  $\sum_{j=1}^N f_j = 1$ .<sup>163</sup> For the case  $N = 2$ , the Bruggeman mixing rule can be given in an explicit form as<sup>163</sup>

$$\epsilon_{\text{BG}} = \frac{b + \sqrt{8\epsilon_1\epsilon_2 + b^2}}{4}, \quad (2.33)$$

where

$$b = (2f_1 - f_2)\epsilon_1 + (2f_2 - f_1)\epsilon_2. \quad (2.34)$$

While claiming a symmetric mixing formula is reasonable for many composite media, this is not the case in general, as shown in the following example according to Ref. <sup>163</sup> A sample structure shall be considered which contains spheres embedded in a homogeneous background such that the filling fraction of the spheres is 50%, while none of the spheres are in touch. When the spheres are composed of a conducting material while the background is dielectric, the entire composite medium will be an insulator. Conversely, a conducting composite medium is obtained when materials are swapped in the same geometry. While both media are obviously quite different, a symmetric mixing rule provides in both cases the same effective permittivity.<sup>163</sup>

Therefore, there is no general rule that a symmetric or non-symmetric mixing rule delivers better results. It rather depends on the microscopic details of the composite medium as well as the involved materials which kind of mixing rule is most appropriate to calculate the effective permittivity.

## 3 Methods

The numerical and experimental methods used in the course of this thesis are presented in this chapter. In that, the basic concepts underlying the numerical methods are exhibited and common simulation parameters are summarized. In addition, the different experimental setups used for sample fabrication as well as measuring and analyzing are displayed and briefly reviewed.

### 3.1 Numerical methods

The FDTD simulation method, the Monte Carlo simulation method, and the force-biased algorithm are outlined in the following. FDTD simulations are used to calculate the effective permittivity of random media as well as to simulate coherent aspects of light transport. Incoherent, diffusive light transport is conversely calculated with the aid of Monte Carlo simulations. The force-biased algorithm enables the generation of various random sphere packings, which are needed for a systematic investigation of size effects in the effective refractive index computation.

#### 3.1.1 Finite-difference time-domain simulations

The FDTD method is a numerical time-domain technique which enables to compute the propagation of electromagnetic waves through regions filled with an arbitrary arrangement of different materials. It was first presented in 1966 by K. S. Yee,<sup>170</sup> thus it is sometimes also referred to as Yee algorithm or Yee method.

The essence of the method is the discretization of time and space which allows to rewrite Maxwell's equations as finite difference equations.<sup>170</sup> By taking finite differences of the electric field components at one point in time, the magnetic field components at the next point in time can be calculated at each mesh point and vice versa. This leads to a leapfrog scheme, i.e., alternately determining the electric and magnetic field components, which enables to compute the fields at all later times from the initial values provided in the first time step.<sup>111,170,171</sup>

One advantage of this method is its applicability to arbitrary scattering geometries without modifying the algorithm.<sup>171</sup> Frequency-domain methods,<sup>172–174</sup> in contrast, require for every scatterer the derivation of a set of equations, which holds true just for the specific geometry.<sup>171</sup> Another advantage arises from the fact that the FDTD method is a time-domain technique. Using a sufficiently short excitation pulse, the response of the considered medium for a large range of frequencies can be calculated in a single simulation.<sup>175</sup>

The FDTD method, nevertheless, also possesses some drawbacks. To obtain a suitable accuracy the step size of the mesh must be much smaller than the shortest wavelength or smallest feature size, respectively. Hence, for large sample volumes (compared to the wavelength), the calculation can require high amount of memory

and computation time.<sup>171</sup> Moreover, the numerical dispersion of the algorithm leads to errors and thus lowers the accuracy of the results.<sup>111</sup>

Below, the deduction of the Yee algorithm is sketched, which can be found in more detail in the literature.<sup>170,171,175</sup> Since the FDTD method is intended to solve Maxwell's equations, the component-wise formulation of these equations is the starting point of the derivation:

$$-\frac{\partial B_x}{\partial t} = \frac{\partial E_z}{\partial y} - \frac{\partial E_y}{\partial z}, \quad (3.1a)$$

$$\frac{\partial D_x}{\partial t} = \frac{\partial H_z}{\partial y} - \frac{\partial H_y}{\partial z} - J_x, \quad (3.1b)$$

where the other components are obtained by cyclic permutation  $(x \ y \ z)$  of Eq. (3.1a) and Eq. (3.1b), respectively.

To obtain finite difference equations instead of derivations, the continuous simulation volume is replaced by a discrete mesh with spatial steps  $\Delta x$ ,  $\Delta y$ , and  $\Delta z$ , while the time is incremented in time steps of  $\Delta t$ . For simplicity mesh points are denoted as<sup>170</sup>

$$(p\Delta x, q\Delta y, r\Delta z) = (p, q, r), \quad (3.2)$$

while functions of space and time are given by

$$F(p\Delta x, q\Delta y, r\Delta z, s\Delta t) = F^s(p, q, r). \quad (3.3)$$

Using the introduced notation, the derivations are approximated by finite difference expressions in the following way:<sup>171</sup>

$$\frac{\partial F^s(p, q, r)}{\partial x} = \frac{F^s(p + \frac{1}{2}, q, r) - F^s(p - \frac{1}{2}, q, r)}{\Delta x} + \mathcal{O}((\Delta x)^2), \quad (3.4a)$$

$$\frac{\partial F^s(p, q, r)}{\partial t} = \frac{F^{s+\frac{1}{2}}(p, q, r) - F^{s-\frac{1}{2}}(p, q, r)}{\Delta t} + \mathcal{O}((\Delta t)^2), \quad (3.4b)$$

while similar equations are applied for the derivative to  $y$  and  $z$ . To receive expressions that are second-order accurate in  $\Delta x$  and  $\Delta t$  (as the ones above), the electric and magnetic field components have to be calculated alternately in half time steps as well as at different positions in the unit cell. Computing the fields at the same position would result in expressions which are just first-order accurate in  $\Delta x$  and  $\Delta t$ .<sup>171</sup> Fig. 3.1 shows a unit cell of the so-called Yee lattice exhibiting the different positions at which the electric and magnetic field components are computed.

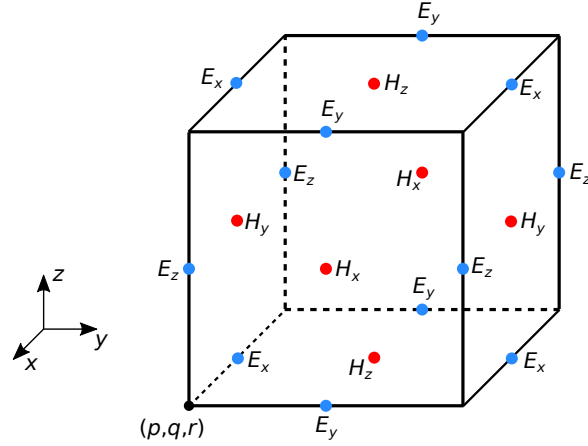


Figure 3.1: Position of different field components in the unit cell of the Yee lattice. The blue dots indicate the electric field component in the middle of the edges, while the red dots show the magnetic field components in the middle of the surfaces. Adapted from Ref. <sup>95</sup>

Using the finite difference expressions (3.4a) and (3.4b) as well as the material equations  $B = \mu_0\mu H$  and  $D = \epsilon_0\epsilon E$  for under the assumption of time-independent, linear and isotropic material properties, Eq. (3.1a) yields:<sup>170,171</sup>

$$\begin{aligned}
 H_x^{s+\frac{1}{2}}(p, q + \frac{1}{2}, r + \frac{1}{2}) &= H_x^{s-\frac{1}{2}}(p, q + \frac{1}{2}, r + \frac{1}{2}) \\
 &+ \frac{\Delta t}{\mu_0\mu(p, q + \frac{1}{2}, r + \frac{1}{2})\Delta z} \left( E_y^s(p, q + \frac{1}{2}, r + 1) - E_y^s(p, q + \frac{1}{2}, r) \right) \\
 &- \frac{\Delta t}{\mu_0\mu(p, q + \frac{1}{2}, r + \frac{1}{2})\Delta y} \left( E_z^s(p, q + 1, r + \frac{1}{2}) - E_z^s(p, q, r + \frac{1}{2}) \right), \quad (3.5)
 \end{aligned}$$

while Eq. (3.1b) delivers:

$$\begin{aligned}
 E_x^s(p + \frac{1}{2}, q, r) &= E_x^{s-1}(p + \frac{1}{2}, q, r) + \Delta t J_x^{s-\frac{1}{2}}(p + \frac{1}{2}, q, r) \\
 &+ \frac{\Delta t}{\epsilon_0\epsilon(p + \frac{1}{2}, q, r)\Delta y} \left( H_z^{s-\frac{1}{2}}(p + \frac{1}{2}, q + \frac{1}{2}, r) - H_z^{s-\frac{1}{2}}(p + \frac{1}{2}, q - \frac{1}{2}, r) \right) \\
 &- \frac{\Delta t}{\epsilon_0\epsilon(p + \frac{1}{2}, q, r)\Delta z} \left( H_y^{s-\frac{1}{2}}(p + \frac{1}{2}, q, r + \frac{1}{2}) - H_y^{s-\frac{1}{2}}(p + \frac{1}{2}, q, r - \frac{1}{2}) \right). \quad (3.6)
 \end{aligned}$$

Equivalent expressions can be obtained for  $H_y$ ,  $H_z$ ,  $E_y$ , and  $E_z$  (see e.g., Refs. <sup>171,175</sup>).

Considering Eq. (3.5) and Eq. (3.6), the Yee algorithm can be understood. In (3.5) the  $x$ -component of the magnetic field at the time step  $s + \frac{1}{2}$  can be calculated from the  $y$ - and  $z$ -component of the electric field at the previous (half) time step  $s$ . Conversely, the respective component of the electric field solely depends on the

magnetic field components of the previous (half) time step (cf. Eq. (3.6)). Thus, every component can be computed successively.

In that, the geometry of the medium enters the algorithm through the permeability and permittivity in Eq. (3.5) and Eq. (3.6), respectively. Since both values can be individually defined for each mesh point, the formalism allows to treat scatterers with arbitrary shape and composition. To resolve fine features, however, the size of the spatial steps must be sufficiently small. Alternatively, advanced techniques like conformal meshing can be used which allow to take permittivity changes within a unit cell into account, for instance at a curved surface.<sup>176</sup>

Another issue that must be treated are the boundaries of the simulation volume. In realistic experimental setups, samples are usually placed in free space or at least in a homogeneous environment, i.e., light that is emitted or reflected from the sample will mostly not return. In FDTD simulations, however, the simulation volume usually cannot be chosen much larger than the sample volume, otherwise impractical computation times will result. To simulate light that is emitted in free space, it must be ensured that light is not reflected at the boundaries of the simulation volume for this reason.

While there are several techniques to define such boundaries,<sup>177–179</sup> the most efficient way is the use of so-called perfectly matched layer (PML) boundaries.<sup>180,181</sup> The idea behind the PML is to apply an absorbing medium at the boundary which is impedance matched to the adjacent media, hence the reflection at the interface is suppressed.<sup>180</sup>

Beside PML boundaries, another type of boundaries is frequently used, namely periodic boundaries. Light that leaves these boundaries at one side of the simulation volume is re-emitted at the opposite side of the simulation volume. These boundaries are either used to simulate periodic structures, since only one unit cell must be considered, or they are applied to realize infinitely extended, uniform objects.

As part of this thesis, the commercial software Lumerical FDTD solutions (ANSYS Inc., USA) is used to conduct various FDTD simulations. The software provides by default numerous sources, monitors, boundary conditions, and analysis tools.

For the evaluation of the effective refractive index (see Ch. 4), a total-field scattered-field source is used in conjunction with the *far-field from closed box* analysis group and PML boundaries in all directions. The total-field scattered-field source occupies a 3D box, in contrast to conventional sources, which are defined by a 2D plane. Inside the box, the total field of the impinging plane wave is computed, which comprises the incident and the scattered field. However, at the edge of the box the incident field is subtracted, thus outside of the box only the scattered field is obtained.

The *far-field from closed box* analysis group contains a 3D box of field monitors. It enables the calculation of the far field projection for every direction by computing this quantity for every monitor separately and summing up the results. By default the far field projection is calculated on a hemisphere with a radius of 1 m where the

sample is in the center and the electric field of the incident plane wave possesses an amplitude of 1 V/m. With this setup it is therefore possible to evaluate the far field projection of solely the scattered light in all directions, while the forward scattering direction is of particular interest.

To identify the role of coherent effects in light propagation through strongly scattering white media, as it is done in Ch. 5, a different simulation setup is used. Here, the source injects a plane wave light pulse impinging on the sample in  $z$ -direction. In this direction PML boundaries are used while periodic boundary conditions are applied in the  $x$ - and  $y$ -direction. The medium is thus infinitely extended in the lateral direction to avoid unintended effects from the finite size of the simulation volume. This setup is a reasonable way to approximate experimental conditions, where the typical spot size of the laser is at least two orders of magnitude smaller than the lateral extent of the scales (see Sec. 3.2.2 or Ref. <sup>21</sup>), i.e., the incident light generally does not reach the lateral edge of the scales.

To obtain the distribution of photon lifetimes within different strongly scattering media, 3900 dot-shaped frequency monitors are placed in a roughly  $7 \times 7 \times 7 \mu\text{m}^3$  cube of the respective medium. In addition, the time-dependent power distribution inside the DBS model structure is evaluated. For this purpose, a time-domain monitor cross sectioning the structure in the  $x$ - $z$ -plane is used to record the Poynting vector every 1.14 fs at every grid point in the monitor plane. In contrast to the other simulations, a lateral footprint of about  $20 \times 20 \mu\text{m}^2$  is used here, while the height of the structure remains the same.

### 3.1.2 Monte Carlo simulations

Monte Carlo simulations are a popular numerical technique for modeling complex systems, e.g., in particle physics, bio-optics, and financial engineering.<sup>182–187</sup> As a statistical approach, Monte Carlo simulations do not require an analytic model of the underlying system.<sup>186</sup> Instead, a large amount of independent random experiments are performed to obtain the quantity of interest as the expected value of one or more random variables.<sup>184</sup> This technique is therefore suited for cases where either no analytical model exists or solving an available model is non-trivial or too costly.<sup>186</sup>

The latter is the fact for light propagation in extended disordered media,<sup>188</sup> which could be in principle exactly computed conducting FDTD simulations or approximately described by means of the radiative transport equation or diffusion theory. However, because of excellent agreement between Monte Carlo simulation results and the predictions of analytic theories in many cases, Monte Carlo simulations are used to evaluate light transport in disordered media, especially biological tissues, for about 40 years.<sup>185,186,189–191</sup>

As part of this thesis a Monte Carlo simulation tool is implemented, which can be adjusted to approach the setup of the corresponding FDTD simulations. Hereinafter, the general Monte Carlo method for calculating photon transport is explained first,

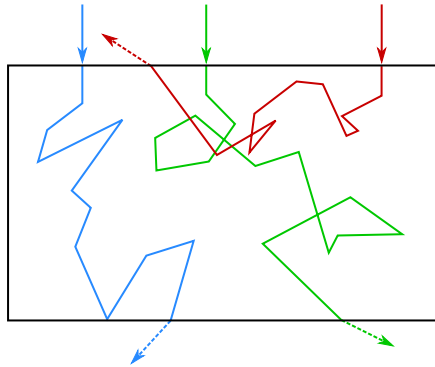


Figure 3.2: Illustration of a random walk of three separate photons in a purely scattering medium.

while the specific details of the Monte Carlo tool used are presented at the end of this section.

The basic idea of the algorithm is to treat photons as particles and perform a random walk for each photon to obtain its trajectory in the medium. In this process, the photon undergoes steps with various length, with a scattering and absorption event occurring at the end of each step. The scattering event deflects the photon from its previous direction, while absorption diminishes the weight which is assigned to the photon. An example of such a random walk is shown in Fig. 3.2 for three distinct photons.

During the random walk, the current position of the photon is stored in the triple  $(x, y, z)$ . Note that the position can take continuous values, unlike the discrete grid points in case of the FDTD method. In addition, the direction of travel is given by the triple  $(\mu_x, \mu_y, \mu_z)$ , where  $\mu_x$  is the cosine of the angle between this direction and the  $x$ -axis and so forth.<sup>185,190</sup> A movement of the photon by a distance  $\Delta s$  thus results in the updated position:

$$x := x + \mu_x \Delta s, \quad (3.7a)$$

$$y := y + \mu_y \Delta s, \quad (3.7b)$$

$$z := z + \mu_z \Delta s. \quad (3.7c)$$

The step size  $\Delta s$  is determined by the probability density function:

$$p(\Delta s) = \gamma_{\text{ext}} \exp(-\gamma_{\text{ext}} \Delta s), \quad (3.8)$$

with the extinction coefficient  $\gamma_{\text{ext}}$ , as given in Sec. 2.3.1.<sup>185</sup> Considering the definition of the extinction coefficient, it can be directly shown that the probability density function must follow Beer's law (see e.g., Ref.<sup>185</sup>). Mapping a uniformly distributed density function over the interval  $(0, 1)$  to the non-uniformly distributed density function  $p(\Delta s)$ , the step size  $\Delta s$  can be obtained from the random variable



$\xi \in (0, 1)$  via<sup>190</sup>

$$\Delta s = \frac{-\ln(\xi)}{\gamma_{\text{ext}}}, \quad (3.9)$$

Further details regarding the mapping can be found in the literature.<sup>184,185</sup>

After a move has been made, the corresponding absorption must be computed. To account for absorption effects, a weight of  $w = 1$  is initially assigned to every photon which is stepwise decreased according to

$$w := w - \frac{\gamma_a}{\gamma_{\text{ext}}}w = w - \left(1 - \frac{\gamma_s}{\gamma_{\text{ext}}}\right)w = W_0w, \quad (3.10)$$

with the albedo  $W_0$  as declared in Sec. 2.3.1.<sup>185,190</sup> Conversely, the portion  $(1 - W_0)w$  is absorbed by the medium at the current site, which is recorded in an absorption matrix to evaluate quantities such as the fluence rate in the medium and so on.<sup>190</sup>

Beside absorption, the change of the photon direction due to scattering must be considered after a step has been taken. This is done by statistically sampling a polar angle  $\phi$  and an azimuthal angle  $\theta$ . Since scattering is usually isotropic around the incident direction (cf. Sec. 2.3.1), the polar angle can be obtained by

$$\phi = 2\pi\xi, \quad (3.11)$$

where  $\xi$  is again a random number which is uniformly distributed over the interval from zero to one. For isotropic scattering the cosine of the azimuthal angle can be evaluated using the expression:

$$\cos(\theta) = 2\xi - 1, \quad (3.12)$$

while anisotropic scattering is determined by mapping the uniformly distributed density function to the normalized Henyey–Greenstein phase function:<sup>185,190</sup>

$$\cos(\theta) = \frac{1}{2g} \left( 1 + g^2 - \left( \frac{1 - g^2}{1 - g + 2g\xi} \right)^2 \right). \quad (3.13)$$

Note that a separate random number  $\xi \in [0, 1]$  is computed for each angle. Once the angles are received, the current photon direction is updated:<sup>190</sup>

$$\mu_x := \frac{\sin(\theta)}{\sqrt{1 - \mu_z^2}} (\mu_x \mu_z \cos(\phi) - \mu_y \sin(\phi)) + \mu_x \cos(\theta), \quad (3.14a)$$

$$\mu_y := \frac{\sin(\theta)}{\sqrt{1 - \mu_z^2}} (\mu_y \mu_z \cos(\phi) + \mu_x \sin(\phi)) + \mu_y \cos(\theta), \quad (3.14b)$$

$$\mu_z := -\sin(\theta) \cos(\phi) \sqrt{1 - \mu_z^2} + \mu_z \cos(\theta). \quad (3.14c)$$

If the previous direction is very close to the  $z$ -direction (typically at  $\mu_z > 0.99999$ ), the new photon direction is calculated by<sup>185</sup>

$$\mu_x = \sin(\theta) \cos(\phi), \quad (3.15a)$$

$$\mu_y = \sin(\theta) \sin(\phi), \quad (3.15b)$$

$$\mu_z = \text{sgn}(\mu_z) \cos(\theta). \quad (3.15c)$$

While a photon is scattered and absorbed during a random walk, its weight is successively decreased but never drops to zero. Hence, a termination condition must be defined to avoid the (costly) propagation of photons which bear a negligible amount of information due to their vanishing small weight. To account for energy conservation, however, photons with a weight below a certain threshold cannot just be discarded.<sup>190</sup>

Instead, a technique renowned as Russian roulette is applied.<sup>185</sup> Once the weight falls below a designated threshold, a uniformly distributed random number  $\xi \in [0, 1]$  is computed. If this number is greater than a predefined probability of one chance in  $m$  (i.e.,  $\xi > 1/m$ ), the remaining weight of the photon is set to zero and the photon is deleted. Otherwise, the photon is allowed to continue propagation with a new weight of  $mw$ . In this, energy conservation is fulfilled while the correct absorption coefficient  $\gamma_a$  is retained.<sup>185</sup>

The framework presented above can be used for Monte Carlo simulations of photon migration in infinitely extended random media. However, media that are finite at least in one spatial direction (here the  $z$ -direction) are frequently of interest. Therefore, reflection at the boundaries between different media must be considered.

When photons are launched in the ambient medium with refractive index  $n_0$ , only a fraction of light will enter the random medium because of specular reflection at the interface. In the case where the direction of incidence is equal to the normal direction (i.e.,  $z$ -direction), the specular reflectance is given by

$$R_{\text{sp}} = \frac{(n_{\text{eff}} - n_0)^2}{(n_{\text{eff}} + n_0)^2}, \quad (3.16)$$

with the effective refractive index of the the random medium  $n_{\text{eff}}$ .<sup>185</sup> To account for the specular reflection, the initial weight of the photon must be accordingly reduced by the specular reflectance:<sup>185</sup>

$$w = 1 - R_{\text{sp}}. \quad (3.17)$$

Inside the medium, the photon can take a step which is long enough to cross a boundary, so that the photon is either internally reflected or transmitted through the boundary. The probability of an internal reflection can be calculated using the

Fresnel reflectance:

$$R(\theta_i) = \frac{1}{2} \left( \frac{\sin^2(\theta_i - \theta_r)}{\sin^2(\theta_i + \theta_r)} + \frac{\tan^2(\theta_i - \theta_r)}{\tan^2(\theta_i + \theta_r)} \right), \quad (3.18)$$

with the incident angle  $\theta_i = \cos^{-1}(\mu_z)$  and the angle of refraction  $\theta_r$ .<sup>185,190</sup> Since the Monte Carlo method treats the photons as particles, the polarization of light is not traced. Thus, in Eq. (3.18) the Fresnel reflectance is given as the average over the reflectance for parallel and perpendicular polarization direction. The angle of refraction is determined by Snell's law:

$$n_{\text{eff}} \sin(\theta_i) = n_0 \sin(\theta_r). \quad (3.19)$$

To decide if the photon is reflected or transmitted at the boundary, a uniformly distributed random number  $\xi \in [0, 1]$  is computed. In the case of  $\xi < R(\theta_i)$  the photon is internally reflected, else it leaves the sample and contributes either to the total reflectance or transmittance of the medium.<sup>185,190</sup> Since the position of the photon after the step lies outside of the medium, it must be corrected in the case of internal reflection. For a slab which is infinitely extended in the  $x$ - and  $y$ -direction and possesses boundaries at  $z = 0$  and  $z = t$ , the correction for the  $z$ -component is obtained by<sup>190</sup>

$$z := \begin{cases} -z, & \text{if } z < 0, \\ 2t - z, & \text{if } z > t. \end{cases} \quad (3.20)$$

In addition, the photon direction also has to be changed according to  $\mu_z := -\mu_z$ . For media that are also finite in  $x$ - or  $y$ -direction, analogous adjustments are obtained.

To simulate purely diffusive light transport in strongly scattering media (see Ch. 5), a Monte Carlo simulation tool is coded in Matlab (The Mathwork Inc., USA) following the framework shown above. However, since all media considered in this thesis have a negligible absorption, the concept of assigning a weight to each photon is omitted.

Since the conducted Monte Carlo simulations are intended to approach the FDTD setup as close as possible, periodic boundary conditions in the  $x$ - and  $y$ -direction are implemented, i.e., a photon that leaves the slab at one side is re-emitted at the opposite side. The slab has a lateral footprint of  $12 \times 12 \mu\text{m}^2$ , while its height corresponds to the height of the structure used in FDTD simulations. The effective refractive index is calculated by means of the formula developed in Ch. 4.

As light source, a plane wave is used which emits in total  $\approx 6.8$  billion photons distributed uniformly over the entrance facet of the medium. The time profile of the plane wave is chosen to match the temporal power profile of the light pulse deployed in corresponding FDTD simulations. A monitor cross sectioning the slab records the position and time, whenever a photon passes through the monitor plane. Hence, the time-dependent distribution of photons within the slab can be tracked.

### 3.1.3 Force-biased algorithm for random sphere packing generation

To systematically investigate the influence of size effects on the effective refractive index calculation, random sphere packings with various filling fractions and sphere radii have to be generated. For this purpose, the so-called force-biased algorithm is applied.<sup>192,193</sup> This method is easy to implement and enables to generate packings of non-intersecting spheres with filling fractions close to the bound at which a packing can be still regarded random, that is around 65%.<sup>192,194</sup>

The force-biased algorithm starts with placing  $N$  seeds randomly in a 3D box with predefined size and periodic boundaries.<sup>192,193</sup> Next, for all seeds two diameters are defined, an inner diameter  $d_{\text{in}}$  and an outer diameter  $d_{\text{out}}$ . The inner diameter is initially given by the condition, that the spheres just do not intersect, i.e., at least two spheres are in touch. The outer diameter is defined by the requirement that the sum over all sphere volumes equals a predefined volume  $V_{\text{ini}}$ , which is an input variable of the algorithm.<sup>192,193</sup> Hence, considering the outer diameter, spheres are allowed to intersect, as shown in Fig. 3.3 (left panel) illustrating the initial state of the algorithm.

Starting with this setting, the following sequence is executed at each iteration.<sup>192,193</sup> First, every sphere center is moved by a ‘repulsion force’ based on the overlap of adjacent spheres corresponding to their outer diameter. The ‘repulsion force’ between two overlapping spheres  $j$  and  $k$  is computed via

$$\mathbf{F}_{jk} = \rho \mathcal{I}_{jk} p_{jk} \frac{\mathbf{r}_j - \mathbf{r}_k}{\|\mathbf{r}_j - \mathbf{r}_k\|}, \quad (3.21)$$

where  $\mathbf{r}_j$  is the position of the  $j$ th sphere,  $p_{jk}$  is the potential function,  $\mathcal{I}_{jk}$  is 1 if the spheres are overlapping and 0 if not, and  $\rho$  is a scaling factor given as an input parameter.<sup>193</sup> In the case of equal spheres, it is found that a potential function proportional to the intersection volume is appropriate:<sup>193</sup>

$$p_{jk} = \|\mathbf{r}_j - \mathbf{r}_k\|^2 - d_{\text{out}}^2. \quad (3.22)$$

The new position of the  $j$ th sphere is determined by

$$\mathbf{r}_j := \mathbf{r}_j + \frac{1}{2} \sum_{j \neq k} \mathbf{F}_{jk}. \quad (3.23)$$

After moving all spheres, the inner diameter is re-calculated in the second step to fulfill the non-intersection condition again. Finally, in the third step the outer diameter is diminished by

$$d_{\text{out}} := d_{\text{out}} - \left(\frac{1}{2}\right)^\delta d_{\text{out,ini}} / (2\tau), \quad (3.24)$$

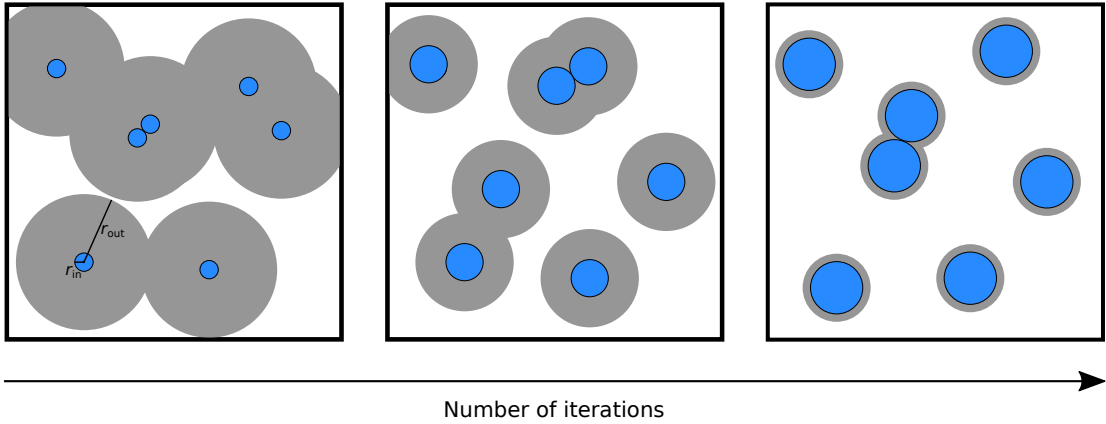


Figure 3.3: Sketch of random sphere packings obtained in the course of the force-biased algorithm. Initially an inner (blue sphere) and outer (gray sphere) radius is defined for every seed point, such that the inner spheres are just non-intersecting (left panel). Moving the centers according to the overlap of the corresponding outer spheres, decreasing the outer radius stepwise and re-calculating the inner radius to satisfy the non-intersection condition leads to a convergence of both radii and a gradual reduction of the overlaps (middle and right panel).

with  $\delta = \lfloor -\log_{10}(V_{\text{out}} - V_{\text{in}}) \rfloor$  and the contraction rate  $\tau$  set as an input parameter.<sup>192</sup> The volumes  $V_{\text{in}}$  and  $V_{\text{out}}$  represent the sum over all sphere volumes regarding the current inner and outer diameter, respectively. The diameter  $d_{\text{out,ini}}$  denotes the initial outer diameter.

In that, pushing apart of overlapping spheres tends to increase the inner radius, while the outer radius decreases successively. Both radii hence converge as the iterations progress,<sup>193</sup> as illustrated in the middle and right panel of Fig. 3.3, which respectively represent the resulting sphere packing at the end of an iteration.

The algorithm terminates if (i) both radii become equal or (ii) the inner radius reaches the desired value. However, to obtain packings with a well-defined sphere radius the algorithm is required to terminate by the second condition. This can be ensured by a reasonable choice of input parameters, especially using a sufficiently small contraction rate  $\tau$ . In addition, changing the number  $N$  of initially placed seeds, the filling fraction can be tuned.

As part of this thesis, the algorithm shown above is implemented in Matlab to generate sphere packings of non-overlapping, equal spheres with adjustable radius and filling fraction. Thereby, packings with sphere radii between 100 nm and 240 nm are realized while the filling fraction is varied between 10% and 60%. Around 500 to 3000 seeds are typically used for calculation depending on the resulting filling fraction. The contraction rate is chosen to usually lie between 800 and 20000, where higher filling fractions generally require larger contraction rates to avoid reaching the first termination condition. The initial volume  $V_{\text{ini}}$  is commonly set to be equal to the box volume or slightly lower than the box volume.

## 3.2 Experimental methods

In the sections below, the DLW setup, the time-resolved spectromicroscopy, and the  $z$ -scan technique are presented. With the help of DLW, microstructures are fabricated according to the DBS model. Beside *Cyphochilus* scales, these structures are investigated by time-resolved spectromicroscopy to unveil the influence of different transport mechanisms in strongly scattering media. In addition, the DLW device is deployed to test bio-sourced photoresists developed in the context of this thesis with respect to their suitability for fabricating 2D and 3D architectures via two-photon polymerization. The  $z$ -scan measurements are applied to evaluate the two-photon absorption cross section of different photoinitiators to find appropriate candidates for utilizing the sensitization effect for DLW.

### 3.2.1 Direct laser writing

Direct laser writing (DLW), sometimes also referred to as two-photon polymerization or laser nanoprinting, is an optical lithography technique that enables the fabrication of nearly any three-dimensional structure from submicron to centimeter scales.<sup>40,41</sup> Unlike other optical lithography methods, DLW is based on two-photon absorption which yields a quadratic optical non-linearity. The absorption thus exceeds the polymerization threshold just in the narrow focal spot of a femtosecond laser beam, which restricts the polymerized volume in all three dimensions, as shown in Fig. 3.4. This volume is also called a voxel, a portmanteau of the terms *volume* and *pixel*.

In contrast, optical lithography methods relying on linear absorption characteristics, such as UV photolithography, are lacking a sharp confinement in the axial direction

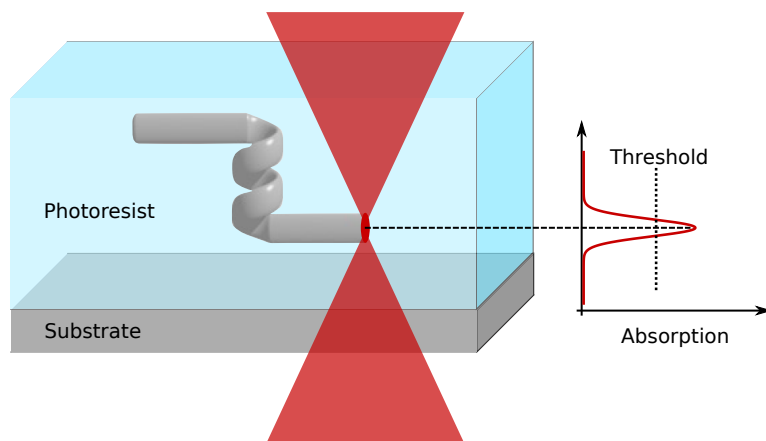


Figure 3.4: Sketch of the DLW process. The polymerized volume is restricted to the focal spot where the absorption exceeds the polymerization threshold. This confinement allows for printing structures along virtually any three-dimensional trajectory. The figure is redrawn from Ref.<sup>195</sup> with slight adaption of the color scheme. ©Wiley-VCH GmbH. Reproduced with permission. The figure is excluded from the CC BY license of this thesis.

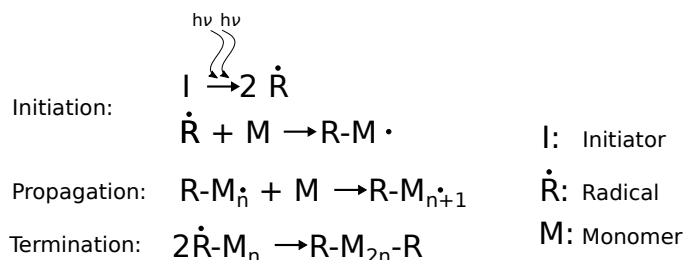


Figure 3.5: Photochemical reaction pathway of two-photon polymerization. Taken from Ref. <sup>198</sup> The figure is excluded from the CC BY license of this thesis.

which inhibits printing of true 3D architectures.<sup>196,197</sup> With DLW, however, feature sizes below 100 nm (lateral) and 300 nm (axial) as well as resolution below 500 nm (lateral and axial) can be reached, depending on the setup.<sup>40</sup> Resolution is thereby defined as the minimal distance between separated features.<sup>197</sup>

While there are numerous photoresists suitable for DLW,<sup>41</sup> most are negative-tone photoresists, usually containing a crosslinkable liquid monomer or oligomer and a photoinitiator. If the monomer is not liquid, an appropriate solvent must be added. Fig. 3.5 depicts the basic scheme of the radical chain polymerization process occurring in many photoresists. In this scheme monomers are assumed as basic unit, however, a similar reaction pathway is obtained starting with oligomers.

Upon simultaneous absorption of two photons, the photoinitiator is first split into free radicals, which then react with the monomer to form new radical sites at its end (initiation step). These radicalized compounds initialize the polymerization by successively merging with other monomers to form monomer chains, i.e., polymers, with one radical site remaining (propagation step). The chain reaction can be terminated when two radicalized chains meet, which limits the overall chain length (termination step).<sup>198</sup> Alternatively, the chain reaction is stopped by an inhibitor, usually oxygen, which is the dominant termination process in most photoresists.<sup>199,200</sup>

The inhibitor also serves as a quencher for the excited photoinitiator, which, along with the required crosslinking density to survive the development process, results in a polymerization threshold.<sup>200</sup> The existence of a polymerization threshold (which can be seen as the analogue of the Schwarzschild effect in photography) is crucial to achieve at least in principle arbitrarily small feature sizes.<sup>197</sup> In reality, experimental conditions such as pulse-to-pulse fluctuations place a lower limit on the feasible feature size.<sup>197,201</sup>

A commercial DLW system is used in this thesis, namely the Photonic Professional GT (Nanoscribe GmbH, Germany), which is sketched in Fig. 3.6. The device is equipped with a femtosecond laser operating at a wavelength of 780 nm. The laser beam first passes an acousto-optic modulator (AOM) to vary the laser power during the writing process. Behind the acousto-optic modulator, a telescope setup enlarges the beam diameter to ensure that the entrance pupil of the objective is completely illuminated. In front of the inverted microscope, two galvanometrically

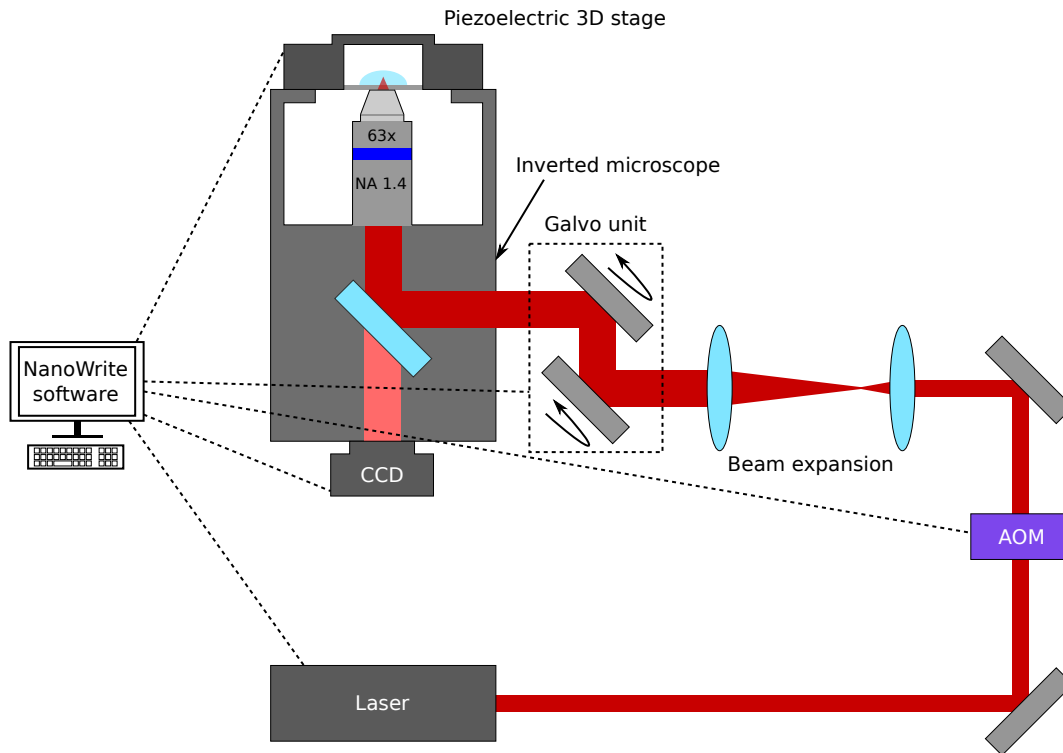


Figure 3.6: Scheme of the commercial DLW system Photonic Professional GT. Based on Ref. <sup>202</sup>

driven mirrors (short: galvo unit) are used to deflect the focus in-plane to allow for patterning. Within the inverted microscope, an objective with high numerical aperture (NA) and magnification is deployed for tightly focusing the laser beam into the photoresist. For mesoscale writing, however, objectives with low magnification and numerical aperture are used. A substrate carrying the photoresist is attached to the stage, which is endowed with a set of piezo actuators to move the resist relative to the laser focus. Hence, any three-dimensional trajectory can be traced along which the photoresist is polymerized. The setup is completed with a charge-coupled device (CCD) camera to observe the printing process. All components are controlled by the software NanoWrite (Nanoscribe GmbH).

The system allows for different operation modes. Primarily, two fundamental writing configurations can be chosen depending on the photoresist. It is possible to either apply the photoresist on the opposite side or the same side of the substrate than the objective.

The former requires the use of immersion oil between the objective and the substrate and is known as standard configuration. The laser beam must be focused through the substrate, limiting the maximum structure height to the working distance of the objective minus the thickness of the substrate, which is on the order of a few hundred microns in total. Moreover, this configuration can be only applied for transparent substrates. Conversely, the objective is not directly exposed to the photoresist and



a refractive index match between the photoresist and the lens of the objective is not necessary.

The second configuration is denoted as dip-in configuration since the objective is dipped into the resist. This enables printing of tall structures up to millimeter and centimeter heights. However, the resist has to satisfy the refractive index matching and must not contain any compound potentially hazardous for the objective.

Beside different writing configurations, there are also two distinct writing modes. On the one hand, the galvo unit can be used to move the focus relative to the resist in the lateral plane (*galvo mode*), while the axial movement is done by the respective piezo actuator or the mechanical drive of the objective. In that, high writing speeds of several mm/s can be reached. On the downside, this mode demands patterning the structure layer-by-layer, which restricts the printable structures to layouts that can be sliced in the axial direction. On the other hand, using piezo actuators in all dimensions (*piezo mode*) does not set this restriction on the layout at the cost of three orders of magnitude lower writing speeds.

Throughout the thesis, a  $63\times$  objective with  $NA = 1.4$  is used in the standard configuration. For fabricating DBS structures (see Ch. 5), a drop of the commercial photoresist IP-L780 (Nanoscribe GmbH) is applied on a  $170\ \mu\text{m}$  thick coverslip (Gerhard Menzel GmbH, Germany), which is coated with a thin layer of aluminum oxide. The aluminum oxide enhances the refractive index contrast between the coverslip and the substrate enabling an easier detection of the corresponding interface. The coating is done with the aid of atomic layer deposition (R-200 Standard, Pico Sun Oy., Finland). After the printing process is finished, the sample is developed for about 45 min in propylene glycol methyl ether acetate and subsequently for 10 min in isopropyl alcohol. Eventually, the sample is cautiously blown dry using a nitrogen pistol.

For testing the capability of various self-developed bio-sourced photoresists, as presented in Ch. 6 and Ch. 7, a drop of the respective resist is sited on a coated coverslip using a syringe. Here, a specially prepared sample holder is used which allows for placing a second uncoated coverslip slightly above the first one, sandwiching the resist in-between. This is done to reduce the exposure of the resist to atmosphere, since moisture can trigger precipitation resulting in a turbid and hence unusable photoresist. To examine the printing quality, various structures at different writing speeds and laser powers are fabricated. In that, the laser power is given relative to the nominal value of  $57.8\ \text{mW}$  ( $= 100\%$ ), measured at the entrance aperture of the objective.

The NAG-based resists are developed in dimethyl sulfoxide (DMSO) for 90 min followed by acetone for 10 min. For the cellulose diacetate (CDA) derivatives the development routine is composed of 30 min acetone and 10 min isopropyl alcohol for CDA-SH 4-pentenoate resists as well as 10 min dimethyl formamide (DMF), 75 min acetone, and 5 min isopropyl alcohol for CDA-SH methacrylate resists. Finally, the samples are carefully blown dry with a nitrogen pistol, except for the bulky 3D

structures shown in Ch. 6 which are dried using a critical point dryer (EM CPD300, Leica Microsystems GmbH, Germany).

The chemicals used to prepare the photoresists were obtained from the suppliers listed below without any further purification. NAG was acquired from Alfa Aesar (USA). DMSO, isopropyl thioxanthone (ITX) and CDA (average  $M_n \sim 30,000$ , 39.8 wt% acetyl) were bought from Sigma-Aldrich (USA). Irgacure 369 and 819 as well as benzophenone were purchased from TCI Chemicals (Japan). DMF was obtained from VWR International (USA) and 7-diethylamino 3-thenoylcoumarin (DETC) was acquired from Acros Organics (Belgium).

### 3.2.2 Time-resolved light scattering spectromicroscopy

While the time-resolved electric field often bears important information, it is usually not accessible since detectors can only measure light intensity at optical frequencies. With the aid of Fourier transform spectral interferometry,<sup>203</sup> however, the phase information can be reconstructed from intensity measurements which allows for tracing the time-resolved electric field of light scattered from the studied sample.<sup>38,39</sup> Such a time-resolved light scattering spectromicroscopy experiment is therefore used in Ch. 5 to investigate different transport regimes in white beetle scales as well as fabricated DBS structures.

The corresponding experiment was set up in Walter Pfeiffer's group at Bielefeld University.<sup>38,39</sup> It is operated by Ruben C. R. Pompe, who has carried out the corresponding measurements as well as acquired and evaluated the experimental data.

As displayed in Fig. 3.7, the setup is in principle an interferometric experiment, which enables to modulate the time delay of the reference pulse relative to the pulse scattered from the sample. As a light source, a femtosecond Ti:sapphire laser (Femtosource Scientific, Femtolasers Produktions GmbH, Austria) is applied, which operates at a center wavelength of 780 nm with a spectral full width at half maximum of 47 nm (cf. Fig. 3.8a) and a repetition rate of 78 MHz. The emitted pulses first pass through a thin film polarizer to set a predefined polarization before being guided into a sample arm and a reference arm using a beam splitter.

In the sample arm a parabolic mirror (custom made, Jenoptik AG, Germany) is deployed to focus the laser beam onto the sample, which is mounted on a piezo stage (M-664.164, Physik Instrumente GmbH & Co. KG, Germany) to enable linear scanning of the excitation position across the sample. Additionally, the parabolic mirror collects and collimates the light scattered from the sample. Different scattering angles are thereby converted into lateral displacement, which allows the measured scattering angle to be selected with a beam block aperture (3 mm in diameter).

Using a second beam splitter, the scattered light pulse is overlapped with the reference pulse, while the relative time delay between both pulses can be adjusted with the delay line in the reference arm. In addition, the polarization of the reference

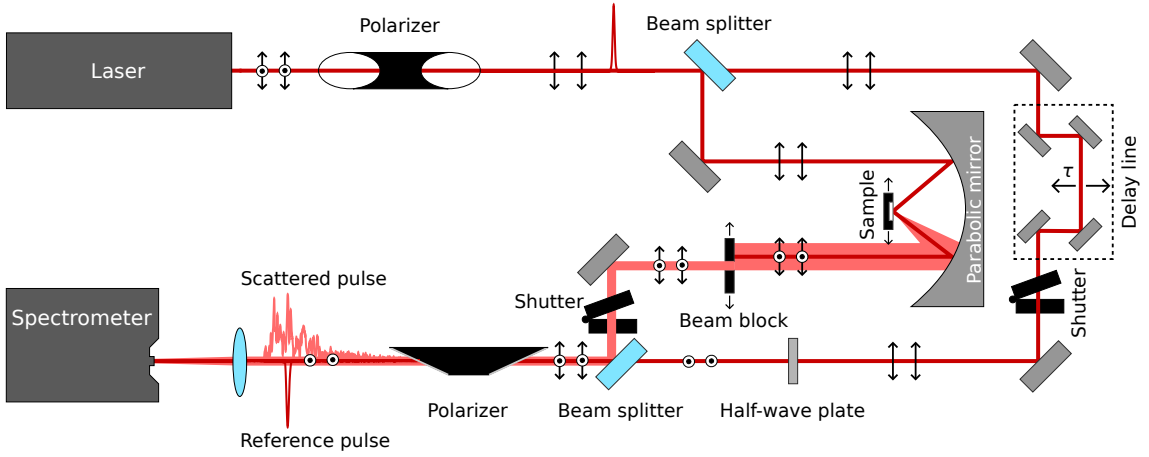


Figure 3.7: Scheme of the time-resolved light scattering spectromicroscopy experiment. The setup is basically an interferometric experiment recording the interference spectrum between the reference pulse and the pulse scattered from the sample in dependence of the time delay. From these data the time-resolved electric field of the scattered light can be reconstructed. Adapted from Ref. <sup>204</sup>

beam is rotated by  $90^\circ$  using a half-wave plate. When passing through a second thin film polarizer aligned perpendicular to the first polarizer, pure surface scattering is filtered out of the scattered pulse, i.e., scattering which preserves the initial polarization direction. In consequence, light scattering inside the sample becomes accessible for the analysis. Eventually, the interference spectrum arising from the superposition of both pulses is gathered with a spectrometer (USB 2000, Ocean Optics Inc., USA).

The spot size on the sample can be estimated by the diffraction limit, which is given as  $d_{\text{diff}} = 4\lambda_{\text{low}}f/\pi d_{\text{in}} = 2.4\ \mu\text{m}$  with the lower bound of the full width at half maximum  $\lambda_{\text{low}} = 735\ \text{nm}$ , the focal length of the parabolic mirror  $f = 15\ \text{mm}$ , and diameter of the incident beam  $d_{\text{in}} = 6\ \text{mm}$ . Performing a line scan across the sample, the minimum spot size can be alternatively obtained from the spatial width distribution of peaks in the measured interference spectra. As revealed in Fig. 3.8b, the diffraction limit is indeed in line with the drop in the spatial peak width distribution. Values below the diffraction limit are attributed to erroneous peak identification and fitting.

From the recorded interference spectra, the phase can be reconstructed as described below. Superposing the scattered pulse field  $|E_s|$  and the reference pulse field  $|E_r|$  yields the interference spectrum:

$$|E_s(\omega) + E_r(\omega)|^2 = |E_s(\omega)|^2 + |E_r(\omega)|^2 + E_s(\omega)E_r^*(\omega) \cos(\Delta\varphi(\omega)), \quad (3.25)$$

where the phase difference  $\Delta\varphi(\omega) = \delta\varphi + \omega\tau$  is composed of the phase  $\omega\tau$  introduced by the time delay between both interferometer arms and the phase difference  $\delta\varphi$  containing the relevant phase information.

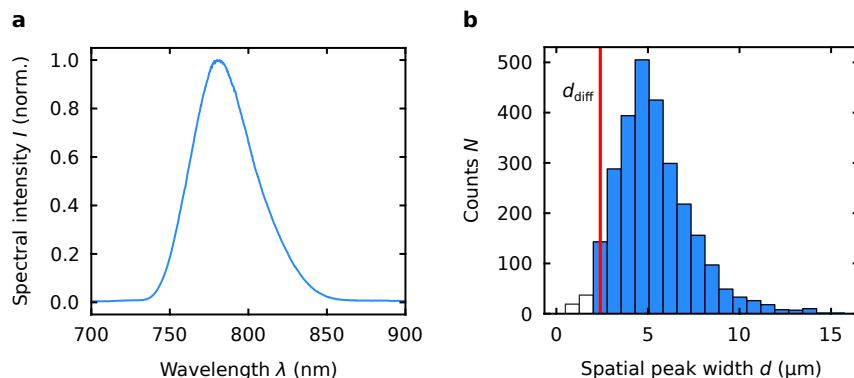


Figure 3.8: Characterization of the spectromicroscopy setup. **a**, Normalized excitation spectrum of the used laser source. **b**, Spatial peak width distribution obtained from line scans across a *Cyphochilus* scale and across the direct laser written DBS structure. In addition, the calculated diffraction limit of the spot size  $d_{\text{diff}}$  is shown as indicated by the red line. Adapted from Ref. <sup>204</sup>

Due to the linearity of the Fourier transform, the resulting spectrum is decomposed in parts related to  $|E_s(\omega)|^2 + |E_r(\omega)|^2$  and side bands  $E_s(\omega)E_r^*(\omega) \cos(\pm(\delta\varphi + \omega\tau))$ , centered around  $\pm\tau$ . By choosing an adequately large delay time  $\tau$ , one side band can be isolated in the Fourier spectrum. Thus,  $\delta\varphi = \varphi_r - (\varphi_s + \varphi_{\text{sample}})$  can be retrieved from the argument of the inverse transformed isolated side band, where  $\varphi_r$  and  $\varphi_s$  are the phases introduced by the respective interferometer arm. Performing a reference measurement without any sample, the phase difference introduced by the interferometer arms can be determined. This eventually allows to extract the phase introduced by the sample  $\varphi_{\text{sample}}$  and therefore the reconstruction of the time-resolved electric field.

To investigate the samples, i.e., a scale of beetle *Cyphochilus* and a direct laser written DBS structure, they are prepared on a microscope slide and mounted on the stage. As mentioned in Sec. 3.2.1, the DBS are printed on a  $d_{\text{cs}} = 170 \mu\text{m}$  thick coverslip, which possesses an index mismatch to the underlying microscope slide. In consequence, the reconstructed time signal of the scattered light shows a second pulse roughly 1.8 ps after the initial pulse, which results from the reflection at this interface. Indeed, the second pulse arises well behind the tail of the first pulse and coincides with the estimated time needed to travel back and forth in the coverslip ( $n_{\text{cs}} \approx 1.51$  for borosilicate glass at 780 nm)<sup>205</sup> given by  $t = 2d_{\text{cs}}n_{\text{cs}}/c_0 \approx 1.7$  ps. Hence, the time signal is filtered using a window function to suppress parasitic scattering from the mounting.

### 3.2.3 Non-linear absorption measurements

The principle of DLW is fundamentally based on (optical) non-linearity. Thus, to find appropriate photoinitiators the measurement of the respective two-photon absorption cross section is crucial. There are many different techniques to determine the two-photon absorption cross section which either rely on transmission

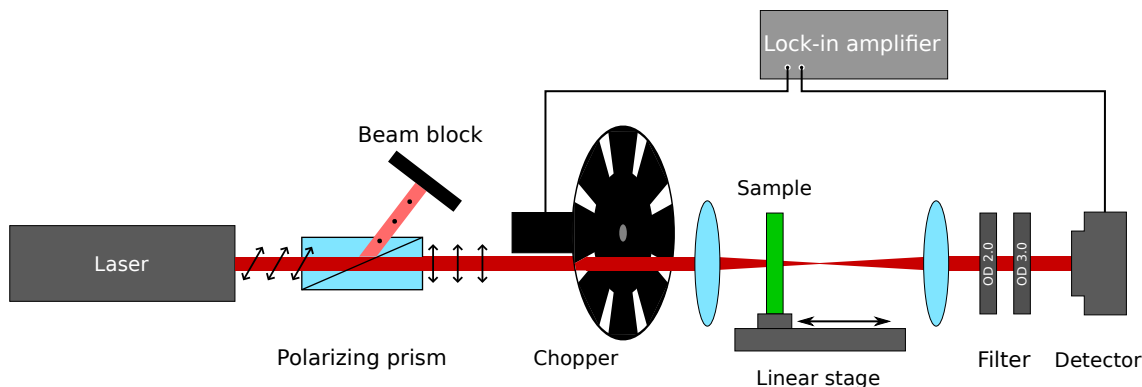


Figure 3.9: Scheme of the used  $z$ -scan setup to measure the two-photon absorption cross section. The sample is moved through the focal spot of a femtosecond laser beam (along the  $z$ -axis) while the position-dependent transmission through the sample is recorded with the detector.

measurements or on the evaluation of two-photon excited fluorescence.<sup>206–208</sup> While the latter requires considerably lower intensities compared to transmission measurements, its use is limited to fluorescent compounds and only relative cross sections are obtained.<sup>207,208</sup> Measuring absolute values demands time-consuming comparison with calibration samples to evaluate the respective fluorescence quantum yield.<sup>208</sup> In contrast, transmission measurements allow for determining the absolute two-photon absorption cross section directly.<sup>209</sup>

Therefore, the (open aperture)  $z$ -scan technique is applied here, which is based on recording the transmission through the sample as a function of the intensity. The intensity within the sample is varied by moving the sample along the axial direction (typically denoted as  $z$ -direction) through the focal spot of a femtosecond laser beam.<sup>208,210</sup> Since two-photon absorption depends on the intensity, a characteristic dip in transmittance is obtained for scan positions around the focal spot from which the two-photon absorption cross section can be retrieved.

The used experimental setup is shown in Fig. 3.9. As light source a tunable Ti:sapphire laser (Chameleon, Coherent Inc., USA) operating at a wavelength of 780 nm is deployed which delivers light pulses with a length of 314 fs<sup>a</sup> providing an output power of around 3.5 W at 80 MHz repetition rate. Hence, intensities sufficient to observe non-linear effects can be easily reached by focusing the beam.

For compounds showing a strong non-linearity, however, lower intensity might be used to avoid the occurrence of non-linear effects beyond two-photon absorption. For that reason, a rotatable Glan-Thompson polarizer (GTH10M, Thorlabs Inc., USA) is placed behind the laser which splits the incident beam into two beams, one being transmitted, and one being blocked. The intensity ratio between both beams can be smoothly adjusted via the angle between the optical axis of the polarizing prism and the polarization direction of the incident light.

<sup>a</sup>measured by E. Waller

The polarizer is followed by an optical chopper system with 50% duty cycle (MC2000, Thorlabs) which modulates the incident beam with a frequency of 400 Hz. Synchronizing the measured signal to that trigger frequency using a lock-in amplifier (SR830 DSP, Stanford Research Systems, USA) thus allows for suppressing parasitic background illumination in the received signal.

After passing the chopper, the beam is focused to the center of the travel range of a motorized stage (Soloist, Aerotech GmbH, Germany) using a 20 cm focal lens (LA1708-B, Thorlabs). On top of the stage, a cuvette with 1 mm path length (Hellma GmbH & Co. KG, Germany) is mounted which contains a solution of the sample under investigation. The light transmitted through the sample is collected by a second lens. To avoid overexposure, the collimated light is attenuated by neutral density filters before reaching the detector (DET36A2, Thorlabs).

In dependence of the scan position  $z$ , the power transmitted through the sample  $P_t$  is obtained via

$$P_t(z, t) = \frac{1}{2} \pi \omega_0^2 I_0(t) e^{-\alpha L} \ln \left( \frac{1 + q_0(z, t)}{q_0(z, t)} \right) \quad (3.26)$$

with the beam waist radius  $w_0$ , the intensity  $I_0(t)$  at the focus, obtained over the course of a light pulse, the linear absorption coefficient  $\alpha$ , and the sample thickness  $L$ .<sup>208,210</sup> In addition, the quantity  $q_0$  is given by

$$q_0(z, t) = \frac{\beta I_0(t) L_{\text{eff}}}{1 + (z^2/z_0^2)} \quad (3.27)$$

with the two-photon absorption coefficient  $\beta$ , the Rayleigh length  $z_0 = \pi \omega_0^2/\lambda$ , and the effective sample length  $L_{\text{eff}} = L(1 - e^{-\alpha L}/\alpha)$ .

In the case of temporally Gaussian pulses, the normalized energy transmittance is obtained by time integration:<sup>208,210</sup>

$$T(z) = \frac{1}{\sqrt{\pi} q_0(z, 0)} \int_{-\infty}^{\infty} \ln(1 + q_0(z, 0) e^{-\tau^2}) d\tau. \quad (3.28)$$

For  $|q_0| < 1$ , Eq. (3.28) can be conveniently expressed in terms of a summation:

$$T(z) = \sum_{m=0}^{\infty} \frac{(-q_0(z, 0))^m}{(m+1)^{3/2}}, \quad (3.29)$$

while only the first two terms are of interest.<sup>210</sup> If in addition  $\alpha \ll 1$  is true, the effective sample length is given by the actual sample length, resulting in the expression:<sup>208</sup>

$$T(z) = 1 - \frac{\beta I_0 L}{2^{3/2} (1 + (z^2/z_0^2))}. \quad (3.30)$$

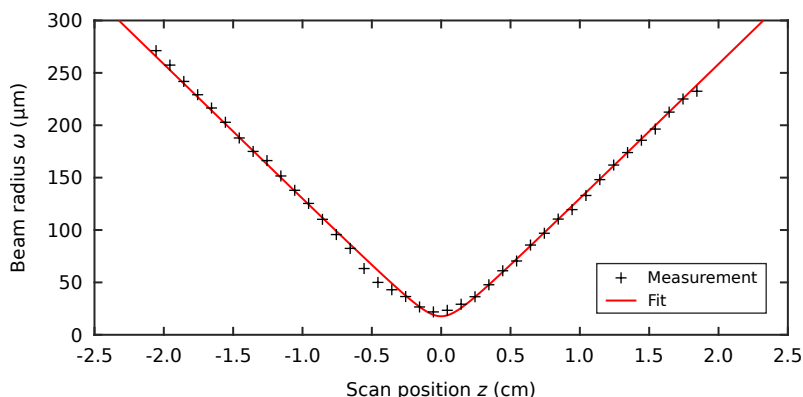


Figure 3.10: Determination of the axial beam profile around the focal spot. The profile is fitted with the hyperbolic relation describing a Gaussian beam (red line).

It should be noted that the transmittance is correctly described by Eq. (3.30) only if  $|q_0| < 1$  and  $L < z_0$  are satisfied. Hence, the experimental conditions must be chosen to fulfill these requirements, in particular the intensity might be lowered for compounds possessing a large two-photon absorption coefficient  $\beta$ .

The two-photon absorption cross section  $\sigma_2$  (in units of Goeppert Mayer with  $1 \text{ GM} = 10^{-50} \text{ cm}^4 \text{ s}$  per photon) is directly related to  $\beta$  via

$$\sigma_2 = \frac{\beta h \nu \times 10^3}{N_A c}, \quad (3.31)$$

where  $\nu$  is the frequency of the laser used,  $N_A$  is the Avogadro constant, and  $c$  is the concentration of the investigated compound in the solvent.<sup>208</sup>

To obtain  $\beta$  and therefore  $\sigma_2$  the measured transmittance is fitted with Eq. (3.30), where  $\beta$  is the fit parameter. The other quantities, namely  $I_0$  and  $z_0$  are fixed by the experimental setup and thus must be characterized first.

While the total power of the incident laser beam can be measured deploying a power meter, the calculation of the intensity at the focus requires the beam waist radius  $\omega_0$  as well as the pulse length and the repetition rate of the laser. Since the latter quantities are known, only the beam waist radius must be evaluated. From this, the Rayleigh length  $z_0$  can be directly retrieved too, as mentioned above.

Since the laser used emits a Gaussian beam, the waist radius can be obtained by determining the axial beam profile and fitting with the known hyperbolic relation:<sup>211,212</sup>

$$\omega(z) = \omega_0 \sqrt{1 + (z^2/z_0^2)}. \quad (3.32)$$

The beam profile is recorded by replacing the sample in the experimental setup (cf. Fig. 3.9) with a CCD camera and taking pictures of the beam cross section for different scan positions. Subsequently, the beam radius at every scan position is obtained by fitting the lateral profile with a Gaussian function. It should be

noted that the  $z$ -scan technique can also be expanded to use non-Gaussian beam shapes.<sup>213,214</sup> In the case of an arbitrary beam shape, however, the beam radius must be determined by the  $D4\sigma$  method.<sup>214</sup>

As exhibited in Fig. 3.10, the measured beam shape indeed follows that of a Gaussian beam given by Eq. (3.32) and a waist radius of  $\omega_0 = 17.2\ \mu\text{m}$  is obtained. Accordingly, a Rayleigh length of  $z_0 = 1.18\ \text{mm}$  is received. Hence, using a cuvette with a path length of  $L = 1\ \text{mm}$  satisfies the necessary condition  $L < z_0$ .

Since  $z$ -scan measurements are deployed to study the compounds which are used to mix bio-sourced photoresists, the respective suppliers can be found in Sec. 3.2.1. Additionally, Rhodamine 6G dissolved in methanol is taken as standard to validate the experimental setup. Rhodamine 6G was purchased from Acros Organics, while methanol (spectroscopy grade) was acquired from VWR International.



## 4 Effective refractive index calculation for composite media with large particles

In many cases, it is feasible to model the light transport in random media by treating the respective medium as an effective one. While this approach gives access to macroscopic transport properties, it demands the calculation of suitable averaged, i.e., effective, quantities such as an effective permittivity or permeability. In the case of small, non-magnetic particles the latter is almost unity, and the effective refractive index is straightforwardly received from the effective permittivity. However, for large particles, the magnetic multipole moments cannot necessarily be neglected, so both quantities must be taken into account.<sup>35,215</sup>

As mentioned before, there are several approaches to determine the effective permittivity, with the Maxwell–Garnett and Bruggeman mixing rules being among the best known and most frequently used. Their popularity might arise from their relatively simple form and the small number of required input parameters, which are the permittivities of the constituents and their respective volume fractions. On the downside, these mixing rules are restricted to grains much smaller than the wavelength of the incident light because of their inherent quasi-static character, as elucidated in Sec. 2.4.1 and 2.4.2, respectively. That means, the sphere size parameter  $x = ka$  (with the wavenumber  $k$  in the host medium and the particle radius  $a$ ) must be much smaller than one, as depicted in Fig. 4.1, left hand side. In addition, the Maxwell–Garnett mixing rule is derived for cermet topologies,<sup>155</sup> which further limits its applicability to certain structure types and small filling fractions in general.<sup>163</sup>

The Maxwell–Garnett theory is nevertheless regularly used to determine the effective permittivity for miscellaneous types of composite media including cermet patterns with large spheres<sup>216,217</sup> and even interconnected structures such as microporous media, foams or biological tissues.<sup>21,22,82,218,219</sup> Although viable values are obtained for some structures, the limitations of the method, in particular its restriction to small particles, are rarely met. Therefore, the accuracy of the predicted values often remains doubtful.

Since many composite media suffice the description as an effective medium but do not satisfy the condition  $x \ll 1$ , various extensions and generalized effective medium theories that allow for incorporating size effects are reported.<sup>155,164–166,220,221</sup> However, due to their limitation to a maximum sphere size parameter (or its equivalent in the case of non-cermet structures) between 0.5 and 1,<sup>35,221</sup> even with these extended theories only comparatively small particles can be treated, as illustrated in Fig. 4.1, center. In addition, most theories provide useful values only under certain conditions limiting their general applicability.<sup>35,158,222</sup>

In this chapter, 3D FDTD simulations are conducted to numerically study the effective refractive index of cermet patterns with large sphere sizes up to  $x \approx 2.5$

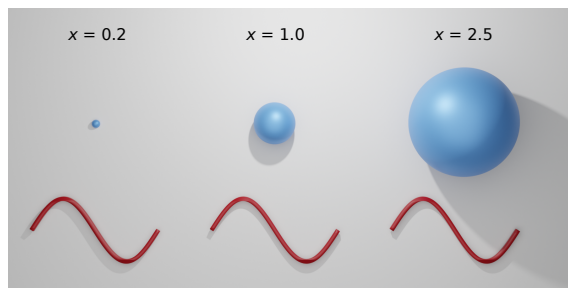


Figure 4.1: Sketch of different sphere size parameters. The size relation between the sphere (blue) and the wavelength is shown for a representative sphere size parameter in the Maxwell–Garnett domain ( $x = 0.2$ ), the upper bound of generalized theories ( $x = 1.0$ ) and the maximum sphere size studied in this thesis ( $x = 2.5$ ). Taken from Ref. <sup>225</sup> The figure is excluded from the CC BY license of this thesis.

(cf. Fig. 4.1, right hand side). Unlike other FDTD methods,<sup>221,223,224</sup> the proposed approach relies on the condition that the forward scattering amplitude of a spherical region of the composite medium vanishes if the refractive index of the background equals the effective refractive index of the composite.<sup>168,220</sup>

Below, after validating the simulation setup, it is used to show that the Maxwell–Garnett mixing rule is not suitable to predict the effective refractive index of composite media containing large particles correctly. Based on systematic investigation of size effects, a simple mixing rule is instead derived and tested, which is capable to calculate the effective refractive index in the so far inaccessible domain between  $x \approx 1$  and  $x \approx 2$ . At the current stage, the study is restricted to non-absorbing dielectric materials, which are found in many practical situations. However, the proposed simulation setup is not fundamentally limited to such materials but can be expanded to consider absorbing or metallic particles in a next step. The main results presented in this chapter are also published in Ref. <sup>225</sup>

## 4.1 Simulation setup and its validation

As mentioned above, the performed FDTD simulations are based on the circumstance that the forward scattering amplitude disappears in the case of a refractive index match between the homogeneous background and the effective medium. Since this condition directly follows from the generalized optical theorem,<sup>168,226</sup> it holds true, independent of the inner structure of the composite medium as long as the medium behaves as an effective one. In consequence, there is no fundamental restriction on the sphere size parameter, as it is also evident in the general derivation of this condition.<sup>168,220</sup>

Previous mixing rules deduced from this requirement are nevertheless limited to rather small sphere size parameters.<sup>168,220,227</sup> This constraint, however, arises from the issue to determine the forward scattering amplitude, which demands in analytic solutions some simplifications, e.g., considering only leading terms from Mie

theory.<sup>168,220</sup> In contrast, the approach presented here uses FDTD simulations, i.e., a full Maxwell solver, which take all relevant electric and magnetic multipole terms into account and thus treat arbitrary sphere sizes correctly.

To decrease the overall number of simulations, a further modification has been made. Since the average forward scattering amplitude is demanded to disappear, many (distinct) single particles are considered in the original approach to allow for averaging their individual forward scattering amplitudes. Straightforwardly transferring this concept to a simulation approach would thus result in a vast number of required simulations. This issue can be circumvented by embedding a spherical region of the composite medium containing both components at their exact volume fractions in the homogeneous background. Hence, the average forward scattering amplitude can be immediately received from a single simulation. This modification is valid since a spherical region of the composite medium exhibits the same forward scattering amplitude as a homogeneous sphere of same size consisting of the effective medium. This is verified for small sphere size parameters by Mallet *et al.*<sup>155</sup> and for large ones of  $x \approx 1.66$  by Yazhgur *et al.*<sup>216</sup>

In addition, this approach can also be used to determine the imaginary part of the effective refractive index. Since the imaginary part generally accounts for the attenuation of an impinging wavefront, it can be non-zero even for non-absorbing materials, due to scattering in the lateral direction. According to Mallet *et al.*, this attenuation can be considered by attributing absorption to the homogeneous effective sphere such that its extinction cross section equals the total scattering cross section of the composite.<sup>155</sup>

In Fig. 4.2a a cross section through the simulation setup is displayed. A spherical region of the composite medium which is composed of a host medium (pale blue) and inclusions (blue) is encased by a homogeneous background (pale red) of adjustable refractive index. In addition, the composite is surrounded by a total-field scattered-field light source (black), which allows only the scattered field outside the source, as explained in Sec. 3.1.1 and shown by the electric field distribution in Fig. 4.2b. While the light is predominantly scattered in forward direction, scattering in other directions also occurs as it can be seen in the corresponding logarithmic plot (see Fig. 4.2c). To obtain the far field projection of the scattered light in all directions, a box of monitors (red) is placed around the total-field scattered-field source.

The forward direction is thereby of particular interest. Since the polarization of the linear polarized incident field (vertical to the propagation direction) is preserved in the forward scattering direction, only one component of the electric field vector is unequal to zero. This component  $E_{\text{for}}$  is proportional to the forward scattering amplitude  $S(0^\circ)$ :<sup>228</sup>

$$E_{\text{for}} \sim E_0 \frac{e^{ikr}}{-ikr} S(0^\circ), \quad (4.1)$$

with the wavenumber  $k$ , the electric field  $E_0$  of the incident wave and the distance  $r$  between the scattering particle and the projected monitor plane (for details see Sec. 3.1.1). Although FDTD is actually a time-domain method, most software tools provide frequency-domain results by default, using monitors that directly Fourier transform the acquired time signal. In the frequency domain, however, the real field is given by the absolute value of the electric field. For this reason, the intensity  $I_{\text{for}}(\lambda) \sim |E_{\text{for}}(\lambda)|^2$  is used here for convenience.

According to the condition mentioned at the beginning, the effective refractive index can be retrieved from the simulation results by varying the background index in order to minimize Eq. (4.1). Indeed, as depicted in Fig. 4.2b,c the background index can be chosen such that forward scattering is suppressed. In this, it is found that around the point of index matching, the forward scattered intensity reveals a quadratic dependence as exemplarily shown for two different composite media in Fig. 4.2d,e. Thus, the effective refractive index is obtained from the minimum of the parabola fitted to the simulation data. While the intensity at the minimum is expected to be zero, a small offset is observed instead, due to unavoidable numerical errors.

As a primary test, a single sphere is placed in the simulation layout while the background index is set to one. For this configuration the forward scattered intensity can be also analytically computed using Mie theory (see e.g., Ref. <sup>228</sup>) and thus compared to the FDTD results. For a sphere with a radius of 100 nm and a refractive index of  $n_i = 1.5$ , the numerical results (black, dashed curve) are displayed beside the analytic results (green curve) in Fig. 4.3a, revealing a perfect agreement over the entire range of investigated wavelengths.

Additionally, the ability of the setup to accurately predict the effective refractive index must be verified. This is done by generating random sphere packings of small spheres, i.e., with a sphere size parameter in the Maxwell–Garnett regime, for different filling fractions  $f$  between 10% and 60% applying the force-biased sphere packing algorithm as presented in Sec. 3.1.3. From each generated packing at least five distinct spherical regions are excised, which exhibit a filling fraction equal to that of the whole sphere packing. The same size of the extracted region is thereby applied for all filling fractions, ensuring that for the lowest filling fraction five spheres are part of the extraction. Eventually, the effective refractive index is received by averaging the values obtained from different extracted regions.

In Fig. 4.3b, the FDTD outcomes (black crosses) are shown for a sphere packing with  $x = 0.314$  and a refractive index of the inclusions of  $n_i = 1.3$ , using a wavelength of 1000 nm. The host medium is here and below (unless otherwise noted) assumed to be vacuum, i.e., the refractive index of the host is  $n_h = 1.0$ . In addition, the prediction of the Maxwell–Garnett (MG) mixing rule calculated with Eq. (2.30) is displayed (blue line). As presumed for a cermet topology in the Maxwell–Garnett regime, the simulation results are in excellent accordance with the Maxwell–Garnett theory, verifying the proposed simulation layout.

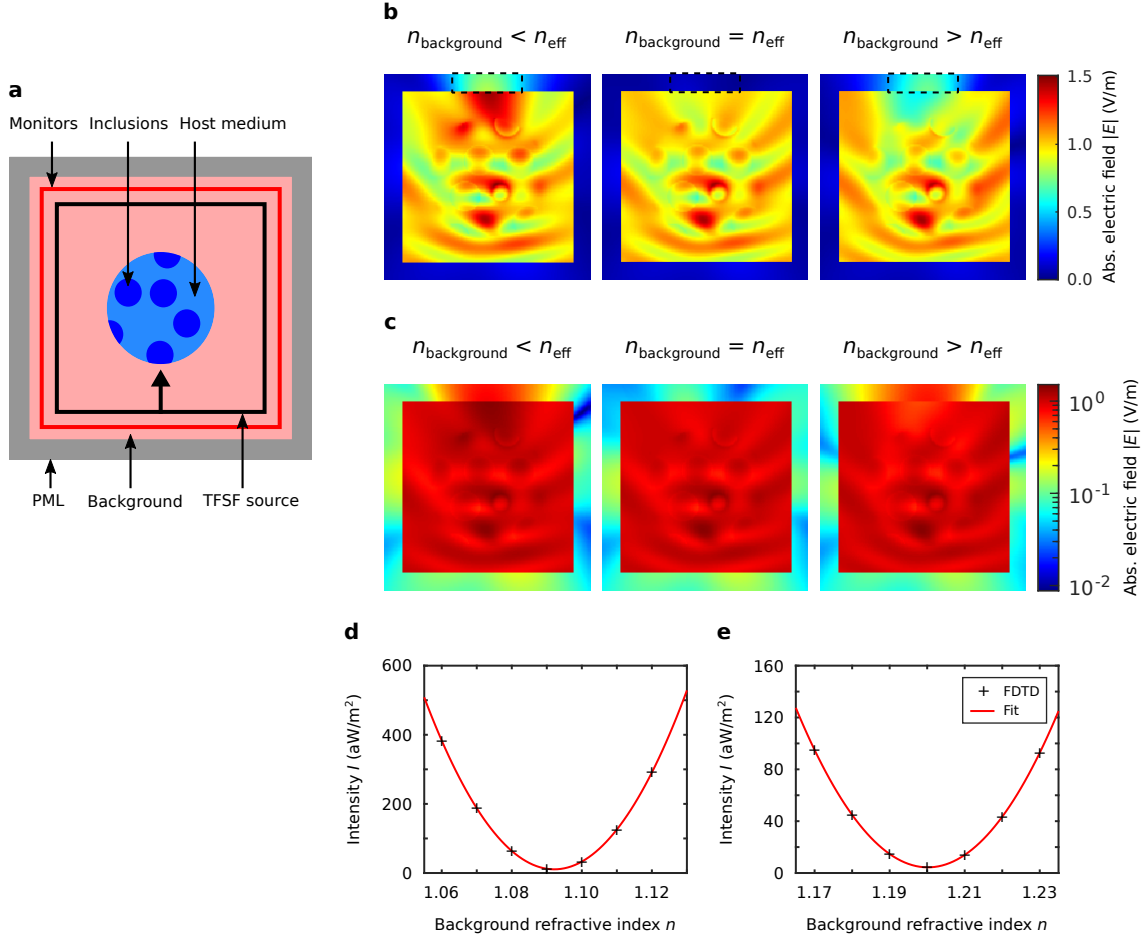


Figure 4.2: Simulation layout to compute the effective refractive index. **a**, 2D cross section of the 3D simulation setup. The layout comprises a homogeneous background medium (pale red) limited by PML boundaries, which encloses the composite medium (host medium, pale blue and inclusions, blue). The composite is furthermore surrounded by a total-field scattered-field source (TFSF, black) that injects a plane wave at its lower edge. The far field projection of the scattered field is obtained from a box of monitors (red). **b**, Absolute electric field within the cross section, exhibited for three distinct background indices. In the case of an index mismatch, pronounced forward scattering is observed, as indicated by the black, dashed box. **c**, same as **(b)** but plotted on a logarithmic scale revealing contributions to scattered light apart from the forward direction. **d,e**, Forward scattered intensity in dependence of the background index for a sphere packing with  $x = 1.62$ , a refractive index of  $n_i = 1.3$ , and a filling fraction of  $f = 30\%$  (**d**) as well as  $x = 1.26$ ,  $n_i = 1.5$ , and  $f = 40\%$  (**e**). In both cases, the results can be fitted with a parabolic curve (red) in perfect agreement. Adapted from Ref. <sup>225</sup>

To test the capability of the simulation geometry to yield the imaginary part of the effective refractive index too, a spherical region of the composite medium is placed in vacuum to determine its scattering cross section. Then, this value is compared to the extinction cross section obtained for a homogeneous effective sphere of same size. For small spherical regions no considerable difference is found, since only a single scattering event occurs on average, i.e., the dimension of the region is smaller

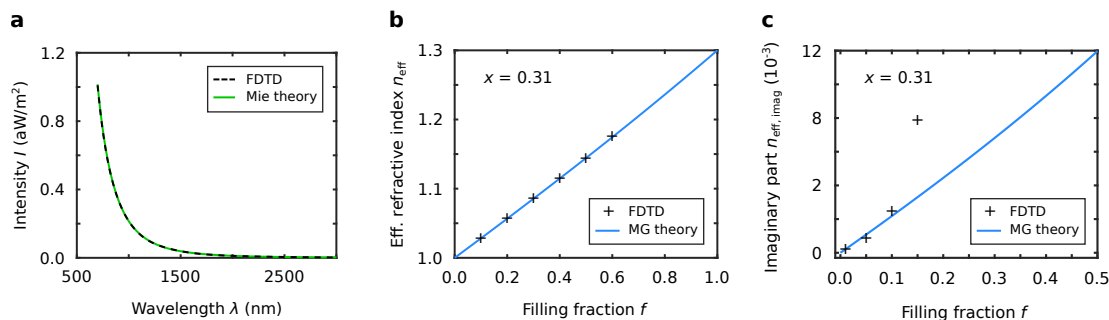


Figure 4.3: Validation of the simulation setup. **a**, Comparison between the forward scattered intensity of a single sphere ( $a = 100$  nm,  $n_i = 1.5$ ) computed using FDTD simulations (black, dashed line) and Mie theory (green line). **b**, Effective refractive index of sphere packings at various filling fractions (black crosses), obtained with the simulation setup shown in Fig. 4.2a. The outcomes are in excellent accordance with the Maxwell–Garnett theory (blue line). For the calculations, a wavelength of 1000 nm and  $n_i = 1.3$  are used. **c**, Corresponding determination of the imaginary part of the effective refractive for sphere packings with  $n_i = 1.5$ . For filling fractions below 10% the FDTD results are consistent with the prediction of the complex Maxwell–Garnett theory. Adapted from Ref. <sup>225</sup>

than the scattering mean free path, such that lateral scattering hardly emerges. In contrast, for spherical regions that are large compared to the wavelength (here 4  $\mu\text{m}$  in diameter), the extinction cross section of the effective sphere is indeed smaller than the scattering cross section. This mismatch can be eliminated by assigning absorption to the effective sphere resulting in a complex effective refractive index.

Applying this approach, the corresponding imaginary part for sphere packings with  $x = 0.314$  and  $n_i = 1.5$  is shown in Fig. 4.3c. These calculations can be compared to the complex version of the Maxwell–Garnett mixing rule, which is received by inserting the electrostatic polarizability of a sphere complemented by radiative corrections

$$\tilde{\alpha} = \alpha_0 \left( 1 + \frac{2i}{3} \frac{\epsilon_i - 1}{\epsilon_i + 2} x^3 \right) =: \alpha_0 \left( 1 + \frac{2i}{3} \beta_i x^3 \right), \quad (4.2)$$

in the Clausius–Mossotti formula (2.27), where  $\alpha_0$  is given by Eq. (2.28). The resulting complex Maxwell–Garnett formula reads

$$\epsilon_{\text{MG}} = 1 + 3f \frac{\beta_i}{1 - \beta_i f} \left( 1 + \frac{2i}{3} x^3 \frac{\beta_i}{1 - \beta_i f} \right), \quad (4.3)$$

which reduces for  $x = 0$  to the common Maxwell–Garnett mixing rule, given by Eq. (2.30).<sup>155</sup>

For small filling fractions the prediction of the complex Maxwell–Garnett theory (Fig. 4.3c, blue line) agrees with the values gained by FDTD simulations. However, Eq. (4.3) is only valid for small filling fractions,<sup>155</sup> thus for larger values significant deviations are presumed as also observed here above 10% filling fraction.

## 4.2 Derivation of a mixing rule applicable to large particles

The deduction of a mixing rule for large particles demands a systematic investigation of size effects on the effective refractive index. Since the size parameter  $x = 2\pi n_h a / \lambda$  depends on the particle radius  $a$  and the wavelength  $\lambda$ , both quantities can be tuned to vary  $x$ . Here, sphere size parameters between  $x = 0.90$  and  $x = 2.51$  are implemented by generating random sphere packings with various radii, as described in Sec. 3.1.3. Thereby, a wavelength of 700 nm is applied in the majority of simulations, which is partly diminished to reach the largest sphere size parameters.

Deploying the introduced simulation setup, the resulting effective refractive index for a sphere packing with  $x = 1.80$  and  $n_i = 1.7$  (Fig. 4.4a, black crosses) exhibits notable deviations from the Maxwell–Garnett mixing rule (blue line). This demonstrates that the latter is unable to accurately compute the effective refractive index for large particles. In contrast, as shown by the green dashed curve in Fig. 4.4a, the results can be well fitted with a quadratic polynomial function.

As it can be seen in Fig. 4.4b-d, the discrepancy between the effective refractive index and the Maxwell–Garnett mixing rule grows with increasing sphere size parameter and refractive index contrast. In all cases, however, the received trend can be fitted to a good approximation with a quadratic polynomial. In this, two reasonable assumptions are made regarding the bounds of the filling fraction. Since the composite reduces to the host medium in the case of  $f = 0$ , the effective refractive index should equal the index  $n_h$  of the host. Accordingly, in the limit of  $f = 1$ , the effective refractive index is given by that of the inclusion medium, i.e.,  $n_i$ .

On the basis of these insights, a quadratic polynomial given by

$$n_{\text{eff,large}}(f) = p_1 f^2 + p_2 f + p_3, \quad (4.4)$$

is the starting point of the derivation of a novel mixing rule, with the yet undetermined coefficients  $p_1$ ,  $p_2$ , and  $p_3$ . However, with aid of the boundary conditions for  $f = 0$  and  $f = 1$ :

$$n_{\text{eff,large}}(0) = p_3 = n_h, \quad (4.5a)$$

$$n_{\text{eff,large}}(1) = p_1 + p_2 + p_3 = n_i, \quad (4.5b)$$

two coefficients, namely  $p_2$  and  $p_3$ , can be fixed.

Therefore, retrieving a mixing rule for large particles reduces to the issue of finding a proper expression for  $p_1$ , which is done by comparison with the Maxwell–Garnett mixing rule. As it can be seen in Fig. 4.4a, the shape of the Maxwell–Garnett curve is also similar to a parabola. Indeed, the second order Taylor expansion calculated around  $f = 0.5$  (Fig. 4.5a, black dashed line) agrees well with the Maxwell–Garnett curve (blue line). However, close to the bounds of the filling fraction range some

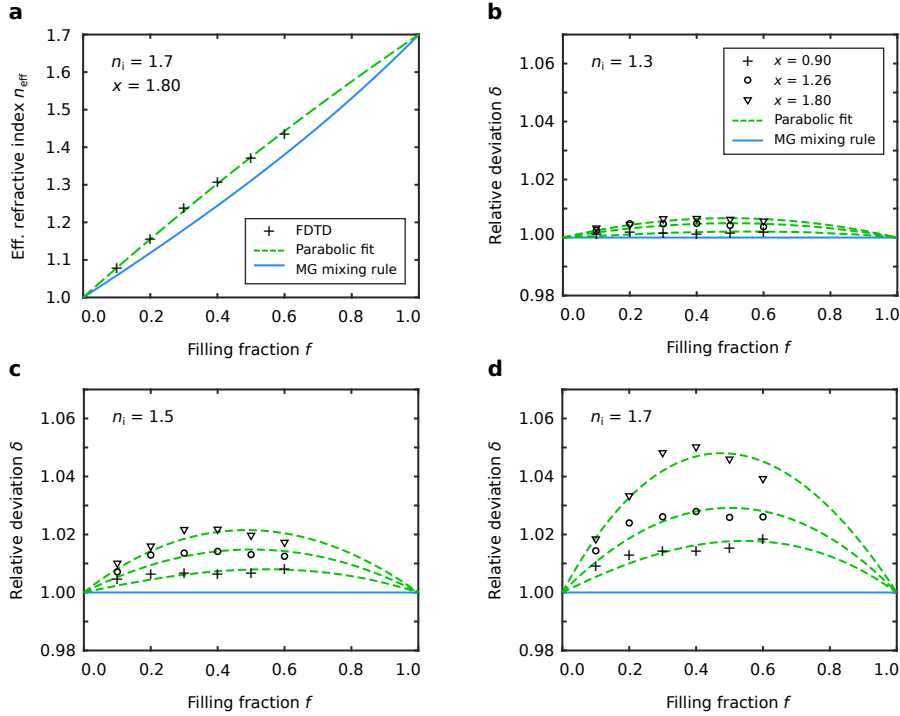


Figure 4.4: Effective refractive index behavior in dependence of the particle size. **a**, Effective refractive index (black crosses) obtained by FDTD simulations for a sphere packing with  $x = 1.80$  and  $n_i = 1.7$  in relation to the Maxwell–Garnett mixing rule (blue line). In addition, a parabola (green, dashed line) is fitted to the simulation results. **b–d**, Deviation of the simulation outcomes and the respective parabolic fits from the prediction of the Maxwell–Garnett mixing rule for various sphere size parameters and refractive index contrasts of 1.3 (**b**), 1.5 (**c**), and 1.7 (**d**). All quantities are scaled according to the normalized Maxwell–Garnett mixing rule, so the relative deviation  $\delta$  from the Maxwell–Garnett mixing rule is revealed. Taken from Ref. <sup>225</sup> The figure is excluded from the CC BY license of this thesis.

deviations are observed (cf. Fig. 4.5a, inset), i.e., the boundary conditions stated above are not satisfied. While these boundary conditions are a fundamental prerequisite of the novel mixing rule, an approximation of the Maxwell–Garnett mixing rule must fulfill them to allow for comparison. Moreover, it is useful to set the value of the approximation at  $f = 0.5$  to the value of the Maxwell–Garnett mixing rule, as it is the case with the Taylor expansion. The approximation therefore is given by

$$n_{\text{MG,approx}}(f) = p_{1,\text{MG}}f^2 + p_{2,\text{MG}}f + p_{3,\text{MG}}, \quad (4.6)$$

with

$$n_{\text{MG,approx}}(0) = p_{3,\text{MG}} = n_h, \quad (4.7a)$$

$$n_{\text{MG,approx}}(0.5) = \frac{1}{4}p_{1,\text{MG}} + \frac{1}{2}p_{2,\text{MG}} + p_{3,\text{MG}} = n_{\text{MG}}(0.5), \quad (4.7b)$$

$$n_{\text{MG,approx}}(1) = p_{1,\text{MG}} + p_{2,\text{MG}} + p_{3,\text{MG}} = n_i, \quad (4.7c)$$



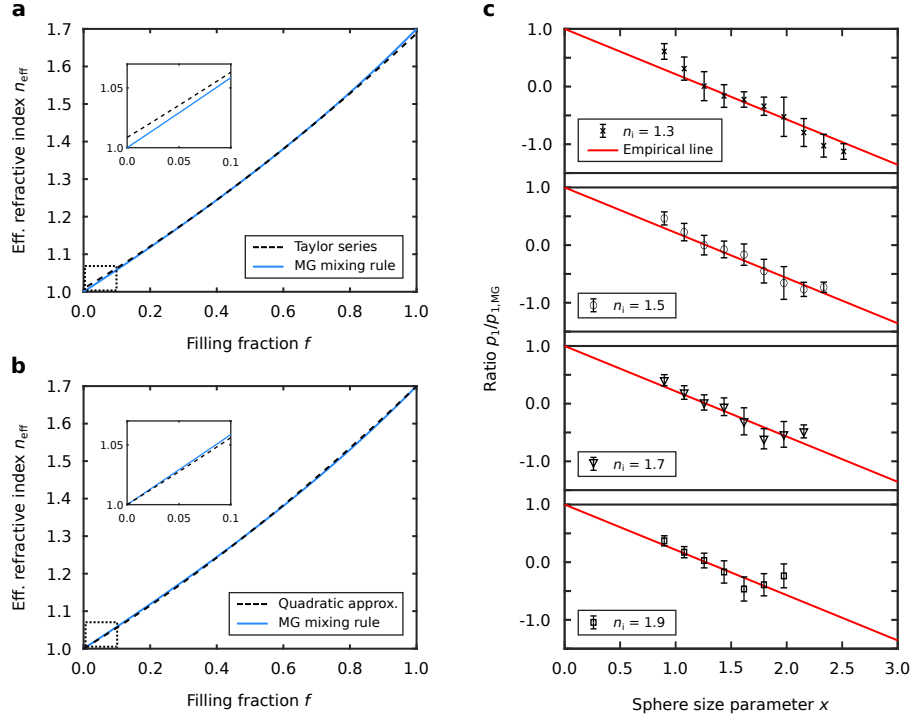


Figure 4.5: Parameter determination for the mixing rule applicable to large particles. **a**, Maxwell–Garnett mixing rule for a refractive index of  $n_i = 1.7$  (blue curve) in relation to its second order Taylor expansion around  $f = 0.5$  (black, dashed curve). The inset displays an enlarged view of the region around the lower bound (marked by the dotted box). **b**, Respective comparison between the Maxwell–Garnett mixing rule and the quadratic approximation (black, dashed line). A close-up of the indicated area is shown as inset. **c**, Ratio  $p_1/p_{1,MG}$  in dependence of the sphere size parameter  $x$  for sphere packings with  $n_h = 1$  and  $n_i = 1.3$ ,  $n_i = 1.5$ ,  $n_i = 1.7$ , and  $n_i = 1.9$ , respectively. The error bars represent the 95% confidence interval of the fits. The empirically obtained linear function (red line) is displayed in addition, revealing that the ratio shows the same tendency within the scope independent of the refractive indices  $n_i$ . Taken from Ref. <sup>225</sup> The figure is excluded from the CC BY license of this thesis.

which straightforwardly results in the coefficients  $p_{1,MG}$ ,  $p_{2,MG}$ , and  $p_{3,MG}$ . Applying these coefficients in Eq. (4.6), indeed yields an approximation in excellent accordance with the Maxwell–Garnett mixing rule while satisfying the boundary conditions (see Fig. 4.5b).

As it can be discerned in Fig. 4.4 the coefficient  $p_1$  relates to  $n_i$  and  $x$ . However, considering the ratio  $p_1/p_{1,MG}$  instead of  $p_1$ , the explicit dependence on  $n_i$  can be circumvented, at least between  $x \approx 1$  and  $x \approx 2$  defining the scope of the novel mixing rule. Indeed, the ratio  $p_1/p_{1,MG}$  follows the same trend for distinct  $n_i$  as shown by the red line in Fig. 4.5c. That means, the mixing rule for large spheres possesses the same dependence on  $n_i$  than the Maxwell–Garnett mixing rule does. In the validity range, an empirical linear function is found that determines the

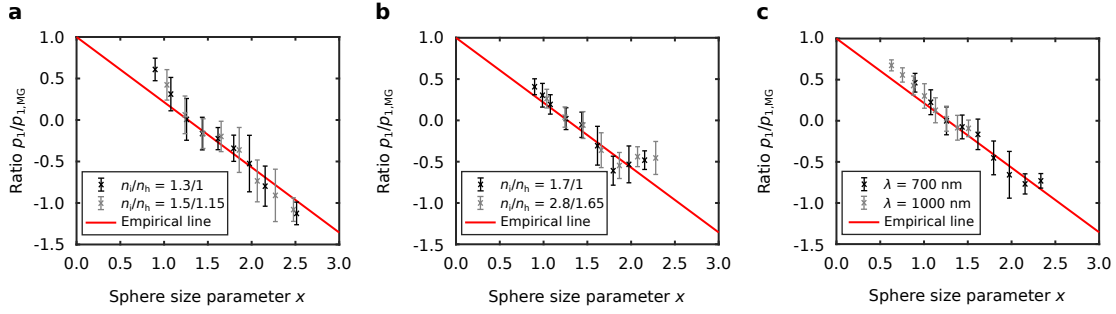


Figure 4.6: Effect of the refractive index contrast and the applied wavelength. **a,b**, Ratio  $p_1/p_{1,MG}$  for two different refractive index configurations yielding the same index contrast of  $n_i/n_h = 1.3$  (**a**) and  $n_i/n_h = 1.7$  (**b**), respectively. **c**, Ratio  $p_1/p_{1,MG}$  for two different wavelengths of the incident light, namely 700 nm and 1000 nm. In all cases, the ratio follows the empirically found linear trend (red line). Adapted from Ref. <sup>225</sup>

relationship between  $p_1/p_{1,MG}$  and the sphere size parameter:

$$\frac{p_1}{p_{1,MG}} = 1 - \frac{\pi}{4}x, \quad (4.8)$$

as exhibited by the red line in Fig. 4.5c. Inserting  $p_{1,MG} = 2n_i + 2n_h - 4n_{MG}(0.5)$  in Eq. (4.8), the previously unknown parameter  $p_1$  is obtained. Therefore, within the scope  $x \approx 1$  to  $x \approx 2$ , the mixing rule applicable to large particles reads

$$n_{\text{eff},\text{large}}(f) = \left(1 - \frac{\pi}{4}x\right) \cdot (2n_i + 2n_h - 4n_{MG}(0.5))f^2 + (n_i - n_h - \left(1 - \frac{\pi}{4}x\right) \cdot (2n_i + 2n_h - 4n_{MG}(0.5)))f + n_h. \quad (4.9)$$

Up to this point, the host medium is assumed to be vacuum, however, the validity of the empirical formula (4.8) is not compromised by  $n_h \neq 1$  or the choice of wavelength, as exemplarily shown in Fig. 4.6. This verifies the mixing rule for large particles in its general form as stated above.

### 4.3 Limitations of the mixing rule

Hereinafter, the limitations of the mixing rule applicable to large particles are examined. Constraints can be either caused by the size of the contained particles or by the general structure of the composite medium.

Effective medium formulations are predominantly found for two different structure types. On the one hand, there are random materials where multiple scattering enables to describe light transport by means of diffusion theory. For such media, e.g., random sphere packings, the here presented mixing rule is developed and for further representatives of this group tested in the following section.

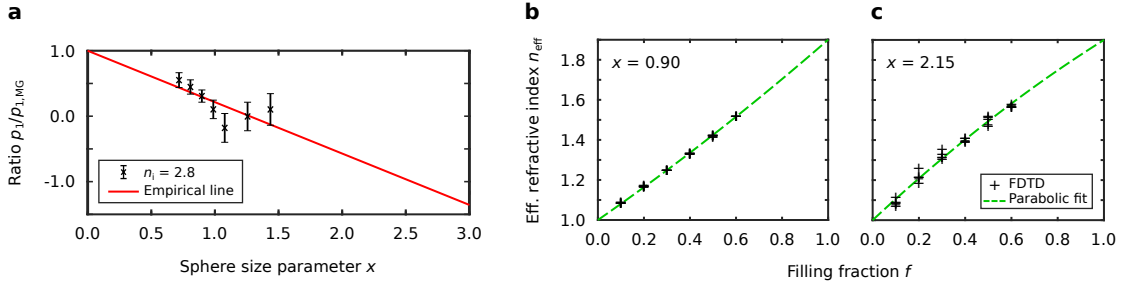


Figure 4.7: Limits of the mixing rule for large particles. **a**, Ratio  $p_1/p_{1,MG}$  for a large refractive index contrast of 2.8. **b,c**, Effective refractive index calculated for five distinct spherical regions extracted from the same sphere packing with  $x = 0.90$  (**b**) and  $x = 2.15$  (**c**). In both cases, the refractive index contrast is 1.9. Taken from Ref. <sup>225</sup> The figure is excluded from the CC BY license of this thesis.

On the other hand, effective medium descriptions can be partly used for ordered media with unit cells in the order of the wavelength, for instance, photonic crystals and metamaterials.<sup>229</sup> However, for such structures the assumption of an effective medium is usually valid only under strict conditions, for example, for a certain incident angle or frequencies below the first stop band.<sup>229,230</sup> Accordingly, the effective quantities of metamaterials are typically obtained from the complex reflection and transmission coefficients received for the entire structure under a particular incident angle.<sup>231,232</sup> The here presented approach contrarily relies on information retrieved from a spherical region extracted from the entire structure. Therefore, the mixing rule for large spheres might provide useful results for some metamaterials but could also show severe errors for others. So, it must be carefully tested for every ordered structure it is applied to.

Nevertheless, as revealed in Sec. 4.4, the novel mixing rule is believed to deliver suitable predictions for a great variety of disordered materials. For these structure types, restrictions primarily relate to the particle size since the empirical formula reflects the trend of the ratio  $p_1/p_{1,MG}$  only between  $x \approx 1$  and  $x \approx 2$ . As it can be discerned in Fig. 4.6a,b the course of the ratio  $p_1/p_{1,MG}$  depends on the refractive index contrast  $n_i/n_h$  rather than the actual values of  $n_i$  and  $n_h$ . Thus, only the index contrast must be taken into account in the following discussion.

In the limit of vanishing particle size  $x \rightarrow 0$ , the mixing rule for large particles is equal to the quadratic approximation of the Maxwell-Garnett mixing rule, as expected. The Maxwell-Garnett theory, however, is valid as long as the electrostatic dipole polarizability suffices to describe the polarizability of the particle (cf. Sec. 2.4.1). For that reason, it is suitable even for non-vanishing sphere sizes, as exemplarily shown for  $x \approx 0.3$  in Fig. 4.3b. In consequence, the ratio  $p_1/p_{1,MG}$  remains one in the electrostatic regime and starts to decrease afterwards. The empirical formula, in contrast, predicts a constant decay for  $x > 0$ , which leads to an underestimation of the ratio in vicinity of the electrostatic regime and thus provides a lower bound on the scope. In the case of small index contrasts, the electrostatic

description stays valid for larger particles, so this behavior is more distinct for low index contrasts, as it can be observed in Fig. 4.5c.

On the other side of the scope, it is found that the ratio only decreases to a particular point from where it remains constant or even grows and thus deviates from the empirical formula. For increasing index contrast this point moves to lower sphere size parameters, which restricts the scope to  $x \lesssim 2$  for index contrasts up to  $n_i/n_h = 2$ . As shown in Fig. 4.7a for  $n_i/n_h = 2.8$ , the scope is further reduced by enlarging the index contrast beyond this limit.

To explain the occurrence of the upper limit, different regions extracted from the same sphere packing must be considered. As expected for a small sphere size parameter within the scope (Fig. 4.7b), the received effective refractive indices hardly differ for various extracted regions. In contrast, performing a similar analysis in the case of sphere size parameters beyond the scope, a significant variance can be noticed, as exhibited in Fig. 4.7c. Thus, it can be concluded that the specific arrangement of spheres defines the scattering behavior, revealing that the assumption of an effective medium becomes generally invalid in that case.

#### 4.4 Comparison to other mixing rules and potential applications

To assess the capability of the here derived mixing rule, its prediction is tested for different structures falling within its validity range as well as compared to the outcomes of renowned mixing rules. Initially, a sphere packing with large sphere size parameter of  $x = 1.71$  and refractive index contrast of 1.9 is considered. As expected for this geometry, the novel mixing rule (computed with Eq. (4.9)) describes the effective refractive index in good approximation over a wide range of filling fractions (Fig. 4.8, green line). The Maxwell–Garnett and Bruggeman mixing rules, in contrast, underestimate the effective refractive index considerably, as shown in Fig. 4.8 by the blue dashed and the black dotted line, respectively. For the Maxwell–Garnett theory deviations as large as  $\Delta n = 0.1$  are found for filling fractions between 30% and 60%. In this range, the prediction of the Bruggeman mixing rule is better, nevertheless, there is still a discrepancy of around  $\Delta n = 0.05$  to the actual values.

Unlike the Maxwell–Garnett theory, the Bruggeman theory is symmetric, as explained in Sec. 2.4.2. It is therefore able to treat arbitrary filling fractions correctly, at least in principle, which leads to better results for large filling fractions, in agreement with observations. However, none of the classical mixing rules can accurately estimate the effective refractive index, which is only done by the here derived mixing rule for large particles.

So far the investigated structures are limited to random sphere packings. While these structures are a great test bed for systematically studying size effects, the assumption of non-interconnected spheres of equal size holds only for a minority of

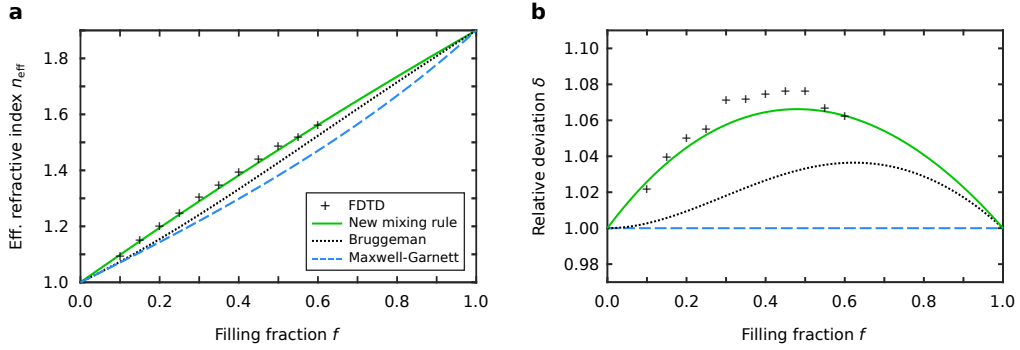


Figure 4.8: Comparison of various mixing rules. **a**, The effective refractive index received for a sphere packing with  $x = 1.71$  and  $n_i = 1.9$  is compared to the results of the mixing rule for large particles (green line), the Bruggeman mixing rule (black, dotted line), and the Maxwell–Garnett mixing rule (blue, dashed line). **b**, Same as **(a)** but all quantities are presented as relative deviation  $\delta$  from the prediction of the Maxwell–Garnett mixing rule for better visibility. Taken from Ref. <sup>225</sup> The figure is excluded from the CC BY license of this thesis.

composite media. In reality, such media often contain a disordered, interconnected structure with various feature sizes, as found for example in countless biological tissues.<sup>71</sup> Hence, the results of different mixing rules should be also compared for more realistic, interconnected patterns.

Such a complex, interconnected structure is found, e.g., in the brilliant white scales of beetle *Cyphochilus* (cf. Sec. 2.2.1). However, for testing different mixing rules, the DBS structure is used instead, since this model can be easily modified to investigate various configurations. As presented in Sec. 2.2.2, the model relies on a small set of parameters, defining the underlying normal distribution of the layer thickness and in consequence the filling fraction  $f$  of the entire structure. The normal distribution is given by its mean value  $\mu$  and standard deviation  $\sigma$ , while it is truncated outside of the interval  $I$ .

In Tab. 4.1 the effective refractive indices obtained by FDTD simulations is shown for various configurations of the DBS model. In this, the same procedure is applied as for random sphere packings, i.e., spherical regions are extracted from the entire structure and the respective forward scattering amplitude is minimized by adjusting the background refractive index. In addition, the received results are compared to the predictions of the mixing rule for large particles, the Maxwell–Garnett and Bruggeman mixing rules. The sphere size parameter required to evaluate the mixing for large particles, is obtained from a sphere that possesses the same volume as a cuboid with a thickness of  $\mu$ , i.e., an average cuboid of the DBS model.

As it can be seen in Tab. 4.1, the results of the mixing rule for large particles indeed agree well with the actual effective refractive index for all studied size distributions, filling fractions and refractive indices. Contrarily, the classical mixing rules exhibit significant deviations, showing their inability to predict an accurate value. As also observed above, the Bruggeman mixing rule slightly outperforms

Table 4.1: Comparison between the effective refractive index of the DBS model and the results of various mixing rules. The normal distribution of the layer thickness is characterized by the mean value  $\mu$ , the standard deviation  $\sigma$  and the interval  $I$  of the used thicknesses. A refractive index of  $n_i$  is used and  $f$  denotes the respective filling fraction. The effective refractive index  $n_{\text{FDTD}}$  obtained by FDTD simulation is given beside the predictions of the mixing rule for large particles  $n_{\text{eff,large}}$ , the Bruggeman mixing rule  $n_{\text{BG}}$ , and the Maxwell–Garnett mixing rule  $n_{\text{MG}}$ . Adapted from Ref. <sup>225</sup>

$n_i$	$\mu$ (nm)	$\sigma$ (nm)	$I$ (nm)	$f$	$n_{\text{FDTD}}$	$n_{\text{eff,large}}$	$n_{\text{BG}}$	$n_{\text{MG}}$
1.5	190	80	[50, 330]	25%	1.126	1.127	1.116	1.113
1.5	230	160	[50, 410]	30%	1.151	1.153	1.141	1.136
1.5	370	160	[190, 550]	40%	1.210	1.207	1.191	1.183
1.7	130	80	[50, 210]	15%	1.115	1.105	1.092	1.088
1.7	190	80	[50, 330]	25%	1.179	1.179	1.158	1.149

the Maxwell–Garnett mixing rule. This is consistent with expectations, since the Maxwell–Garnett mixing rule is originally developed for cermet topologies, in sharp contrast to the here investigated DBS model.

Altogether, this implies that the novel mixing rule is not just able to incorporate size effects correctly but can be also applied for various structure types, ranging from cermet topologies to more realistic interconnected structures. Therefore, the presented mixing rule may find application in several fields.

Beside white beetle scales, scattering and whiteness optimization is generally an issue of wide interest,<sup>18,19,86,233</sup> usually demanding the calculation of effective quantities in structures where size effects cannot be neglected. Indeed, white paint formulations typically feature sphere size parameters and refractive index contrasts in the order of 1.8, hence in the validity range of the novel mixing rule.<sup>18</sup>

Moreover, the mixing rule for large particles might be also useful in other areas considering the interaction of light with complex media, e.g., in opto-biomedical context. As recently reported, it is possible to differentiate between benign and malignant tissue based on the corresponding effective refractive index, even at an early stage of the cancerous disease.<sup>234,235</sup> To unambiguously identify the size of the tumor, exact calculation of the effective refractive index is required, which demands a higher precision than obtained with the currently used Maxwell–Garnett mixing rule,<sup>235</sup> especially when size effects cannot be neglected. This is the case in many approaches where THz radiation is used for diagnostics. The wavelength range in the THz regime (roughly 3 mm to 40  $\mu\text{m}$  for 0.1–7 THz) is partially in the same order than human cells (10–100  $\mu\text{m}$ )<sup>236</sup> while refractive index contrasts between benign and malignant tissue can be as high as 1.8 in this frequency range.<sup>237</sup>

## 5 Study of weak localization effects on brilliant whiteness generation

As discussed in the previous chapter, many disordered media can be characterized by effective quantities, while light transport within these media is treated as a diffusion process. Since the received macroscopic transport properties often describe the optical behavior of the medium correctly, this approach is usually preferred to the laborious solving of Maxwell's equations within the entire microscopic structure. However, diffusive light transport inherently neglects coherent effects that could play a crucial role in some cases.

Regarding the white scales of beetle *Cyphochilus*, previous studies have been concentrated on unveiling the correlation between structural and optical properties with a special emphasis on the influence of anisotropy, cf. Sec. 2.2.1 and references therein. In that, the framework of diffusion theory is regularly applied.<sup>21,22,26,28–30</sup> Although some studies using fully coherent FDTD simulations,<sup>24,25,27</sup> and even coherent backscattering is measured and reported for *Cyphochilus* scales,<sup>26</sup> so far, no work systematically investigated the influence of coherent effects on brilliant whiteness generation. On the contrary, the observed coherent backscattering cone is *a posteriori* reconstructed from the scattering angle distribution obtained by (incoherent) Monte Carlo simulations (see also Sec. 2.3), excluding all other coherent contributions.<sup>26</sup>

While scattering and whiteness optimization demands detailed knowledge about all relevant underlying effects, the unknown coherent contribution could inhibit tailoring nanostructure design for enhanced performance. For that reason, time-resolved spectromicroscopy measurements are performed for scattered light outside of the coherent backscattering cone to dissect different transport regimes in white beetle scales and fabricated DBS structures. This analysis is accompanied with incoherent Monte Carlo and fully coherent FDTD simulations to verify the experimental results and assess the contribution of diffusive light transport and coherent effects, which occur as scattering from weakly localized photonic modes.

The work presented below was done in cooperation with Ruben C. R. Pompe from Walter Pfeiffer's group at Bielefeld University, who has performed the spectromicroscopy measurement for each sample as well as collected and analyzed the experimental data. The main results presented here are also published in Ref.<sup>204</sup>

### 5.1 Fabrication of the DBS structure

Prior to conducting spectromicroscopy measurements, the DBS structure has to be experimentally realized and characterized. Deploying DLW, the structure is fabricated according to the model presented in Sec. 2.2.2, yielding a brilliant whiteness comparable to that of beetle *Cyphochilus* as displayed in Fig. 5.1a. To achieve me-

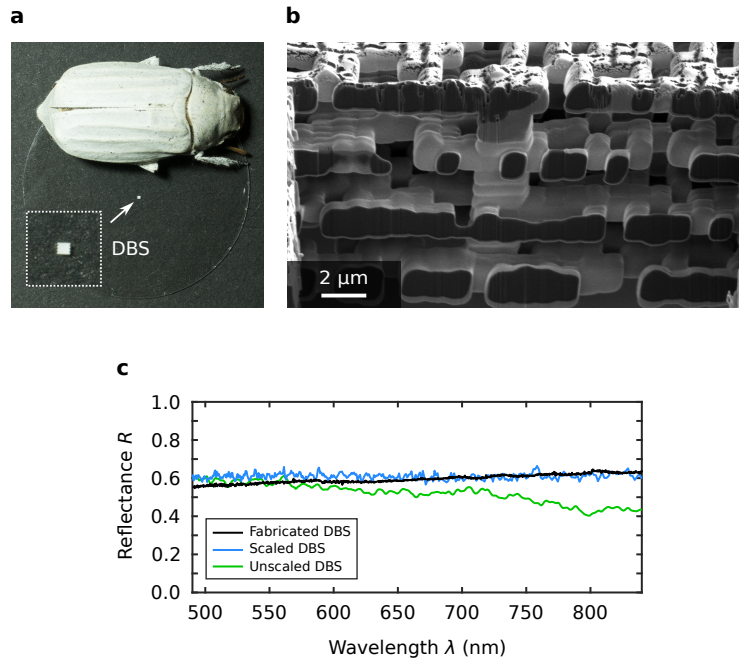


Figure 5.1: Comparison of the fabricated DBS structure with the white beetle and the computer model. **a**, Photograph of the white beetle *Cyphochilus* and the direct laser written DBS structure. The inset shows a magnified view of the DBS structure. **b**, SEM micrograph of a cross section through the printed structure shown in **(a)**, exhibiting its top four layers. **c**, Measured reflectance of the fabricated DBS structure in comparison to the simulated reflectance for the scaled and unscaled computer model. **(a)** is adapted from Ref. <sup>123</sup> and **(b)** is taken from Ref. <sup>204</sup>

chanical stability, the DBS version with constant center-to-center distance is used, while the structure must be scaled up compared to the original model to allow for printing. In addition, a scaffold is added to hold the separated layers in place.

In the fabrication step, first an open circular scaffold is printed possessing a diameter of  $64\ \mu\text{m}$ . Afterwards, the uppermost layer of the DBS structure is added on top of the scaffold with an overlap of  $7\ \mu\text{m}$  at the rim. From this layer four  $3.8\ \mu\text{m}$  long pillars with a footprint of  $2 \times 2\ \mu\text{m}^2$  are printed downwards to ensure constant spacing between consecutive layers. One of these pillars can be seen in the center of Fig. 5.1b. According to this procedure, the following layers and pillars are fabricated from top to bottom until the total number of nine layers is completed. In each layer, the different thickness of individual blocks is received by varying the laser power and thus the corresponding voxel size. The resulting building blocks possess a footprint of  $1 \times 1\ \mu\text{m}^2$ , while their thickness is found to mostly differ between  $1\text{--}2\ \mu\text{m}$ , as it can be discerned in Fig. 5.1b. To obtain an overall structure size of about  $0.5 \times 0.5\ \text{mm}^2$ , as shown in Fig. 5.1a, 46 separate DBS structures are placed on a hexagonal lattice.

To check the conformity of the fabricated with the theoretical DBS structure the reflectance is determined in both cases. To measure the reflectance of the printed structure, the sample is mounted at the output aperture of an integrating sphere, while it is illuminated by a white-light laser source (SuperK EVO equipped with



SuperK Varia, NKT Photonics A/S, Denmark) focused through the input aperture of the sphere onto the sample. The light collected by the sphere is analyzed using a spectrometer (USB2000+, Ocean Optics). The recorded spectrum is referenced on the spectrum of light reflected by a silver mirror placed at the output aperture under same illumination conditions.

As mentioned above, the fabricated architecture is scaled up, hence for a fair comparison a scaled-up version of the computer model should be used too. The corresponding block thickness is therefore chosen to follow a normal distribution with a mean value of  $1.5\ \mu\text{m}$  and a standard deviation of  $0.5\ \mu\text{m}$  within a range of  $1\text{--}2\ \mu\text{m}$ . The footprint ( $1 \times 1\ \mu\text{m}^2$ ) and the center-to-center distance of consecutive layers ( $3.8\ \mu\text{m}$ ) are equal to those of the fabricated structure.

It can be seen in Fig. 5.1c that the experimentally measured reflectance (black line) is in good accordance with the simulation results for the scaled DBS structure (blue line) showing an almost constant, high reflectance over the investigated spectral range. Nevertheless, there are some small deviations for short wavelengths, which are attributed to the fact that the scaled computer model is idealized, for instance, with respect to the shape of fundamental building blocks. Moreover, assuming a dispersion-free, i.e., constant, refractive index in simulations and neglecting any absorption is not satisfied for a real material like the used IP-L photoresist, especially for small wavelengths.<sup>238</sup>

Compared to the scaled model, the reflectance of the unscaled model generally decreases with increasing wavelength (Fig. 5.1c, green line), with noticeably lower reflectance in the near-infrared region beyond  $700\ \text{nm}$ . In the visible spectral range, however, the reflectance is at the same level or only slightly lower.

The deviation in the near-infrared range can be explained as follows. The unscaled DBS model shows a high reflectance due to the disorder-induced broadening of the second order stop band at  $475\ \text{nm}$  originating from the underlying Bragg stack structure (cf. Sec. 2.2.2). In contrast, the first order stop band at  $1426\ \text{nm}$  is only slightly affected by disorder limiting the range of high reflectance mainly to the visible. When the model is scaled up, the spectral positions of the stop bands are shifted accordingly. Thus, for the scaled model the seventh to twelfth order stop bands lie in the visible range, experiencing a similar broadening due to disorder as the second order stop band in the original model. Additionally, the fifth and sixth order stop band are in the range between  $700\ \text{nm}$  and  $850\ \text{nm}$ , hence extending the range of constant reflectance to this region. The underlying physics responsible for broad reflectance is, in consequence, not affected by the scaling, which allows to compare light transport mechanisms in the fabricated DBS structure with those found in beetle scales and the unscaled computer model.

## 5.2 Light scattering spectromicroscopy on brilliant white media

Multiple scattering occurring in random media is generally an elastic process.<sup>70,80</sup> As a result, interference effects are always existent, and every scattering event adds a well-defined phase to the scattered light which is stored in the time evolution of the corresponding electric fields. Thus, to analyze the influence of coherent transport on the brilliant whiteness of ultrathin scattering media, the time-resolved electric field of the scattered light must be evaluated. This is done by deploying the scattering light spectromicroscopy setup sketched in Fig. 5.2a to investigate a single beetle scale as well as the printed DBS structure, both displayed in 5.2b.

The detection of coherent effects is notably eased if only a small number of interfering paths is considered. For example, laser speckles are most prominent if the illuminated and detected area on the scattering medium is kept small, while in return they disappear if the detector integrates over a large area, i.e., many interfering paths. In such configurations, the light transport is still coherent but due to averaging most interference effects, except coherent backscattering, vanish and the resulting propagation can be well described by light diffusion theory. Therefore, to consider only a low number of interfering paths, the here shown investigation is based on focused excitation and detection of scattered light from a small sample volume.

To reach the spatial resolution required to detect only a small number of scattering paths, a femtosecond laser beam is focused onto the sample with a spot size of  $\lesssim 3\ \mu\text{m}$  using a parabolic mirror (see Fig. 5.2a and Sec. 3.2.2 for further details). In addition, the parabolic mirror collects the light scattered from the focal spot under an angle of  $\approx 24^\circ$  with respect to the specular direction. To examine internal scattering rather than surface scattering, a cross-polarization setup is applied. Mounting the respective sample on a piezo stage, the excitation spot can be scanned over the sample. The time-resolved electric field is obtained for every scan position by evaluating the spectral interference between the scattered and the reference pulse as described in Sec. 3.2.2.

The resulting amplitude of the electric field is shown in Fig. 5.2c for the investigated beetle scale. The temporal evolution of the electric field exhibits a spatially varying exponential decay which is superimposed by pronounced beatings, a typical fingerprint of interference effects. As revealed below, the light transport can be dissected in two different regimes. Initially, a diffusion-like transport regime prevails (illustrated in Fig. 5.2d). At a later stage, leakage from weakly localized photonic modes arising from randomly closed scattering paths (Fig. 5.2e) contributes considerably to the scattered light, leading to the observed beating behavior.

While different transport regimes can be distinguished due to their characteristics in the frequency domain, a temporal dissection requires an analysis in the time domain. For that reason, the coherent scattering signal (Fig. 5.2f) is investigated with the aid

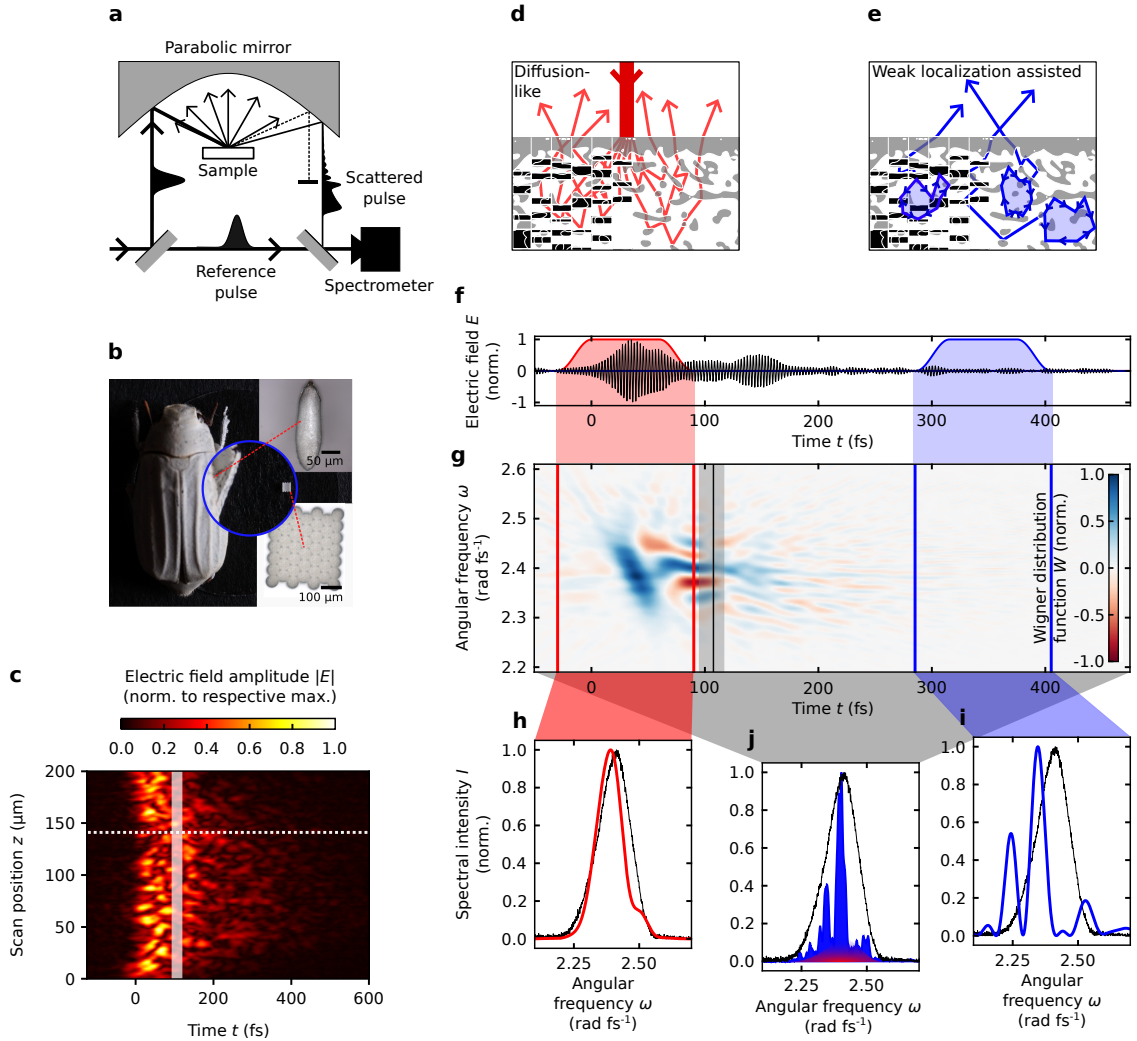


Figure 5.2: Time-resolved spectromicroscopy of light scattered from a *Cyphochilus* scale. **a**, Sketch of the deployed experimental setup. **b**, Microscopy image of a single beetle scale (upper right) and printed DBS structure (lower right) obtained from the respective objects shown in the photograph. **c**, Time-resolved amplitude of the light scattered from the beetle scale at different scan positions. The threshold between the diffusive and the weak localization assisted scattering regime, as identified in the Wigner representation (**g**), is marked by the gray bar. **d,e**, Illustration of light transport in the diffusive (**d**) and the weak localization assisted scattering regime (**e**). The gray and black patterns display the intra-scale and the DBS structure, respectively. **f**, Electric field of the scattered light obtained for the scan position indicated in (**c**) by the white, dashed line. **g**, Wigner representation of the electric field shown in (**f**). The gray bar denotes the found threshold between distinct transport regimes, while the black line marks the calculated pulse round trip time. **h–j**, Computed Fourier spectra for the red (**h**) and blue (**i**) short time windows exhibited in (**f**) and (**g**) and for the entire time signal (**j**). Moreover, the excitation spectrum (black line) is depicted in each panel. Adapted from Ref. <sup>204</sup>

of the Wigner distribution function, which enables a simultaneous representation of the frequency and time domain. The Wigner distribution function is basically the

Fourier transform of the autocorrelated signal and hence given by

$$W(t, \omega) = \int_{-\infty}^{\infty} E\left(t - \frac{t'}{2}\right) E^*\left(t + \frac{t'}{2}\right) e^{-i\omega t'} dt', \quad (5.1)$$

with  $E$  and  $E^*$  being the electric field and its complex conjugate, respectively.<sup>239</sup> While the Wigner distribution function features the highest possible time–frequency resolution, it has the disadvantage of not being a linear transformation, resulting in cross-terms with no actual physical meaning.<sup>239</sup> Therefore, the analysis must be accompanied by calculating the spectral power of the short-time Fourier transform, that is the Fourier transform of the signal within a specific time window.

For that purpose, a Tukey window with a width of  $\Delta t = 120$  fs and a rising time of  $t_r = 30$  fs is applied. A Tukey window is obtained as the convolution of a cosine lobe with a rectangular window.<sup>240</sup> As a result, it has smoother slopes than a rectangular window which reduces spectral leakage, i.e., the introduction of spectral components that are not present in the original signal but are introduced as a result of multiplying the time signal by a finite window.<sup>240</sup>

The resulting Wigner distribution function (Fig. 5.2g) exhibits for early times broadband features, as expected for diffusion-like transport, which is largely wavelength independent. Indeed, computing the short-time Fourier transform for the regime indicated by the red window, the spectrum of the scattered light reproduces the excitation spectrum in good agreement, as revealed in Fig. 5.2h. However, around  $105 \pm 10$  fs (gray bar in Fig. 5.2g), a qualitative change in the Wigner spectrum is observed, as the broadband features are substituted by sharp modulations. These spectral modulations arise from resonance peaks, which are also found in the according short-time Fourier transform spectrum (Fig. 5.2i) independent of the excitation spectrum. As shown in Fig. 5.2j, the Fourier spectrum obtained for the entire time signal exhibits a broadband background superimposed by sharp spectral peaks, featuring the attributes of both transport regimes.

The found threshold time at which the spectral characteristic changes coincides closely with the pulse round trip time  $t_{\text{prt, scale}}$  (Fig. 5.2g, black line). The pulse round trip time is the duration that a light pulse takes to propagate back and forth through the scale under the assumption of an effective medium, as it is usually done in the diffusion approximation. It is calculated as the sum of the effective round trip time obtained for a single photon and the pulse length to ensure that ‘all’ photons within the pulse have hit the top of the scale again. The effective round trip time is given by  $t_{\text{eff, scale}} = 2l_{\text{scale}}n_{\text{eff}}/c_0$ , with  $l_{\text{scale}} = 10 \mu\text{m}$  being the thickness of the beetle scale.<sup>27</sup> Since the diameter of the fibrils in the intra-scale network follows a normal distribution with a mean value of  $230 \text{ nm}$ ,<sup>24</sup> the effective refractive index can be calculated with the mixing rule for large particles presented in Ch. 4 according to the procedure used for the DBS structure in Sec. 4.4. For a filling fraction of  $f_{\text{scale}} = 31\%$ <sup>27</sup> and a refractive index of  $n_{\text{chitin}} = 1.55$ ,<sup>96</sup> a value of  $n_{\text{eff, scale}} = 1.17$  is obtained, which results in an effective round trip time of  $t_{\text{eff, scale}} = 78$  fs. With a

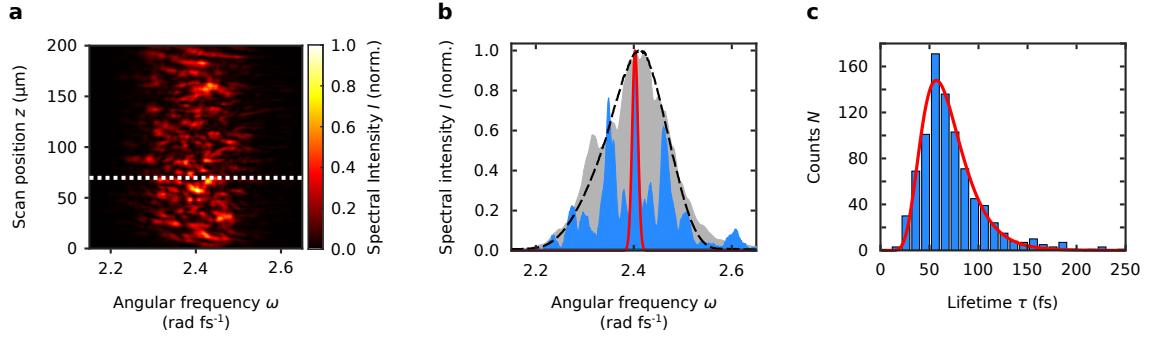


Figure 5.3: Lifetime distribution measured for a *Cyphochilus* scale. **a**, Spectra of the light scattered from the beetle scale at different scan positions. **b**, Spectral intensity (blue) obtained for the scan position marked by the white line in **(a)**. The gray area shows the incoherent, normalized sum of all spectra of the scan and the black, dashed line the corresponding excitation spectrum. As depicted by the red curve, individual peaks are identified, and the peak width is determined to extract the associated lifetime. **c**, Distribution of the photonic mode lifetimes, received for the scan shown in **(a)**. The distribution is closely fitted by a log-normal distribution (red line). Adapted from Ref.<sup>204</sup>

pulse length of 29 fs (measured from the pulse front to the drop of the amplitude to  $1/e$  of the peak value) a pulse round trip time of  $t_{\text{prt, scale}} = 107$  fs is received.

While applying the short-time Fourier transform enables to temporally dissect different transport regimes based on their spectral signature, the resolution of the resonance peaks suffers from the short time windows. To unequivocally clarify the existence of weak localization assisted scattering, full-time Fourier transform is used to retrieve the probability distribution of the resonance lifetimes. As it can be seen in Fig. 5.3a for all scan positions, multiple peaks which differ in center frequency and width can be found in the respective spectrum. Due to the averaging of spectral peaks, the incoherent sum of all spectra of the scan (Fig. 5.3b, gray area) corresponds to the excitation spectrum (black, dashed line) which macroscopically leads to the white appearance.

Identifying the peaks using a Matlab routine, as illustrated in Fig. 5.3b by the red curve, the spectral width can be obtained, which provides a lower limit to the resonance lifetime. Figure 5.3c shows the resulting distribution of lifetimes obeying a log-normal distribution (red line) as expected in the case where localization effects are present.<sup>241</sup> The log-normal distribution deviates from the normal distribution in that it features a larger fraction of long lifetimes associated with the existence of localized modes in which light dwells comparatively long in closed scattering paths before coupling into loss channels.<sup>242</sup>

As mentioned above, the fabricated DBS structure is investigated and analyzed according to the procedure described for the beetle scales. The measurement results in time domain (Fig. 5.4a) and frequency domain (Fig. 5.4b,c) as well as the corresponding analyses by means of Wigner distribution function and short-time Fourier transform (Fig. 5.4d-h) qualitatively agree with those of the beetle scales. However,

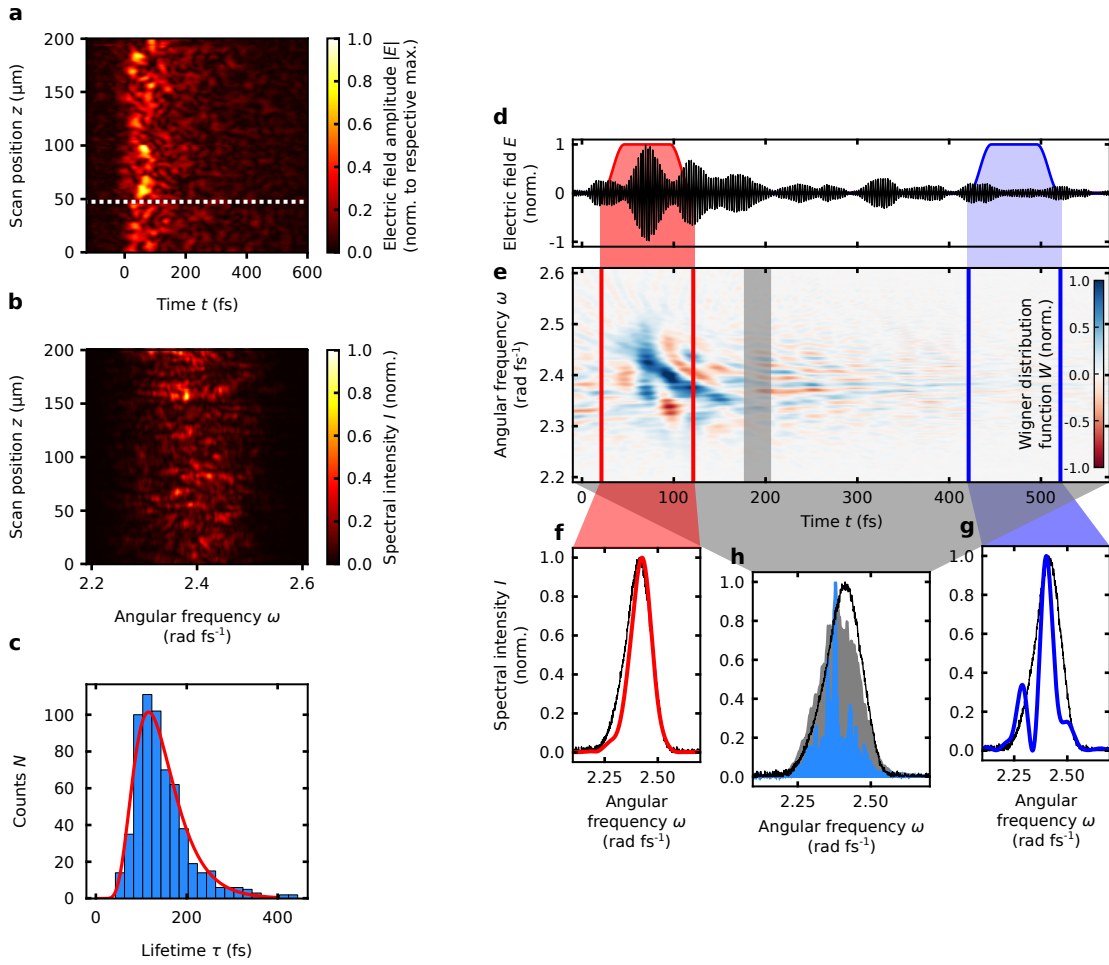


Figure 5.4: Time-resolved spectromicroscopy of light scattered from the fabricated DBS structure. **a**, Time-resolved amplitude of the light scattered from the DBS architecture at various scan positions. **b**, Corresponding spectra in dependence of the scan position. **c**, Lifetime distribution received for the scan exhibited in **(b)**. **d**, Electric field of the scattered light for the scan position marked in **(a)** by the white, dashed line. **e**, Wigner representation of the electric field shown in **(d)**. The gray bar indicates the identified threshold between different transport regimes. **f-h**, Calculated Fourier spectra for the red **(f)** and blue **(g)** short time windows shown in **(d)** and **(e)** as well as for the complete time signal **(h)**. In addition, the incoherent, normalized sum of all spectra of the scan (gray area) is displayed in **(h)** and the excitation spectrum (black line) is shown in each panel. Adapted from Ref. <sup>204</sup>

due to larger structure thickness, about  $30\ \mu\text{m}$  for the DBS structure compared to  $10\ \mu\text{m}$  for the scales, the time scale is shifted. In consequence, the threshold at which broad features transform to fine modulations in the Wigner representation is identified around  $190 \pm 10\ \text{fs}$ , at a significantly later time than in the beetle scales.

The computation of a corresponding pulse round trip time is a delicate matter in the case of the DBS structure. The individual blocks of the printed DBS architecture reach thicknesses of up to  $2\ \mu\text{m}$ , considerably larger than the laser wavelength of  $780\ \text{nm}$ . For this reason, the structure is far beyond the validity range of the mixing

rule developed in Ch. 4, which thus prevents its use for calculation. Moreover, according to the analysis of random sphere packings with sphere sizes beyond this validity range in Sec. 4.3, the treatment of the printed DBS structure as an effective medium is generally invalid.

Nevertheless, the brilliant whiteness generation in the heterogeneous DBS structure relies on multiple scattering, i.e., the scattered light passes different compounds of the structure several times. As a result, the optical length of an average scattering path will still depend on a mixture of both refractive indices.

For an approximate estimation of the pulse round trip time, the average refractive index is assumed to be given by the sum of the refractive indices of air and photoresist ( $n_{\text{IP-L}} = 1.51$ )<sup>238</sup> weighted by their respective volume fractions (the filling fraction of the structure is 33%). Thus, an average refractive index of  $n_{\text{avg, DBS}} = 1.17$  is received, yielding a pulse round trip time of around 260 fs.

While this time does not match the found threshold, it is at least in the same order. It is therefore assumed that the deviation is mainly due to the rough estimation of the average refractive index, which is made because the dimension of the printed DBS structure inhibits the application of any mixing rules. In contrast, in the case of beetle scales, which comply with the description as an effective medium, the mixing rule presented in Ch. 4 provides an adequate result for the pulse round trip time.

### 5.3 Numerical investigation of different transport regimes

In contrast to experiments, where interference is always existent due to elastic light scattering, altering the simulation approach used allows to systematically enable and disable interference effects and thus to unambiguously verify the experimental result presented in the last section. In fact, the results of fully coherent FDTD simulations can be directly related to those of incoherent Monte Carlo simulations. Using simulations, it is moreover possible to assess the intrinsic light transport directly while the experimental evaluation completely relies on scattered light.

FDTD simulations, however, can only handle relatively small sample volumes, so periodic boundary conditions must be used. To study spatial characteristics of closed scattering loops, sufficiently large lateral simulation dimensions of  $20 \times 20 \mu\text{m}^2$  have to be applied to avoid parasitic effects from the artificial periodicity. At this extent, closed loops fit entirely in a single period, even at the upper edge of the log-normal distribution (around 150 fs, cf. Fig. 5.3c), where the corresponding path length is about  $40 \mu\text{m}$ , i.e.,  $20 \mu\text{m}$  in one direction. Since meshing of a complex structure such as the intra-scale network is computationally extremely demanding in such large-scale simulations, deploying the simple DBS model is favored to keep the computation time acceptable.

While experimentally the DBS structure and the *Cyphochilus* scales reveal qualitatively the same transport behavior, the validity to directly infer from the unscaled

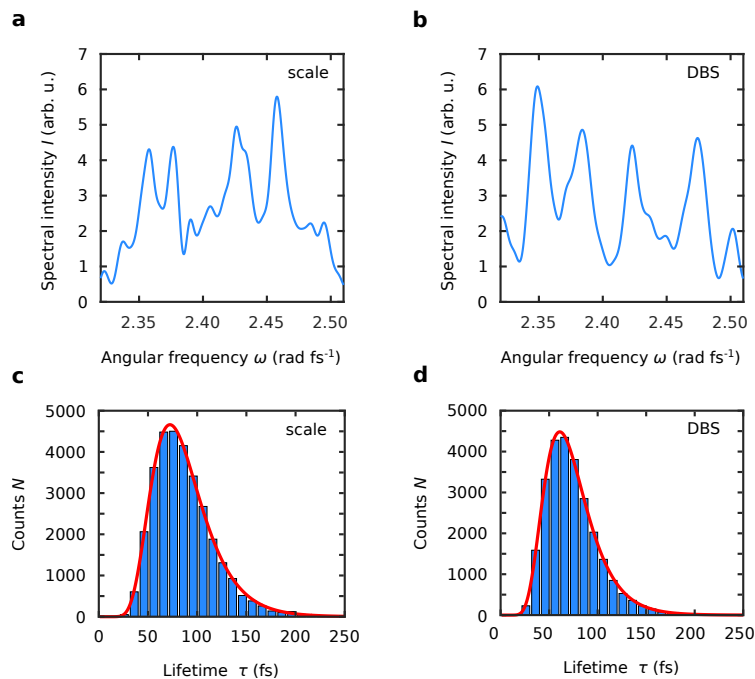


Figure 5.5: Resonance peaks and corresponding lifetime distribution of simulated model structures. **a,b**, Exemplary spectrum gathered in FDTD simulations with a point monitor placed in the intra-scale network (**a**) and the DBS model (**b**), respectively. **c,d**, Corresponding lifetime distribution received for the intra-scale network (**c**) and the DBS model (**d**) by evaluating the spectra of all used point monitors. Adapted from Ref.<sup>204</sup>

DBS model to the intra-scale structure<sup>a</sup> must be first confirmed performing FDTD simulations (with a lateral dimension of  $7 \times 7 \mu\text{m}^2$ ). Local spectra recorded inside both structures indeed feature distinct resonance peaks in a similar way, as exemplarily shown in Fig. 5.5a and b, respectively. Using all recorded spectra (see Sec. 3.1.1 for details), the computed lifetime distributions are in excellent agreement with each other (Fig. 5.5c and d) as well as with the experimentally obtained distribution for the beetle scales (Fig. 5.3c). Therefore, it can be concluded that (i) the properties retrieved from scattered light indeed reflect the intrinsic behavior and (ii) the DBS model can be used for further investigations applying large-scale simulations.

In these simulations, the spatio-temporal evolution of the local power is gathered in a monitor plane sectioning the DBS model vertical to its surface. In addition, the results are compared to the associated spatio-temporal evolution of the photon number in similar Monte Carlo simulations. However, to set up appropriate Monte Carlo simulations, first the correct transport and scattering mean free path must be determined. To obtain the transport mean free path, the transmittance of the DBS model as a function of the structure height  $L$  is computed applying FDTD simulations and subsequently fitted with Eq. (2.19) as shown in Fig. 5.6a. The fit

<sup>a</sup>model data supplied by courtesy of B. Wilts<sup>24</sup>



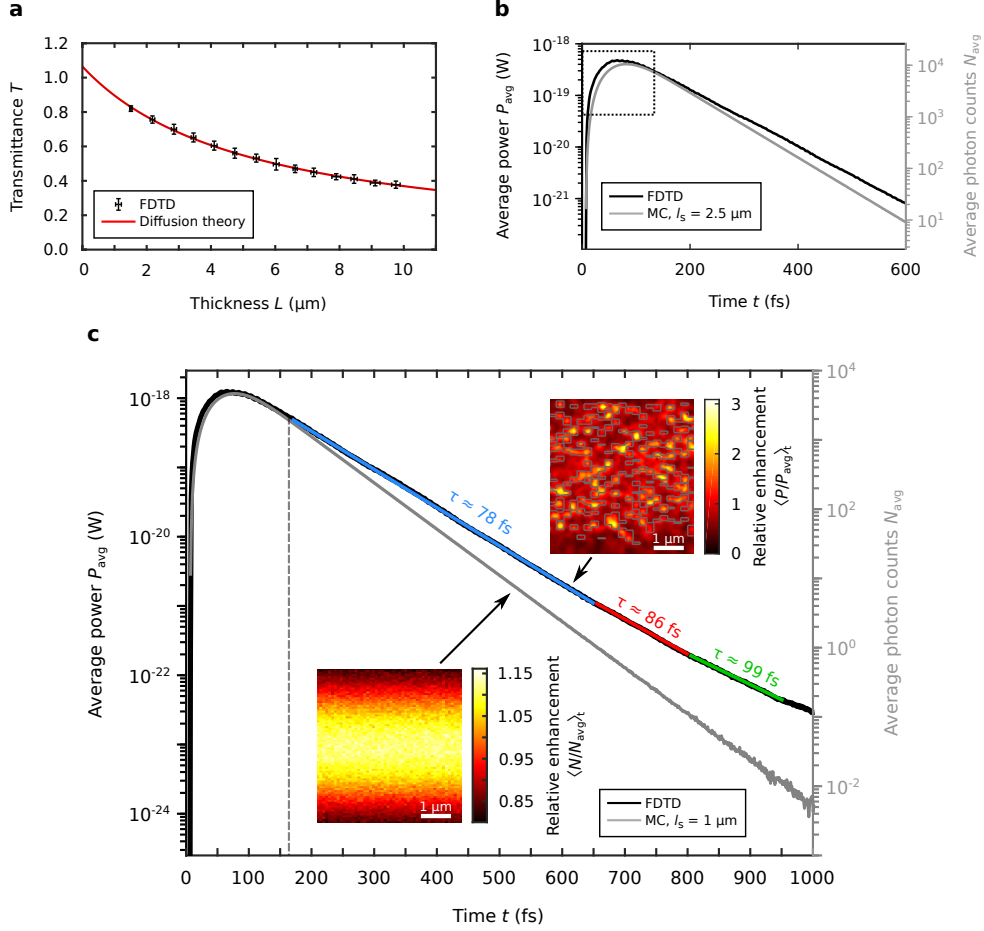


Figure 5.6: Spatio-temporal evolution of coherent and diffusive light transport. **a**, Transmittance of the DBS model as a function of the structure thickness obtained through FDTD simulations. The results are fitted with the isotropic diffusion equation (red line). **b**, Comparison of the average power (black line) and the average photon count (gray line) in the monitor plane for a scattering mean free path of  $2.5 \mu\text{m}$  in Monte Carlo (MC) simulations. The black dotted box indicates the area where the top of both curves deviates. **c**, Same as (b) but applying a scattering mean free path of  $1 \mu\text{m}$  in Monte Carlo simulations. Both ordinates span the same order of magnitudes, allowing for direct comparison of the slopes. The colored exponential slopes with various lifetimes  $\tau$  highlight the non-exponential decay of the FDTD results. The vertical gray, dashed line corresponds to the calculated round trip time. Insets: Local power enhancement (upper right, FDTD) and local photon count enhancement (lower left, Monte Carlo) averaged over the time span marked by the blue line ( $170$ – $650$  fs) shown for a snippet of the entire monitor plane. Adapted from Ref. <sup>204</sup>

yields a value of  $l_t = 3.0 \mu\text{m}$  at  $780 \text{ nm}$  in accordance with previous investigations.<sup>95</sup> Using this value in Monte Carlo simulations together with  $n_{\text{eff, DBS}} = 1.15$  (calculated with the mixing rule for large particles for  $f_{\text{DBS}} = 27\%$  and  $n_i = n_{\text{chitin}}$ ), the received reflectance matches that obtained by FDTD simulations.

Unlike the transport mean free path, the scattering mean free path does not affect the transmittance and hence reflectance directly, as it can be discerned in Eq. (2.19) in conjunction with Eq. (2.18). Therefore, the scattering mean free path is determined

by comparing the temporal profile of the average power in the monitor plane (FDTD simulations, black line in Fig. 5.6b and c) with the time evolution of the average photon count (Monte Carlo simulations, gray line in Fig. 5.6b and c) for different scattering mean free paths. As it can be seen in Fig. 5.6b for  $l_s = 2.5 \mu\text{m}$ , the top of both curves diverges (black, dotted box) whereas they align for a scattering mean free path of  $l_s = 1.0 \mu\text{m}$  (Fig. 5.6c).

In consequence, there is a set of parameters at which Monte Carlo simulations replicate all transport properties obtained by fully coherent FDTD simulation, namely, reflectance, transport mean free path and initial temporal evolution of the power within the structure. Thus, the initial light transport can be modeled as a diffusive process in close approximation even if interference effects might be existent.

However, from  $\approx 170$  fs a discrepancy between the FDTD and Monte Carlo results starts to appear (Fig. 5.6c), indicating that the description as light diffusion breaks down. In this regime, a multi-exponential decay is found for FDTD simulations, with decay times ranging from roughly 80 fs to about 100 fs. This straightly relates to the lifetime distribution (Fig. 5.5d) with a mean value around 80 fs, implicating that random photonic modes with long lifetimes dominate the decay at later times. Contrarily, Monte Carlo simulations reveal a mono-exponential decay with a decay constant of 65 fs, which neither correspond to the simulated nor to the measured lifetime distribution. Hence, only a fully coherent description suffices to model this regime where weakly localized photonic modes characterize the transport behavior.

Computing the pulse round trip time in analogous to the experiment yields a value of 162 fs for the 100 fs long pulses used in the simulation. As shown by the gray, dashed line in Fig. 5.6c, this time closely matches the point where both simulation approaches starts to deviate. This implies that the pulse round trip time is an appropriate assessment for the upper limit of the diffusive transport regime.

To further verify that indeed weakly localized modes are present in the regime beyond 170 fs, the time averaged local power enhancement is calculated. In the first step, the momentary power enhancement:

$$P_{\bar{\rho}}(x, z, t) = \frac{P(x, z, t)}{\bar{\rho}(t)}, \quad (5.2)$$

with the mean power in the  $x$ - $z$ -monitor plane:

$$\bar{\rho}(t) = \int_A \frac{P(x, z, t)}{A} dA, \quad (5.3)$$

is computed to compensate for radiation losses to the far field (for orientation of the DBS model see Fig. 2.6e). Eventually, the time averaged local power enhancement for the interval  $[t_1, t_2]$  is received via

$$\langle P/P_{\text{avg}} \rangle_t = \langle P_{\bar{\rho}} \rangle_t = \int_{t_1}^{t_2} \frac{P_{\bar{\rho}}(x, z, t)}{(t_2 - t_1)} dt. \quad (5.4)$$

The upper right inset in Fig. 5.6c shows the local power enhancement averaged over the time marked by the blue line (170–650 fs) applying FDTD simulations. Here, distinct spatially localized hotspots can be discerned, which possess a power enhancement up to a factor of three. Since this enhancement persists even when averaged over almost 500 fs, it is concluded that the hotspots are stationary. They can thus be associated with antinodes of weakly localized long-lasting random modes, leading to the sharp resonance peaks observed in experiments and simulations. Indeed, performing a similar analysis for Monte Carlo outcomes, the time averaged local photon number enhancement does not show any hotspots at all, as revealed in Fig. 5.6c, lower left inset. Instead, a constant photon number is found in the lateral direction, while the slight variation in the axial direction can be attributed to the fact that light escapes at the boundaries of the slab.

## 5.4 Contribution of distinct transport regimes to the whiteness

Based on the experimental and simulation outcomes, the contribution of the diffusive and the weak localization enhanced scattering regime on the reflectance and hence the whiteness can be assessed. To evaluate each portion the accumulated scattering yield  $\Sigma$  is determined for every structure by integrating the incoherent intensity signal over time. The incoherent intensity is thereby received through averaging the square modulus of the time-resolved scattered field over all recorded positions. To

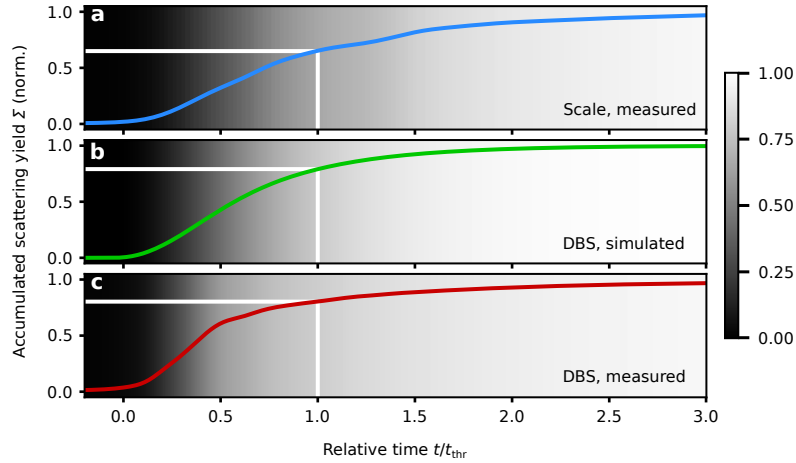


Figure 5.7: Time-resolved accumulated scattering yield and related color impression. **a**, The measurements performed at the beetle scales reveal a scattering yield from the weak localization enhanced scattering regime, i.e., after the threshold time, of 35% (white horizontal line). **b**, The corresponding results for the simulated DBS structure reveal a scattering yield of 21% from this regime. **c**, The measurement outcome for the fabricated DBS structure show an scattering yield of 20% from weak localization. The background shading displays for each sample the resulting color impression from black to white in dependence of the accumulated scattering yield at each point in time. Adapted from Ref. <sup>204</sup>

compare the various results in the same manner, each time scale is normalized to the respective threshold time, which divides both transport regimes.

As revealed in Fig. 5.7, a significant portion of 20% to 35% of the reflected light originates from the weak localization assisted scattering regime. As a result, the brilliant white media would appear rather gray than white if this regime was absent, as illustrated by the background shading in Fig. 5.7.

Hence, photon leakage from weakly localized photonic modes is a crucial mechanism for the generation of brilliant whiteness in ultrathin scattering media. Although such modes have been identified beforehand in random laser materials with coherent feedback,<sup>80,243</sup> their important role in whiteness generation was not considered yet.

While the structures examined here show clear characteristics of individually localized modes, the reported results do not reveal the onset of strong localization. Anderson localization would require the complete halt of light transport even for finite sample size,<sup>39</sup> which is obviously not the case for the investigated structures. In addition, none of the structures satisfies the Ioffe-Regel criterion (cf. Sec. 2.3.3). Nevertheless, the investigated structures clearly demonstrate that localization effects can significantly affect light transport even outside of the regime of strong localization.

## 6 Developing of bio-based resists and establishing the sensitization effect for DLW

While nature provides a large pool of design concepts to tailor various properties, for example optical properties as shown in the previous chapter, it also offers a great variety of corresponding building materials.<sup>2</sup> Such materials are also of technological interest, in particular for microfabrication, since they enable reproducing natural structures in facsimile for testing, analyzing, and biomimetic engineering. In addition, devices for biomedical applications, especially *in vivo*, require biocompatibility, which is inherently given for a wide range of natural materials.<sup>244,245</sup>

Indeed, animal-based biomaterials used for DLW are commonly hydrogel formulations, i.e., soft materials,<sup>54–58</sup> which allow for imitating the extracellular matrix as needed in tissue engineering or drug delivery applications.<sup>246,247</sup> Many architectures in nature, however, make use of rigid materials, e.g., cellulose in wood cells or chitin in arthropods' cuticle and scales, offering a whole new level for designing bionic structures. While plant-based carbohydrates, such as cellulose, are already available for printing rigid structures via DLW,<sup>9</sup> their animal-based counterparts are currently lacking.

To close this gap, first a derivative of the monomeric unit of chitin, namely N-acetyl-D-glucosamine (NAG), is functionalized with methacrylic side groups. Subsequently, this methacrylated NAG serves as the basis for non-hydrogel photoresist formulations that establish a new class of animal-sourced photoresists for DLW. In addition, the resists presented in this chapter rely on a low molecular compound, i.e., a monomer, in contrast to bio-based photoresists reported so far, which use polymers as basic unit.<sup>9,55,58</sup>

Beside developing NAG-based photoresists, a new crosslinking strategy is established by adapting the UV sensitization effect for two-photon polymerization. In this, a sensitizer–photoinitiator pair is used instead of a single photoinitiator. The sensitizer absorbs light via two-photon absorption and subsequently transfers the acquired energy to the photoinitiator, which cleaves in highly reactive radicals and starts the polymerization. Unlike a single photoinitiator, the system allows separate optimization of the absorption efficiency and the crosslinking capability by selecting an appropriate sensitizer–photoinitiator pair, which outperforms the use of a photoinitiator or sensitizer alone.

The work shown in this chapter was done in cooperation with Maximilian Rothammer and Maximilian Maier from Cordt Zollfrank's group at the Technischen Universität München, who performed the synthesis, functionalization, and chemical characterization of the NAG derivatives used to mix the photoresists. The key findings reported in this chapter are also published in Ref.<sup>248</sup>

## 6.1 Chemical functionalization of N-acetyl-D-glucosamine

While plain NAG is not photo-crosslinkable, unsaturated side groups must be added to the monosaccharide, which is done by applying methacrylic acid anhydride in a N,N-dicyclohexylcarbodiimide-coupled esterification as described below. First, under continuous stirring and reflux conditions, 3.05 g NAG are dissolved in 100 mL DMF at 58 °C. Once the solution is cooled down to room temperature, 5.8 mL methacrylic acid anhydride (94%, Sigma Aldrich), 0.1 g 4-dimethylaminopyridine (DMAP, 99%, Acros Organics) and 4.04 g N,N-dicyclohexylcarbodiimide (DCC, 99%, Alfa Aesar) are admixed. After constantly stirring the reaction mixture for 45 h, it is concentrated using a rotary evaporator. The methacrylated NAG is eventually obtained through precipitation in an excess of diethyl ether (technical grade, VWR International) placed within an ice bath. However, before the methacrylated NAG is used to mix a photoresist, it is washed five times with diethyl ether and once with ethanol deploying a centrifuge for 20 min (at 4000 rpm and 20 °C), while the solvents are subsequently allowed to evaporate using a rotary evaporator.

To proof whether the esterification is successful, Fourier transform infrared (FTIR) and nuclear magnetic resonance (NMR) spectroscopy are used to investigate and compare the compounds. Since FTIR spectra reveal absorption bands caused by vibronic transitions characteristic of a specific chemical bond, they enable detection of the appearance and disappearance of bonds associated with esterification and crosslinking. The corresponding measurements are performed using a Frontier MIR spectrometer (L1280018) equipped with an attenuated total reflection diamond (PerkinElmer, Inc., USA) providing a resolution of 4 cm<sup>-1</sup>. For each spectrum at least eight scans are recorded. To study crosslinked methacrylated NAG, a photoresist composed of 50 mg methacrylated NAG, 250 µL DMSO, and 1 mg Irgacure 369 is polymerized for 30 min under an 8 W UV lamp (Herolab GmbH, Germany) using the 245 nm and 365 nm output concurrently.

Figure 6.1a shows the FTIR analyses for NAG, methacrylated NAG, and polymerized methacrylated NAG confirming the proper esterification of NAG as well as crosslinking via the added methacrylic side groups. The observed absorption bands at 1624 and 1546 cm<sup>-1</sup> refer to amide I and amide II modes, respectively, which are assigned to the amide carbonyl group in secondary amides.<sup>249-254</sup> C=O stretching vibrations are primarily responsible for the amide I band, while small contributions originate from N-H bending as well as N-H and C-H stretching vibrations of the amide.<sup>255,256</sup> The amide II band is characterized by N-H bending and the presence of certain C-H stretching vibrations.<sup>255-257</sup> Absorption bands at 3453 cm<sup>-1</sup> and 3322 cm<sup>-1</sup> are related to O-H and N-H stretching vibrations, while C-O-C antisymmetric bridge oxygen stretching vibrations, C-O stretching vibrations, antisymmetric in-phase ring vibrations, as well as C-O-H stretching vibrations give rise to the features at 1125, 1049 and 1018 cm<sup>-1</sup>, respectively.<sup>251-253,257,258</sup>

## 6.1 Chemical functionalization of N-acetyl-D-glucosamine

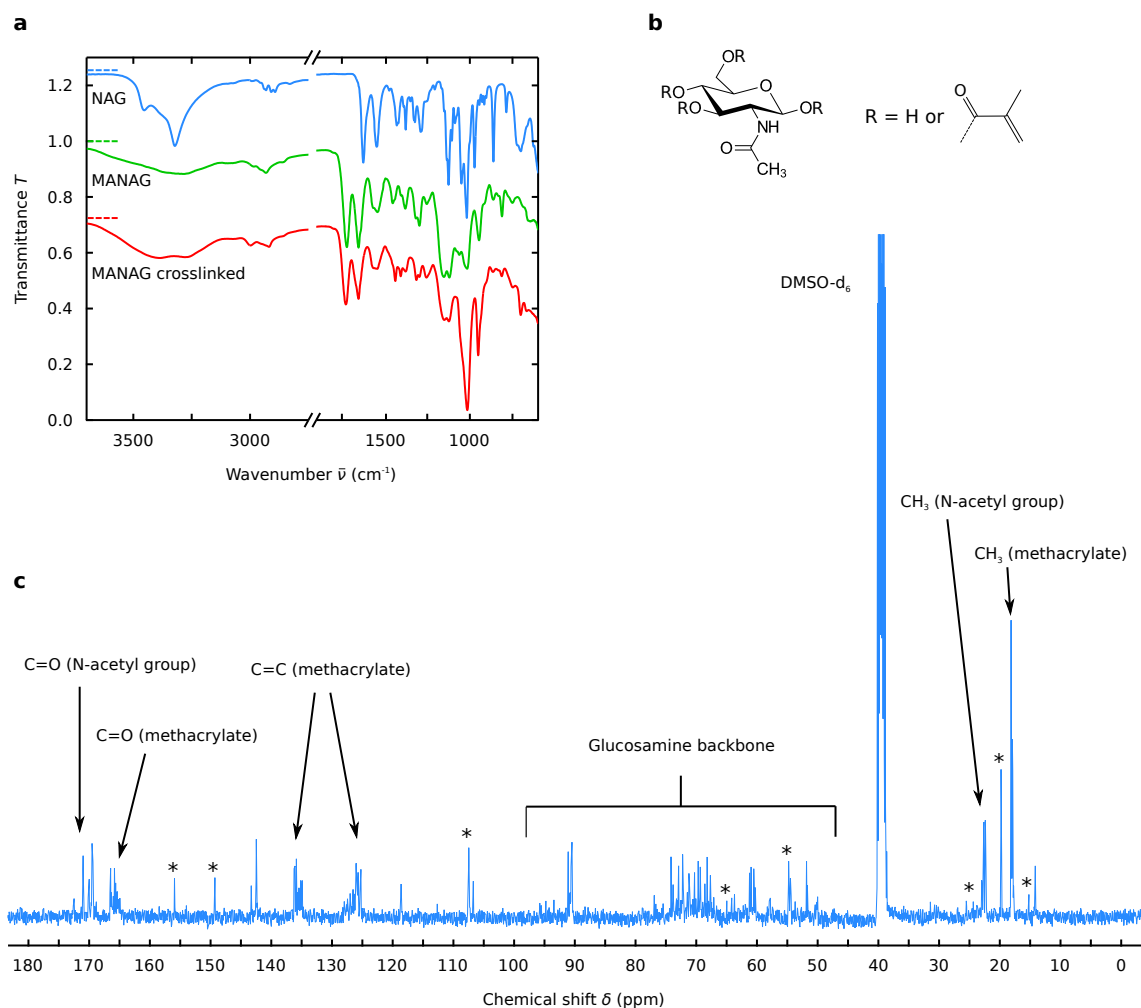


Figure 6.1: Chemical characterization of NAG derivatives. **a**, FTIR spectra of NAG (blue line), methacrylated NAG (MANAG, green line), and crosslinked methacrylated NAG (red line). For better visibility the spectra of NAG and crosslinked methacrylated NAG are vertically shifted. The dashed colored lines indicate the corresponding transmittance of 100% for each graph. **b**, Structural formula of NAG ( $R = \text{hydrogen}$  at all sites) and methacrylated NAG ( $R = \text{methacrylate}$  group at least at one site). **c**,  $^{13}\text{C}$ -NMR spectrum of methacrylated NAG with attribution of the observed peaks to the appropriate groups. The asterisks denote peaks which are identified as impurities of *N,N*-dicyclohexylcarbodiimide (DCC) (55.8, 25.6, 24.7 ppm), 4-dimethylaminopyridine (DMAP) (155.9, 149.3, 107.5 ppm), diethyl ether (66.1, 15.1 ppm), and ethanol (56.1, 18.5 ppm) using an online database such as NMRShiftDB.<sup>259</sup> Adapted from Ref. <sup>248</sup>

After the methacrylation process, novel bands occur at  $1721$  and  $812\text{ cm}^{-1}$  (Fig. 6.1a, green line). The former is related to the carbonyl  $\text{C}=\text{O}$  stretching vibrations of the ester,<sup>249,252,255,260</sup> while the latter arises from  $\text{C}=\text{CH}_2$  out of plane deformation vibration of the carbon double bonds in the methacrylate group,<sup>9,260</sup> proving the successful functionalization of NAG. In addition, the absorption band at  $3453\text{ cm}^{-1}$  belonging to hydroxyl groups is diminished after esterification. This meets the expectation, since hydrogen is substituted by methacrylate groups in one or multiple

Table 6.1: Signal attribution for the  $^{13}\text{C}$  NMR spectra measured for NAG and methacrylated NAG (MANAG). Adapted from Ref. <sup>248</sup>

Sample	Assignment of chemical shift $\delta$ (ppm)						
	C=O	C=O	C=C	C=C	C1-C6	CH <sub>3</sub>	CH <sub>3</sub>
	(NAG)	(MANAG)				(NAG)	(MANAG)
NAG	170.0	-	-	-	91.1-54.8	23.2	-
MANAG	169.8	166.9	136.3	126.3	91.6-54.8	23.2	18.6

OH-groups, depending on the degree of substitution. The corresponding molecules are depicted in Fig. 6.1b.

During polymerization via methacrylic side groups, the corresponding carbon double bond is cleaved. Indeed, the dip associated with this double bond ( $812\text{ cm}^{-1}$ ) is absent in the spectrum of crosslinked methacrylated NAG (Fig. 6.1a, red line), implying that the photo-crosslinking takes place via the methacrylic side groups.

To further verify the esterification,  $^{13}\text{C}$  NMR spectroscopy is applied, which enables identification of carbon in different chemical bonds by the shift of the magnetic resonance as a function of the chemical environment. The measurements are conducted using a ECS-400 NMR (JEOL Ltd., Japan), while the data acquisition and evaluation is done with the software Delta v 5.0.4 (JEOL) and MestReNova v 14.2.3 (Mestrelab Research S.L., Spain). Spectra are obtained for the compounds dissolved in DMSO- $d_6$  at  $25^\circ\text{C}$  as the result of 2048 scans.

Figure 6.1c displays the  $^{13}\text{C}$  NMR spectrum obtained for methacrylated NAG, while Tab. 6.1 summarizes the characteristic shifts received for NAG and methacrylated NAG. Signals at 170.0, 91.1-54.8, and 23.2 ppm are found for both compounds, since the signals between 91.1-54.8 ppm correspond to the C1-C6 atoms of the glucose backbone of the monosaccharide, while the signals at 170.0 and 23.2 ppm can be attributed to the ester and the methyl group of the N-acetate moiety, respectively.<sup>261</sup> In contrast to NAG, methacrylated NAG features peaks around 166.9, 136.3, and 126.3 ppm (Fig. 6.1c), which are associated with the C=O and C=C bond in the methacrylate, exhibiting the successful esterification of NAG.<sup>9,261</sup> In addition, the peaks related to the CH<sub>3</sub> group of the methacrylic side group are observed around 18.6 ppm.<sup>260</sup>

As revealed by the splitting of the corresponding signals, esterification takes place at several positions of the NAG backbone. However, due to overlapping and the overall complex signal structure, an unequivocally evaluation of the exact positions is not possible. Moreover, as revealed in Fig. 6.1c by the peaks marked with an asterisk, some impurities caused by the deployed coupling agents exist. Therefore, the degree of methacrylation cannot be precisely assessed.



Element analysis of the synthesized methacrylated NAG performed with an EuroEA-Elemental Analyser (Eurovector, Italy), nevertheless suggests a degree of methacrylation in the domain between one and three. In consequence, the obtained polymerized resist is likely to feature linear polymers for methacrylated NAG monomers with a degree of methacrylation of one as well as crosslinked polymer networks composed of methacrylated NAG monomers with a degree above one. The resulting variation in crosslinking density might be responsible for the partly rough surfaces, especially observed for bulky structures, as shown in the next section.

## 6.2 DLW in NAG-based photoresists

After functionalization of the NAG with methacrylate side groups, it can be applied to create photoresists. To obtain a photoresist that allows patterning via two-photon absorption, however, the methacrylated NAG must be dissolved in a proper solvent as well as mixed with an appropriate photoinitiator.

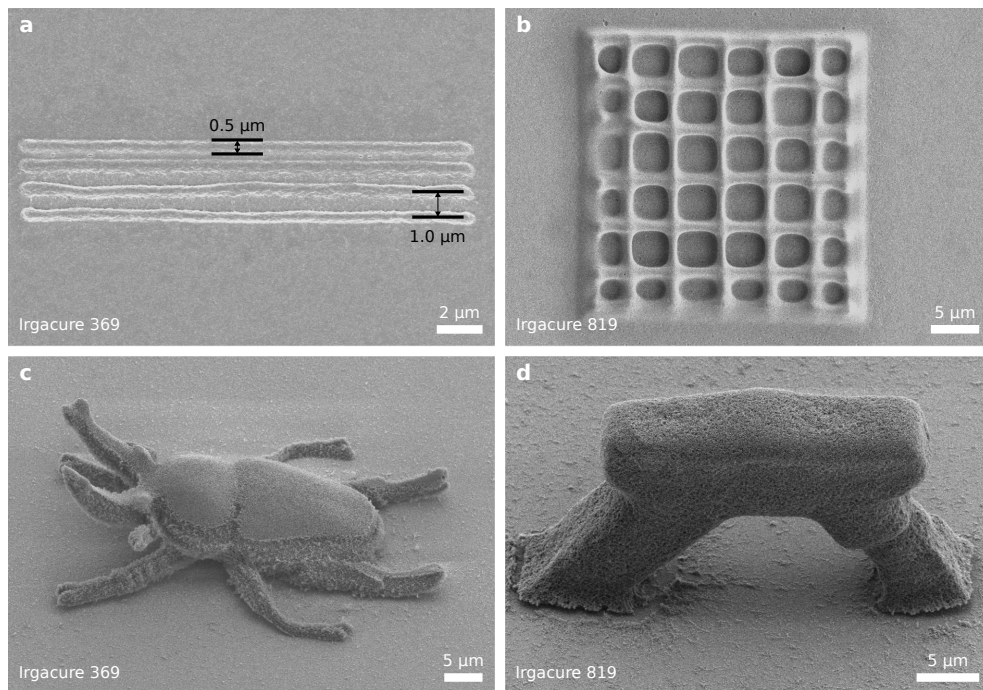


Figure 6.2: SEM micrographs of structures realized with NAG-based photoresists containing either Irgacure 369 or Irgacure 819. **a**, 2D lines printed at a writing speed of  $10 \mu\text{m/s}$  and a laser power of 30% ( $100\% \cong 57.8 \text{ mW}$ ), exhibiting a submicron feature size as well as a micron resolution. **b**, Fabricated 2D grid structure using a speed of  $50 \mu\text{m/s}$  and a power of 90%. **c**, Realization of a 3D model of the rainbow stag beetle at a speed of  $1000 \mu\text{m/s}$  applying 90% laser power. **d**, Written arch using a writing speed of  $100 \mu\text{m/s}$  and a power of 30%, showing the capability to fabricate free standing 3D structures. (**a,b**) reveal top views, while (**c,d**) exhibit side views on the structures at an angle of  $45^\circ$ . Adapted from Ref. <sup>248</sup>

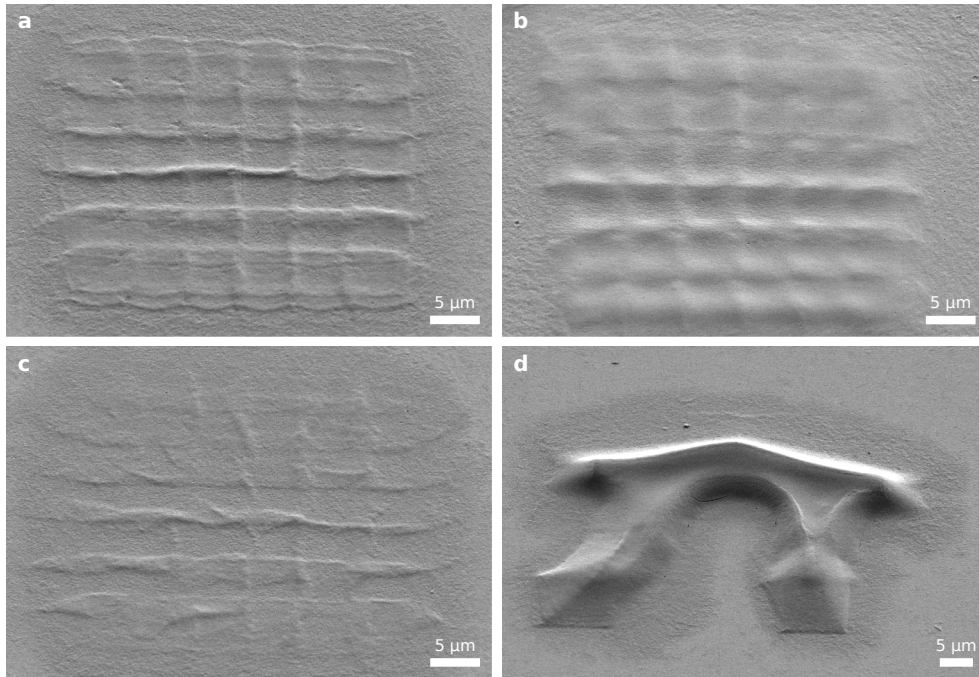


Figure 6.3: SEM micrographs of structures obtained with a NAG-based photoresist containing DETC. **a–c**, Patterned 2D grids using a writing speed of  $20\ \mu\text{m/s}$  and a laser power of 30% (**a**), a writing speed of  $20\ \mu\text{m/s}$  and a laser power of 100% (**b**), as well as a writing speed of  $200\ \mu\text{m/s}$  and a laser power of 50% (**c**), respectively. **d**, Attempt to print an upright arch structure at a speed of  $100\ \mu\text{m/s}$  and a power of 50%. All panels display side views at  $45^\circ$ . Taken from Ref. <sup>248</sup>

Since methacrylated NAG is soluble in DMSO, this solvent is used to first prepare stock solutions, each containing a different photoinitiator at a concentration of 0.05 M. Subsequently, the photoresists are obtained by adding the respective stock solution to the methacrylated NAG until a concentration of 250 g methacrylated NAG per liter is received. Using a magnetic stirrer, the photoresists are mixed overnight and eventually separated for 20 min deploying a centrifuge (Mini-Zentrifuge, Carl Roth GmbH & Co. KG, Germany) to remove unsolved particles.

To find the best suited photoinitiator, a variety of 2D and 3D structures is printed in each photoresist, revealing that Irgacure 369 and 819 provide the best structure quality (Fig. 6.2). Contrarily, photoinitiators such as DETC, which are renowned to be among the most efficient for DLW at  $780\ \text{nm}$ ,<sup>262,263</sup> fail to produce well-defined stable structures, independent of the used writing speed and laser power (cf. Fig. 6.3).

Therefore, the performance of NAG-based resists is further studied for Irgacure 369 (Fig. 6.2a,c) and Irgacure 819 (Fig. 6.2b,d) loaded ones. For 2D structures, typical lateral resolution of  $1\ \mu\text{m}$  and feature sizes in the order of  $500\ \text{nm}$  are observed (Fig. 6.2a), closely matching the properties of a prior published cellulose-based resist.<sup>9</sup> To reach such specifications is crucial for printing biomimetic architectures, since many functional structures found, e.g., in insects, are nano- and microstructures.<sup>2</sup>

Although 2D structures in NAG-based resists can be successfully printed, this comes at the cost of a rather low writing speed. Patterning a 2D grid structure (Fig. 6.2b) at a speed of  $50\ \mu\text{m/s}$  requires already 90% of the total laser power in the case of using Irgacure 819, while similar results are obtained for Irgacure 369. To enable considerably faster printing, the laser power would have to be increased accordingly to obtain the same dose. Thus, no well-defined delicate 2D structures are achieved for higher writing speeds.

In the case of bulky 3D structures, however, higher writing speeds of up to  $1000\ \mu\text{m/s}$  can be reached, as shown in Fig. 6.2c for the printed miniaturized model of a rainbow stag beetle<sup>a</sup>. Together with the fabricated arch structure, which is composed of two skewed pillars topped by an architrave (Fig. 6.2d), this further reveals that free standing 3D structures are feasible, highlighting the ability of the resists for 3D microfabrication.

### 6.3 Identifying appropriate sensitizer–photoinitiator pairs

Compared to a vast number of DLW photoresists which allow for maximum writing speeds of several mm/s or even higher,<sup>262</sup> the NAG-based photoresists presented in the last section feature only a relatively low maximum writing speed, especially for fabrication of delicate 2D structures. However, this disadvantage can be circumvented by adding a suitable sensitizer to the photoresist that forms a pair with the photoinitiator capable to exhibit the sensitization effect.

In principle, a sensitizer is also a photoinitiator, but it must satisfy two additional conditions. On the one hand, the sensitizer should provide a higher absorption than

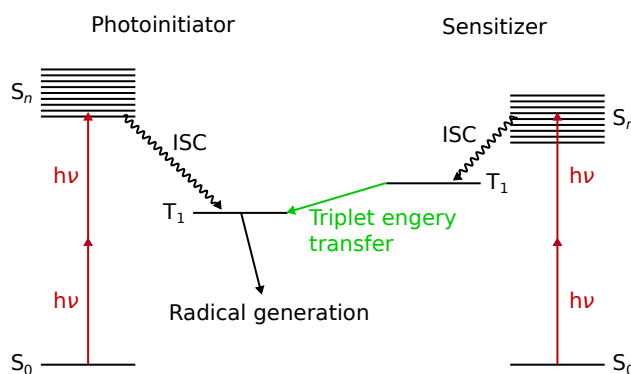


Figure 6.4: Simplified Jablonski diagram of the sensitization effect for two-photon absorption. Due to the larger two-photon absorption cross section of the sensitizer, the  $T_1$  level of the photoinitiator, which is responsible for radical generation, is mainly excited via two-photon absorption in the sensitizer followed by intersystem crossing (ISC) and triplet energy transfer from the  $T_1$  level of the sensitizer to the  $T_1$  level of the photoinitiator. A minor amount of excitation is also provided by two-photon absorption in the photoinitiator, followed by corresponding intersystem crossing.

<sup>a</sup>the free 3D model is received from the website [www.ameede.net](http://www.ameede.net)

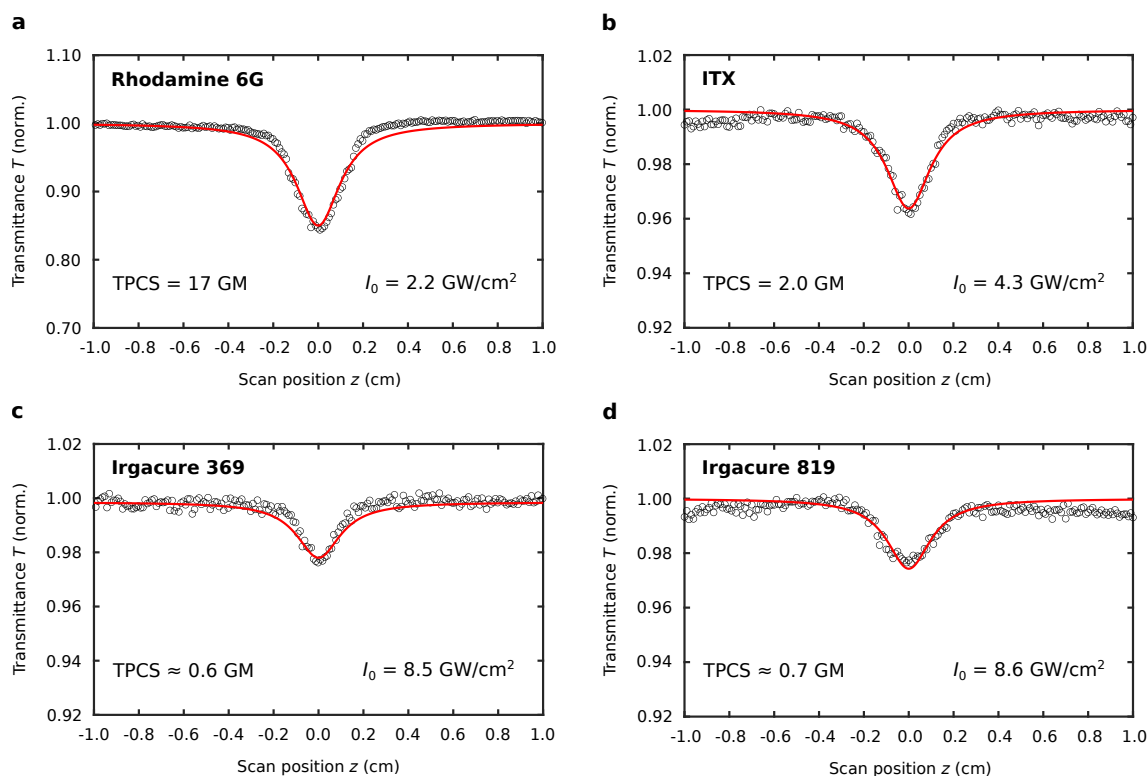


Figure 6.5: Two-photon absorption transmittance dip measured with a  $z$ -scan setup at 780 nm for different compounds. **a**, Rhodamine 6G in methanol. **b**, ITX in DMSO. **c**, Irgacure 369 in DMSO. **d**, Irgacure 819 in DMSO. The measurement data are fitted with Eq. (3.30) in each case (red line). The intensity at the focal spot  $I_0$  is adapted for every compound as denoted in each panel to consider various two-photon absorption coefficients. In addition, the obtained two-photon absorption cross section (TPCS) is given. The ordinate in (**b–d**) is scaled differently than in (**a**) for the sake of detectability of the characteristic dip. Taken from Ref. <sup>248</sup>

the photoinitiator at the applied wavelength, i.e., in the case of DLW a larger two-photon absorption cross section. This is the case, for instance, if the wavelength closely matches the center of the absorption band of the sensitizer, while it is right at the edge of the absorption band of the photoinitiator, as depicted in Fig. 6.4. On the other hand, the triplet energy of the sensitizer must be higher than that of the photoinitiator. As a result, a triplet energy transfer can occur, passing the energy stored in the  $T_1$  state of the sensitizer to the  $T_1$  state of the photoinitiator, where the formation of radicals is initialized (Fig. 6.4). In the meantime, the sensitizer reverts to the ground state being preserved for a new cycle.<sup>59,264</sup>

Because of these conditions, selecting a proper sensitizer–photoinitiator pair conceptually differs from just combining two photoinitiators, as presented elsewhere in the literature.<sup>265</sup> Since the photoinitiator is responsible for crosslinking the monomer, it is convenient to start with choosing an appropriate photoinitiator. As shown in the previous section, Irgacure 369 and 819 are promising candidates in the case of NAG-based photoresists.

To find compatible sensitizers, the triplet energy must be considered first. While Irgacure 369 and 819 offer a triplet energy of 60.0 and 55.5 kcal/mol, respectively,<sup>59</sup> compounds such as ITX (61.4 kcal/mol)<sup>59</sup> or benzophenone (69.1 kcal/mol)<sup>59</sup> are potential candidates. DETC, in contrast, has a triplet energy of 45.7 kcal/mol<sup>263</sup> and is thus not suited as a sensitizer. To serve as a sensitizer, however, the candidates must also possess a higher two-photon absorption cross section than the respective photoinitiator.

For that reason, the two-photon absorption cross section is measured for the photoinitiators (Irgacure 369, 819) as well as for the potential sensitizers (ITX, benzophenone), deploying the (open)  $z$ -scan setup described in Sec. 3.2.3. Prior to taking measurements, the setup used is validated using the well-known two-photon absorption cross section of Rhodamine 6G in methanol at a wavelength of 780 nm, which is 16 GM.<sup>208</sup> As it can be seen in Fig. 6.5a, the here deployed setup provides a value of 17 GM in close agreement with the literature.

Since both the solvent and the wavelength affect the resulting two-photon absorption cross section,<sup>208</sup> for  $z$ -scan measurements the same conditions are applied as for DLW, i.e., a wavelength of 780 nm and DMSO as solvent are deployed. Benzophenone does not show any two-photon absorption, even if the maximum laser power of the  $z$ -scan setup is used. Therefore, it is discarded as a potential sensitizer. In contrast, ITX possesses a two-photon absorption cross section of 2 GM (Fig. 6.5b), which is about three times higher than that of the Irgacure photoinitiators, each revealing a two-photon absorption cross section around 0.6–0.7 GM (Fig. 6.5c,d). In Fig. 6.5, it should be noted that a two times higher laser power must be applied to observe the characteristic two-photon absorption dip in the case of Irgacure 369 and 819 compared to ITX.

The obtained results meet furthermore the expectations, since the two-photon absorption maximum of ITX at 760 nm is indeed close to the applied wavelength, while the two-photon absorption maxima of Irgacure 369 (670 nm) and Irgacure 819 (600 nm) deviate considerably.<sup>266</sup> In consequence, ITX can act as a suitable sensitizer for both Irgacure photoinitiators, which is examined in the section below.

## 6.4 Deploying the sensitization effect for DLW

To test the identified sensitizer–photoinitiator pairs, in the context of DLW, photoresists containing Irgacure 369 and ITX as well as Irgacure 819 and ITX are prepared. The corresponding stock solutions are thereby blended in different ratios, prior to mixing the respective photoresist. Since all stock solutions possess the same molar concentration (cf. Sec. 6.2), the total number of photoactive molecules remains constant, no matter if a single photoinitiator, sensitizer or the corresponding pair is used. Hence, the effect observed below does not arise from increasing the total amount of photoinitiator molecules, as it would be the case for just adding a second initiator, but from a beneficial combination of two initiators leading to a higher

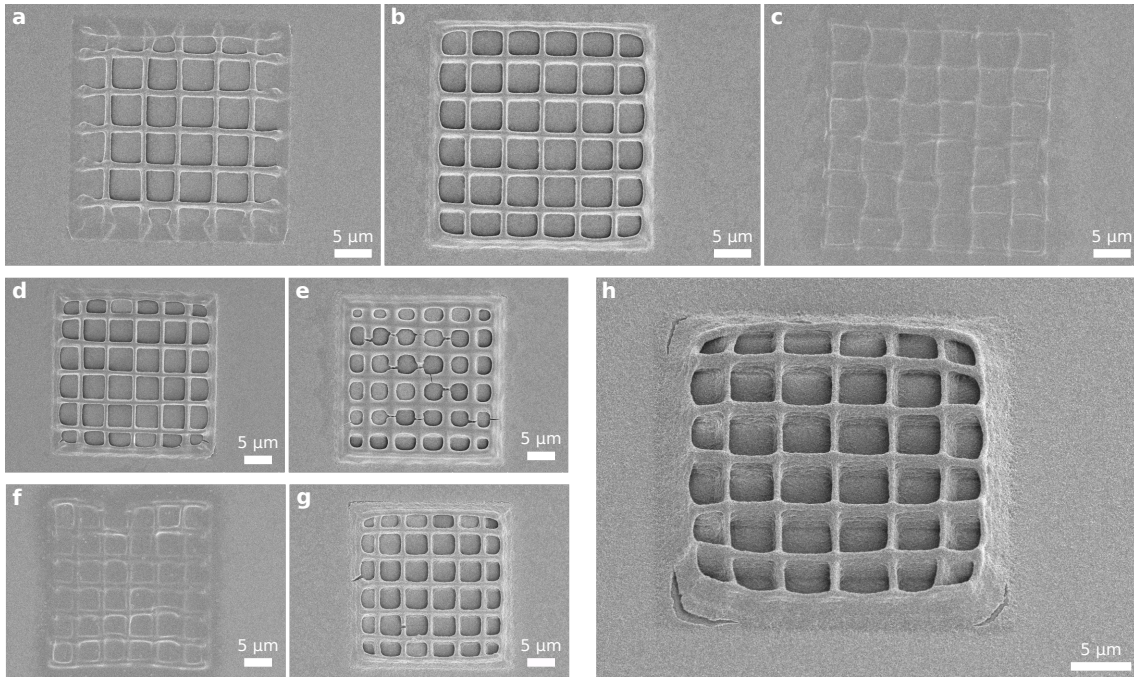


Figure 6.6: SEM micrographs comparing structures fabricated by either applying the photoinitiator, the sensitizer, or the corresponding sensitizer–photoinitiator pair. **a–c**, 2D grid structure obtained via DLW in a photoresist containing Irgacure 369 (**a**), a mixture of Irgacure 369 and ITX in the ratio 3:1 (**b**), and ITX (**c**). A writing speed of  $20\ \mu\text{m/s}$  and a laser power of 30% is used in each case. **d,e** Printing of the same grid structure using Irgacure 369 (**d**) and the combination of Irgacure 369 and ITX (**e**) but at a higher laser power of 50%. **f,g** Corresponding grid structures realized in NAG-based resists comprising Irgacure 819 (**f**) and a mixture of Irgacure 819 and ITX in the ratio 7:1 (**g**), applying a writing speed of  $50\ \mu\text{m/s}$  and a power of 40%. **h**, Same as (**g**) but fabricated at a writing speed of  $500\ \mu\text{m/s}$  at a power of 50%. This panel shows a side view at an angle of  $30^\circ$ . Taken from Ref. <sup>248</sup>

absorption efficiency. Moreover, for a fair comparison between different resists, only structures fabricated with the same settings, i.e., writing speed and laser power, are directly compared.

Figure 6.6a–c displays similar grid structures fabricated in NAG-based resists comprising solely Irgacure 369 (**a**), a mix of Irgacure 369 and ITX (**b**) as well as only ITX (**c**). While the resists containing Irgacure 369 solely or in mixture with ITX exhibit raised lines for the applied writing condition ( $20\ \mu\text{m/s}$  writing speed and 30% laser power), barely no lines can be discerned for the resist relying purely on ITX. Instead, a weak contrast between the written structure and the substrate can be observed, implying that the applied laser power is below the power threshold needed to obtain raised structure. Indeed, solid lines can be fabricated if a laser power close to 100% is used.

Comparing both resists including Irgacure 369, it can be seen that applying the sensitizer–photoinitiator pair results in a considerably better overall structure quality, especially at the edge of the structure (cf. Fig. 6.6a and b). This shows that the

sensitizer–photoinitiator pair significantly outperforms both the photoinitiator and the sensitizer when used alone.

Since Irgacure 369 crosslinks the methacrylated NAG more efficiently than ITX, this advantage arises from maximizing the amount of radicalized Irgacure 369 molecules due to the sensitization effect, as explained in the previous section. However, since Irgacure 369 acts as a photoinitiator itself, a comparable amount of radicalized Irgacure 369 molecules can be also obtained by increasing the applied power to 50%. This indeed results in a similar structure quality using Irgacure 369 alone (Fig. 6.6d). Conversely, the same power enhancement leads to a notable overexposure of the lines in the case of the sensitizer–photoinitiator pair, as revealed in Fig. 6.6e. Altogether, this demonstrates that the sensitization effect diminishes the needed dose, which is advantageous since the writing speed at a given dose is limited by the maximum laser power of the device used.

To show that the sensitization effect is rather universal than limited to a particular sensitizer–photoinitiator pair or writing conditions, accompanying experiments are performed for Irgacure 819 and ITX. Applying a NAG-based resist with Irgacure 819 at a writing speed of 50  $\mu\text{m/s}$ , solid structures might be received for high powers in the order of 90% (Fig. 6.2b), but not for a power as low as 40% (Fig. 6.6f). Deploying the corresponding sensitizer–photoinitiator pair, in contrast, raised lines can be realized already at 40% laser power (Fig. 6.6g), where neither the photoinitiator nor the sensitizer alone allows for structure fabrication.

It should be further noted that this effect is reached by adding only a minor amount of ITX, here one part per seven parts Irgacure 819. This further proves the successful adaption of the sensitization effect for DLW, as the sensitizer will be generally not cleaved during sensitization, allowing to reuse the same sensitizer molecule several times.<sup>264</sup>

While the maximum writing speed for delicate 2D structures in Irgacure 819 loaded resists is restricted to roughly 50  $\mu\text{m/s}$  due to the needed dose, writing speeds of up to 500  $\mu\text{m/s}$  become available if the sensitizer–photoinitiator pair is used instead (Fig. 6.6h). This enhancement by an order of magnitude is the result of a significant decrease of the required dose due to the sensitization effect, and thus highlights the benefit of utilizing the sensitization effect for DLW.





## 7 Outlook

While each of the issues explored in the last three chapters provides a starting point for further research, this outlook is intended to mainly highlight the next steps in the development of bio-based resists, as some of them have already been taken. Nevertheless, possible further investigations resulting from the findings of Ch. 4 and Ch. 5 will first be briefly summarized.

The novel mixing rule deduced here is currently limited to calculate the real part of the effective refractive index for heterogeneous dielectric materials with negligible absorption. Thus, in a subsequent step, the investigation can be expanded to evaluate the complex effective refractive index for structures incorporating also metallic and absorbing materials. While the successful application of the new mixing rule to non-cermet structures is shown for one example, a systematic analysis of the influence of particle shape and size distribution would be worthwhile. In this, the field of application could be delimited more precisely, while further modifications might be found, which enable to include a greater variety of structures. Last but not least, the slope of the empirically found linear function might provide a good starting point to derive a mixing rule for large particles *a priori*.

In the context of this thesis, leakage from weakly localized photonic modes is found to significantly contribute to the brilliant whiteness of ultrathin scattering media. However, since coherent backscattering is a frequently observed phenomenon, it is believed that the weak localization assisted scattering regime is not exclusive for brilliant white structures but emerges in many other random media as well. Investigating its occurrence for a great variety of structures could provide a more general insight into the temporal dynamics of light transport and its relation to the morphology of the underlying structure. For instance, this might be germane to sensing through turbid media or random lasing action in disordered media with gain.<sup>74,267,268</sup> In addition, the observed long-living local hotspots offer the potential for enhanced light-matter interaction, a quantity that is subject to optimization in the field of solar energy harvesting or optical sensor applications, to name just a few.<sup>38,67,269,270</sup>

While the sensitization effect is studied for two different sensitizer–photoinitiator pairs and a specific monomer, there is no fundamental limit to these compounds. On the contrary, other sensitizer–photoinitiator combinations might be found that exhibit an even stronger sensitization effect. Since most photoinitiators are soluble in common photoresist formulations, the sensitization effect can be straightforwardly applied in a broad spectrum of resists. Moreover, highly reactive UV photoinitiators, which are currently inaccessible to DLW because of their vanishingly small two-photon absorption cross section at the wavelength used, may become available due to the sensitization effect, as only the sensitizer needs to provide a sufficient absorption. However, while the sensitization effect is beneficial in a myriad of applications that demand large scale fabrication in a decent time, the use of one or even two photoini-

tiators is often undesirable in applications that require biocompatibility due to the cytotoxic nature of many photoinitiators.<sup>271</sup> This issue is overcome in photoresists which can be crosslinked without any additional photoinitiator. Such formulations are received by attaching side groups to the underlying monomer that enable polymerization via two-photon absorption by the molecule itself.

While adding such side groups to obtain an alternative photoinitiator-free NAG-based resist is desirable in the long term, the proof of concept of a photoinitiator-free bio-based resist is done using cellulose diacetate (CDA) instead. In contrast to NAG, the synthesis of cellulose-based resists is an established and well controllable process,<sup>9,245</sup> reducing the imponderables in the implementation of new functionalization concepts.

In the sections below, the main aspects of the synthesis as well as the first results of DLW in photoinitiator-free cellulose-based resists are summarized. The presented study was also done in cooperation with Maximilian Rothhammer and Maximilian Maier of Cordt Zollfrank's group, who synthesized, functionalized, and characterized the CDA derivatives. The outcomes of this work are published in Ref.<sup>272</sup> providing all details of this study.

## 7.1 Synthesis of bifunctional cellulose diacetate derivatives

While polymerization of photoinitiator-loaded cellulose-based resists relies on a radical chain-growth mechanism via methacrylic side groups, a different strategy is used to obtain photoinitiator-free resists. The strategy's foundation lies in a step-growth mechanism using a thiol-ene reaction, as this reaction can be driven without a photoinitiator<sup>273</sup> and thiol-ene polymerization have been already successfully exploited for DLW.<sup>274,275</sup> Both properties, however, are not yet combined in a bio-based resist, i.e., the presented thiol-ene bio-resists for DLW still demand a photoinitiator.<sup>275</sup> Consequently, the approach shown in this section aims for a functionalization that enables a thiol-ene polymerization without using any photoinitiator.

Since the thiol-conjugated crosslinking results from the formation of thioether bonds between thiol and alkenes,<sup>276</sup> two distinct side groups must be added to the CDA backbone. Here, two different bifunctional CDA derivatives are prepared, deploying a thiol moiety and either an olefinic (CDA-SH 4-pentenoate) or a methacrylic side group (CDA-SH methacrylate).

The corresponding synthesis consists of three steps, as schematically shown in Fig. 7.1 for CDA-SH 4-pentenoate. In the first step, using 3,3'-dithiodipropionic acid, a monobenzylated asymmetric disulfide with one inert end and one reactive carboxylic group is synthesized (Fig. 7.1, top), according to the procedure presented in the literature.<sup>277</sup> Since this disulfide compound is the center of the thiolation strategy to introduce the reactive thiol group in the final step,<sup>277</sup> it is attached to the CDA backbone deploying DCC coupling with DMAP as catalyst (Fig. 7.1, center left). In

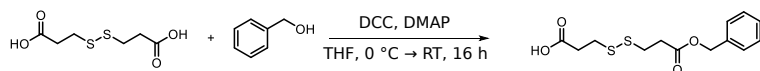
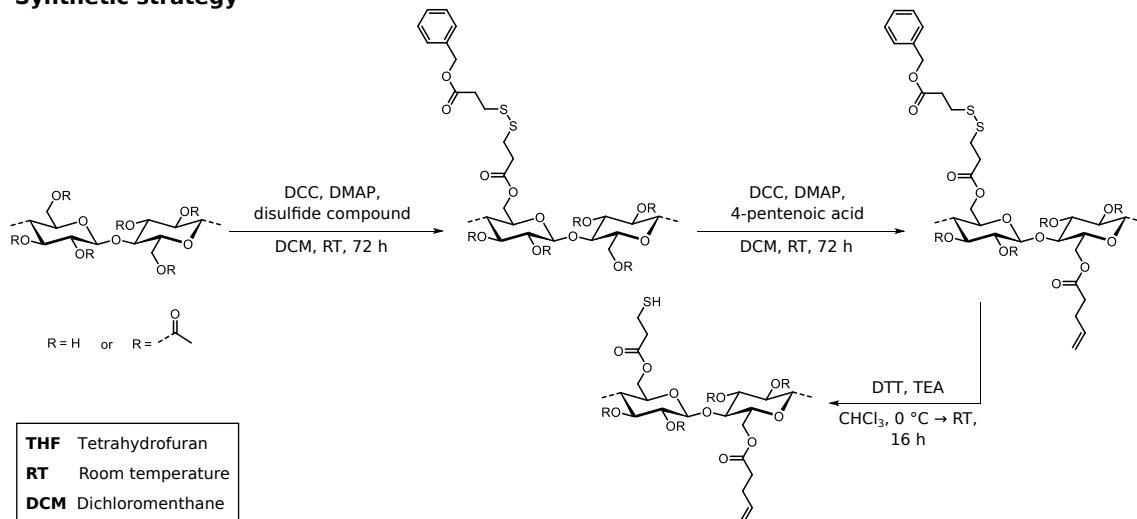
**Synthesis disulfide compound****Synthetic strategy**

Figure 7.1: Sketch of the synthesis steps to obtain CDA-SH 4-pentenoate. Depending on the degree of substitution R can be hydrogen, acetyl, disulfide substituent, olefin, or thiol substituent. Adapted from the accepted manuscript version of Ref. <sup>272</sup> The figure is excluded from the CC BY license of this thesis.

addition, an esterification reaction, also based on DCC coupling, is used to add either the methacrylate or the 4-pentenoate functionalities to the backbone, as shown in Fig. 7.1, center right for 4-pentenoate. Eventually, the thiol activation is achieved by a disulfide cleavage using 1,4-dithiothreitol (DTT, Alfa Aesar) as a reducing agent and triethylamine (TEA, Acros Organics) as a catalyst (Fig. 7.1, bottom).

A detailed description of each synthesis step can be found in Ref. <sup>272</sup> As in the case of the NAG functionalization, the successful synthesis is monitored and confirmed using FTIR and NMR measurements, as also exhibited in this publication.

## 7.2 DLW in photoinitiator-free cellulose-based resists

The CDA derivatives presented in the last section are solid, so a proper solvent must be added to produce DLW-suitable photoresists. Although there are several possible solvents, DMF is chosen because it is neither highly volatile like acetone or chloroform, nor does it affect already polymerized structures as DMSO does.

Once the solvent has been selected, it is necessary to test various concentrations to obtain a suitable viscosity. Applying the resist to the substrate with a syringe can cause unwanted air bubbles in the resist if its viscosity is too high. On the other

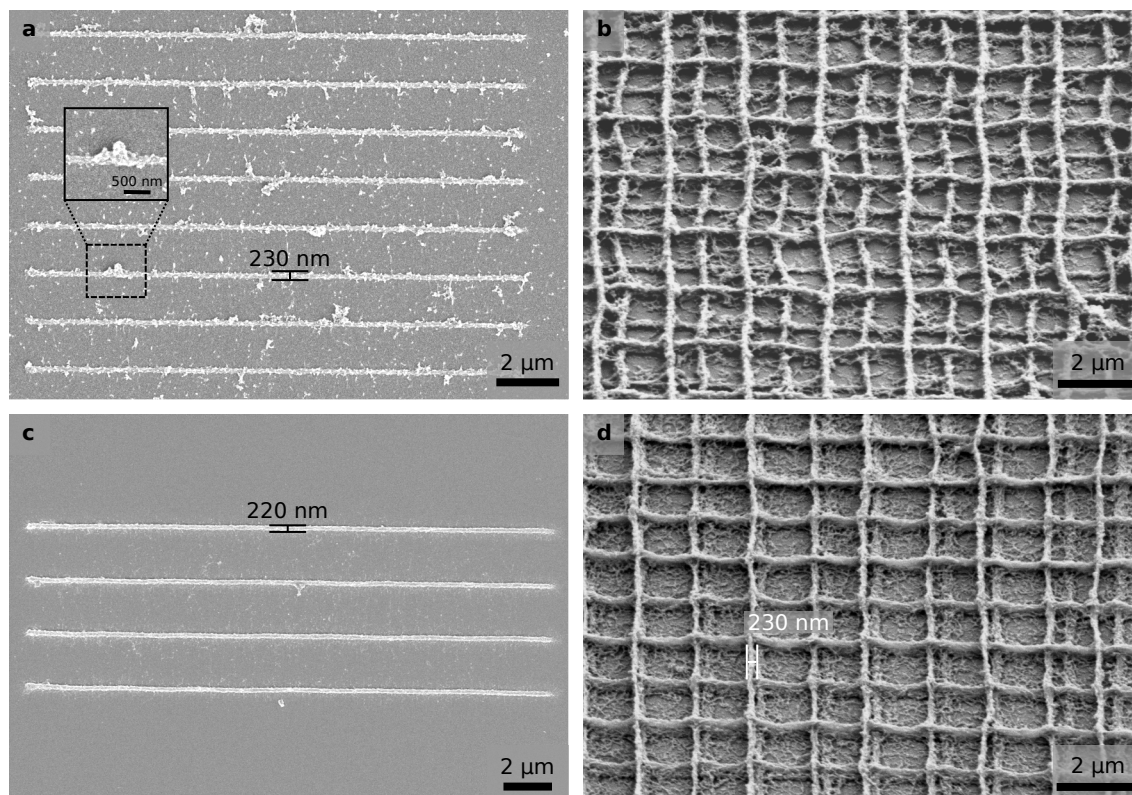


Figure 7.2: SEM micrographs of structures printed in photoinitiator-free cellulose-based resists. **a**, Fabricated 2D line grid using CDA-SH 4-pentenoate. The magnified view shown in the inset reveals one of the bulges observed on the lines. **b**, Printed four-layer woodpile structure deploying the same resist. In both cases a writing speed of  $100\ \mu\text{m/s}$  and a laser power of 100% are applied. **c**, 2D line pattern obtained with a CDA-SH methacrylate resist. **d**, Four-layer grid structure written in the same resist. The same writing speed of  $20\ \mu\text{m/s}$  is used for both structures while the laser power differs from 80% (**c**) to 40% (**d**). In panel (**b**) and (**d**) a side view at  $45^\circ$  is depicted. Taken from the accepted manuscript version of Ref. <sup>272</sup> The figure is excluded from the CC BY license of this thesis.

hand, a drop of a highly fluid resist does not stay in form but tends to disperse during a print job. This restricts the maximum height and leads to undesired dynamics within the drop. Moreover, the viscosity also influences the radical diffusion within the resist, which has an effect on the obtainable feature size and resolution.<sup>200</sup>

Studying different mixing ratios, a good trade-off between handling of the resist and resulting structure quality is found for concentrations between 100 g and 140 g CDA-SH 4-pentenoate per liter DMF. In the case of CDA-SH methacrylate, the optimum concentration is found at a distinctly lower value of about 50 g/L.

The successful use of the thiol-ene reaction for photoinitiator-free DLW can be seen in Fig. 7.2, displaying various structures printed in a CDA-SH 4-pentenoate resist (Fig. 7.2a,b) and a CDA-SH methacrylate resist (Fig. 7.2c,d). Both resists enable the fabrication of 2D structures with features sizes as small as 220–230 nm, however, in terms of structure quality the CDA-SH 4-pentenoate resist (Fig. 7.2a) is clearly

surpassed by the CDA-SH methacrylate resist (Fig. 7.2c). While printed lines in the former suffer from the frequent formation of bulges (cf. zoomed view in Fig. 7.2a), well-defined, sharp lines can be realized using CDA-SH methacrylate.

The observed difference can be ascribed to the distinct character of the added side groups. Compared to the methacrylic side group, the terminal double bond of the olefinic group is sterically less inhibited, resulting in an enlargement of the range where the polymerization can be induced. In combination with the omnipresent diffusion of radicals, unwanted polymerization tends to occur between features written in close proximity to each other. As a result, the formation of bulges in such line grids is facilitated while the achievable resolution is diminished.

Due to this issue, fabrication of filigree 3D structures is a challenge. While the general shape of the four-layer woodpile structure printed in a CDA-SH 4-pentenoate resist can be recognized in Fig. 7.2b, bulges also emerge here, hampering a better structure quality. As in the case of 2D structures, the CDA-SH methacrylate resist also enables a better structure quality in 3D. The four-layer grid structure displayed in Fig. 7.2d indeed exhibits some lines that bridge the underlying lines, showing the fundamental potential for 3D fabrication. However, unintended polymerization also occurs with CDA-SH methacrylate, which, although not as pronounced as with the other derivative, results in small filaments between adjacent features. As a result, the total structure height of delicate 3D architectures is currently limited to a few microns, as a polymer film starts to overgrow larger structures. Bulky structures, nevertheless, can reach larger heights, e.g., simple blocks taller than 10  $\mu\text{m}$  are successfully fabricated.

Despite some further improvements are necessary to print complex 3D architectures, the results indicate the potential of the proposed functionalization to create photoinitiator-free bio-based resists for DLW. It further should be noted that remarkably small feature sizes in the order of 230 nm are not only obtained for 2D but also for simple 3D structures (cf. Fig. 7.2d). This is just about the half of the minimum feature size reached with current photoinitiator-loaded cellulose-based resists,<sup>9</sup> underlining the fundamental potential of using thiol-ene polymerization to improve existing photoresists.



## 8 Conclusions

In this dissertation, the brilliant white scales of the beetle *Cyphochilus* are considered from two different viewpoints, namely from an optical and from a material perspective. Regarding their optical properties, first a new mixing rule to accurately calculate the effective refractive index in the presence of large features is deduced. Subsequently, different light transport regimes that occur in the scales are identified and their respective contribution to the whiteness is assessed. The material aspect of the scales serves as an inspiration for the development of novel bio-based photoresists for 3D microfabrication in the second part of the thesis. In addition, this work presents an innovative concept for enhancing writing speed by transferring the sensitization effect from UV curing to DLW.

To derive a new mixing rule, FDTD simulations are used to systematically investigate the influence of the particle size on the resulting effective refractive index. For this purpose, the condition that the forward scattering amplitude vanishes in the case of index matching between the effective medium and the background is implemented for the first time in FDTD simulations. This approach enables a fast and accurate evaluation for arbitrary structures and any feature size as long as the investigated medium behaves as an effective one. Indeed, in the regime where the Maxwell–Garnett mixing rule is valid, the simulation results are in perfect agreement with the theoretical predictions both for the real and imaginary part.

For composite media with particles sizes beyond this regime, the prediction of the Maxwell–Garnett mixing is shown to break down as expected. Instead, for sphere size parameters between  $x \approx 1$  and  $x \approx 2$ , it is found that the effective refractive index can be described by a simple quadratic polynomial function in good approximation. The coefficients of this polynomial are retrieved from an empirical linear function. Therefore, an easy-to-use mixing rule is presented that greatly extends the current upper bound of such rules ( $x \lesssim 1$ ) to encompass particles approaching the boundary of the geometrical optics regime.

Originally, the here reported mixing rule is derived for random sphere packings. Nevertheless, it is exhibited that this mixing rule is also applicable to complex interconnected structures composed of non-spherical particles. Testing several realizations of the DBS structure, i.e., a model of the white beetle scales, reveals in all cases good agreement between the simulation outcomes and the prediction of the presented mixing rule. Common mixing rules such as those of Maxwell–Garnett and Bruggeman, in contrast, fail to yield the effective refractive index correctly. Since a large spectrum of natural as well as artificial structures feature particles in the scope between  $x \approx 1$  and  $x \approx 2$ , the novel mixing rule is believed to replace the widespread Maxwell–Garnett and Bruggeman mixing rules in a myriad of situations.

The influence of coherent effects on the brilliant whiteness of the beetle scales is studied experimentally and in simulations. Using spectromicroscopy measurements, the time-resolved electric field is reconstructed, which shows a characteristic beating

behavior for light scattered from the scales. Analyzing the electric field by means of the Wigner distribution function and the short-time Fourier transform, two different light transport regimes are identified. An initial diffusion-like transport is followed by a regime where scattering via leakage from weakly localized photonic modes dominates. It is further shown that the transition between both regimes coincides with the round trip time of a light pulse propagating through the scale, assuming the scale acts as an effective medium.

Similar experimental results are obtained for a direct laser written DBS structure. Compared to the original DBS model, the structures must be scaled up to allow for fabrication. As a result, the same two transport regimes as in the scales are found, but on an accordingly shifted time scale.

The distribution of resonance lifetimes measured for the scales as well as simulated for a computer model of the intra-scale network and the DBS model follows in all cases a similar log-normal shape, a typical signature of weak localization. Simulations are additionally used to verify the identification of the experimentally observed transport regimes. While the initial diffusive transport is well modeled by fully coherent FDTD and incoherent Monte Carlo simulations, the latter fail to correctly describe the behavior after the characteristic pulse round trip time is reached. Moreover, FDTD simulations exhibit persistent local hotspots that are attributed to the antinodes of randomly closed scattering loops, giving rise to the experimentally observed resonances.

Since many functional structures found in nature, such as the white beetle scales, are composed of chitin, its monomer unit N-acetyl-D-glucosamine is modified to enable its use for 3D microfabrication via DLW. To obtain a crosslinkable compound, a methacrylic side group is attached to the NAG backbone via an esterification reaction. The successful functionalization is confirmed performing FTIR and NMR measurements on the reagents and products. Applying photoresists composed of the functionalized NAG, a proper solvent and photoinitiator, various microstructures are realized, showing micron resolution, submicron feature sizes and the ability to print free standing 3D structures.

In contrast to existing animal carbohydrate-based resists, the reported resists rely on a non-hydrogel formulation and thus establish a new class of photoresists. This first realization of these resists may pave the way for synthesizing more complex animal-based carbohydrates like chitin to allow for microfabrication. Such rigid materials are frequently deployed in the animal kingdom as the fundamental building block of functional structures. Thus, the opportunity of 3D printing these materials offers new routes to replicate these structures for analyzing their functionality or for bionic tasks.

While a single photoinitiator is sufficient to crosslink the NAG-based resists, it is demonstrated that the addition of a suitable sensitizer can enhance the maximum writing speed by up to an order of magnitude. To transfer the sensitization effect from the renowned case of one-photon absorption in UV curing to two-photon ab-



---

sorption in DLW, suitable sensitizer–photoinitiator pairs must be selected. For this purpose, an open  $z$ -scan setup is used to measure the two-photon absorption cross section of various photoinitiators identifying two appropriate pairs, each using ITX as sensitizer and either Irgacure 369 or Irgacure 819 as photoinitiator. While both pairs are capable to increase the maximum writing speed in NAG-based resists, the effect is believed to be also beneficial for other DLW-suitable photoresists. In addition, due to the universal nature of the sensitization effect further sensitizer–photoinitiator pairs might be found that outperform the current ones.

Finally, a short outlook is given on using a thiol-ene reaction to receive bio-based photoresists that enables DLW without the need of any photoinitiator. In this, thiol moieties and either olefinic or methacrylic side groups are added to a cellulose diacetate backbone to prove the concept. Beside developing a proper synthesis scheme, the successful fabrication of first structures via DLW in photoinitiator-free cellulose-based resists is shown. Although the current synthesis requires some improvement to also enable complex, large scale 3D architectures, the feasibility of the fundamental concept to shed cytotoxic photoinitiators in bio-based resists is confirmed.



## References

- <sup>1</sup>S. Dou, H. Xu, J. Zhao, K. Zhang, N. Li, Y. Lin, L. Pan, and Y. Li, “Bioinspired microstructured materials for optical and thermal regulation”, *Advanced Materials* **33**, 2000697 (2021).
- <sup>2</sup>T. B. H. Schroeder, J. Houghtaling, B. D. Wilts, and M. Mayer, “It’s not a bug, it’s a feature: Functional materials in insects”, *Advanced Materials* **30**, 1705322 (2018).
- <sup>3</sup>L. Ge, S. Sethi, L. Ci, P. M. Ajayan, and A. Dhinojwala, “Carbon nanotube-based synthetic gecko tapes”, *Proceedings of the National Academy of Sciences* **104**, 10792–10795 (2007).
- <sup>4</sup>L. Wang, Y. Hui, C. Fu, Z. Wang, M. Zhang, and T. Zhang, “Recent advances in *Gecko*-inspired adhesive materials and application”, *Journal of Adhesion Science and Technology* **34**, 2275–2291 (2020).
- <sup>5</sup>K. Autumn, M. Sitti, Y. A. Liang, A. M. Peattie, W. R. Hansen, S. Sponberg, T. W. Kenny, R. Fearing, J. N. Israelachvili, and R. J. Full, “Evidence for van der Waals adhesion in gecko setae”, *Proceedings of the National Academy of Sciences* **99**, 12252–12256 (2002).
- <sup>6</sup>J. Jaramillo-Fernandez, H. Yang, L. Schertel, G. L. Whitworth, P. D. Garcia, S. Vignolini, and C. M. Sotomayor-Torres, “Highly-scattering cellulose-based films for radiative cooling”, *Advanced Science* **9**, 2104758 (2022).
- <sup>7</sup>S. Wang, A. Lu, and L. Zhang, “Recent advances in regenerated cellulose materials”, *Progress in Polymer Science* **53**, 169–206 (2016).
- <sup>8</sup>Y. Chen, L. Zhang, C. Mei, Y. Li, G. Duan, S. Agarwal, A. Greiner, C. Ma, and S. Jiang, “Wood-inspired anisotropic cellulose nanofibril composite sponges for multifunctional applications”, *ACS Applied Materials & Interfaces* **12**, 35513–35522 (2020).
- <sup>9</sup>M. Rothhammer, M.-C. Heep, G. von Freymann, and C. Zollfrank, “Enabling direct laser writing of cellulose-based submicron architectures”, *Cellulose* **25**, 6031–6039 (2018).
- <sup>10</sup>W. Fan, J. Zeng, Q. Gan, D. Ji, H. Song, W. Liu, L. Shi, and L. Wu, “Iridescence-controlled and flexibly tunable retroreflective structural color film for smart displays”, *Science Advances* **5**, eaaw8755 (2019).
- <sup>11</sup>W. Zhang, H. Tian, T. Liu, H. Liu, F. Zhao, X. Li, C. Wang, X. Chen, and J. Shao, “Chameleon-inspired active tunable structural color based on smart skin with multi-functions of structural color, sensing and actuation”, *Materials Horizons* (2023).

- <sup>12</sup>H. Zhou, J. Xu, X. Liu, H. Zhang, D. Wang, Z. Chen, D. Zhang, and T. Fan, “Bio-inspired photonic materials: Prototypes and structural effect designs for applications in solar energy manipulation”, *Advanced Functional Materials* **28**, 1705309 (2018).
- <sup>13</sup>R. H. Siddique, Y. J. Donie, G. Gomard, S. Yalamanchili, T. Merdzhanova, U. Lemmer, and H. Hölscher, “Bioinspired phase-separated disordered nanostructures for thin photovoltaic absorbers”, *Science Advances* **3**, e1700232 (2017).
- <sup>14</sup>S. Kinoshita, S. Yoshioka, and J. Miyazaki, “Physics of structural colors”, *Reports on Progress in Physics* **71**, 076401 (2008).
- <sup>15</sup>A. R. Parker, “515 million years of structural colour”, *Journal of Optics A: Pure and Applied Optics* **2**, R15 (2000).
- <sup>16</sup>P. Vukusic, B. Hallam, and J. Noyes, “Brilliant whiteness in ultrathin beetle scales”, *Science* **315**, 348 (2007).
- <sup>17</sup>T. Lemcoff, L. Alus, J. S. Haataja, A. Wagner, G. Zhang, M. J. Pavan, V. J. Yallapragada, S. Vignolini, D. Oron, L. Schertel, and B. A. Palmer, “Brilliant whiteness in shrimp from ultra-thin layers of birefringent nanospheres”, *Nature Photonics*, 1–9 (2023).
- <sup>18</sup>L. Pattelli, A. Egel, U. Lemmer, and D. S. Wiersma, “Role of packing density and spatial correlations in strongly scattering 3D systems”, *Optica* **5**, 1037–1045 (2018).
- <sup>19</sup>F. Utel, L. Cortese, D. S. Wiersma, and L. Pattelli, “Optimized white reflectance in photonic-network structures”, *Advanced Optical Materials* **7**, 1900043 (2019).
- <sup>20</sup>S. M. Luke, B. T. Hallam, and P. Vukusic, “Structural optimization for broadband scattering in several ultra-thin white beetle scales”, *Applied Optics* **49**, 4246–4254 (2010).
- <sup>21</sup>M. Burrese, L. Cortese, L. Pattelli, M. Kolle, P. Vukusic, D. S. Wiersma, U. Steiner, and S. Vignolini, “Bright-white beetle scales optimise multiple scattering of light”, *Scientific Reports* **4**, 6075 (2014).
- <sup>22</sup>L. Cortese, L. Pattelli, F. Utel, S. Vignolini, M. Burrese, and D. S. Wiersma, “Anisotropic light transport in white beetle scales”, *Advanced Optical Materials* **3**, 1337–1341 (2015).
- <sup>23</sup>C. Åkerlind, H. Arwin, T. Hallberg, J. Landin, J. Gustafsson, H. Kariis, and K. Järrendahl, “Scattering and polarization properties of the scarab beetle *Cyphochilus insulanus* cuticle”, *Applied Optics* **54**, 6037–6045 (2015).
- <sup>24</sup>B. D. Wilts, X. Sheng, M. Holler, A. Diaz, M. Guizar-Sicairos, J. Raabe, R. Hoppe, S.-H. Liu, R. Langford, O. D. Onelli, D. Chen, S. Torquato, U. Steiner, C. G. Schroer, S. Vignolini, and A. Sepe, “Evolutionary-optimized photonic network structure in white beetle wing scales”, *Advanced Materials* **30**, 1702057 (2018).

- 
- <sup>25</sup>D. T. Meiers, M.-C. Heep, and G. von Freymann, “Invited article: Bragg stacks with tailored disorder create brilliant whiteness”, *APL Photonics* **3**, 100802 (2018).
- <sup>26</sup>G. Jacucci, O. D. Onelli, A. De Luca, J. Bertolotti, R. Sapienza, and S. Vignolini, “Coherent backscattering of light by an anisotropic biological network”, *Journal of the Royal Society Interface Focus* **9**, 20180050 (2019).
- <sup>27</sup>S. L. Burg, A. Washington, D. M. Coles, A. Bianco, D. McLoughlin, O. O. Mykhaylyk, J. Villanova, A. J. C. Dennison, C. J. Hill, P. Vukusic, S. Doak, S. J. Martin, M. Hutchings, S. R. Parnell, C. Vasilev, N. Clarke, A. J. Ryan, W. Furnass, M. Croucher, R. M. Dalgliesh, S. Prevost, R. Dattani, A. Parker, R. A. L. Jones, P. A. Fairclough, and A. J. Parnell, “Liquid–liquid phase separation morphologies in ultra-white beetle scales and a synthetic equivalent”, *Communications Chemistry* **2**, 100 (2019).
- <sup>28</sup>S. H. Lee, S. M. Han, and S. E. Han, “Anisotropic diffusion in *Cyphochilus* white beetle scales”, *APL Photonics* **5**, 056103 (2020).
- <sup>29</sup>S. H. Lee, S. M. Han, and S. E. Han, “Nanostructure regularity in white beetle scales for stability and strong optical scattering”, *Optical Materials Express* **11**, 1692–1704 (2021).
- <sup>30</sup>J. S. Haataja, G. Jacucci, T. G. Parton, L. Schertel, and S. Vignolini, “Topological invariance in whiteness optimisation”, *Communications Physics* **6**, 137 (2023).
- <sup>31</sup>F. Liu, B. Q. Dong, X. H. Liu, Y. M. Zheng, and J. Zi, “Structural color change in longhorn beetles *Tmesisternus isabellae*”, *Optics Express* **17**, 16183–16191 (2009).
- <sup>32</sup>M. Wang, X. Xiang, and X. Wan, “Divergence in gut bacterial community among life stages of the rainbow stag beetle *Phalacrognathus muelleri* (Coleoptera: Lucanidae)”, *Insects* **11**, 719 (2020).
- <sup>33</sup>B. D. Wilts, J. Otto, and D. G. Stavenga, “Ultra-dense, curved, grating optics determines peacock spider coloration”, *Nanoscale Advances* **2**, 1122–1127 (2020).
- <sup>34</sup>G. Labeyrie, E. Vaujour, C. A. Mueller, D. Delande, C. Miniatura, D. Wilkowski, and R. Kaiser, “Slow diffusion of light in a cold atomic cloud”, *Physical Review Letters* **91**, 223904 (2003).
- <sup>35</sup>R. Ruppin, “Evaluation of extended Maxwell-Garnett theories”, *Optics Communications* **182**, 273–279 (2000).
- <sup>36</sup>P.-E. Wolf and G. Maret, “Weak localization and coherent backscattering of photons in disordered media”, *Physical Review Letters* **55**, 2696 (1985).
- <sup>37</sup>M. P. van Albada and A. Lagendijk, “Observation of weak localization of light in a random medium”, *Physical Review Letters* **55**, 2692 (1985).
- <sup>38</sup>D. Differt, B. Soleymanzadeh, F. Lükermann, C. Strüber, W. Pfeiffer, and H. Stiebig, “Enhanced light absorption in nanotextured amorphous thin-film silicon caused by femtosecond-laser materials processing”, *Solar Energy Materials and Solar Cells* **135**, 72–77 (2015).

- <sup>39</sup>M. Aeschlimann, T. Brixner, D. Differt, U. Heinzmann, M. Hensen, C. Kramer, F. Lükermann, P. Melchior, W. Pfeiffer, M. Piecuch, C. Schneider, H. Stiebig, C. Strüber, and P. Thielen, “Perfect absorption in nanotextured thin films via Anderson-localized photon modes”, *Nature Photonics* **9**, 663–668 (2015).
- <sup>40</sup>J. K. Hohmann, M. Renner, E. H. Waller, and G. von Freymann, “Three-dimensional  $\mu$ -printing: An enabling technology”, *Advanced Optical Materials* **3**, 1488–1507 (2015).
- <sup>41</sup>H. Wang, W. Zhang, D. Ladika, H. Yu, D. Gailevičius, H. Wang, C.-F. Pan, P. N. S. Nair, Y. Ke, T. Mori, J. Y. E. Chan, Q. Ruan, M. Farsari, M. Malinauskas, S. Juodkazis, M. Gu, and J. K. W. Yang, “Two-photon polymerization lithography for optics and photonics: Fundamentals, materials, technologies, and applications”, *Advanced Functional Materials*, 2214211 (2023).
- <sup>42</sup>A. K. Au, W. Huynh, L. F. Horowitz, and A. Folch, “3D-printed microfluidics”, *Angewandte Chemie International Edition* **55**, 3862–3881 (2016).
- <sup>43</sup>A. Lüken, M. Geiger, L. Steinbeck, A.-C. Joel, A. Lampert, J. Linkhorst, and M. Wessling, “Biocompatible micron-scale silk fibers fabricated by microfluidic wet spinning”, *Advanced Healthcare Materials* **10**, 2100898 (2021).
- <sup>44</sup>C. Michas, M. Ç. Karakan, P. Nautiyal, J. G. Seidman, C. E. Seidman, A. Agarwal, K. Ekinici, J. Eyckmans, A. E. White, and C. S. Chen, “Engineering a living cardiac pump on a chip using high-precision fabrication”, *Science Advances* **8**, eabm3791 (2022).
- <sup>45</sup>T. Gissibl, S. Thiele, A. Herkommer, and H. Giessen, “Sub-micrometre accurate free-form optics by three-dimensional printing on single-mode fibres”, *Nature Communications* **7**, 11763 (2016).
- <sup>46</sup>J. Li, S. Thiele, R. W. Kirk, B. C. Quirk, A. Hoogendoorn, Y. C. Chen, K. Peter, S. J. Nicholls, J. W. Verjans, P. J. Psaltis, C. Bursill, A. M. Herkommer, H. Giessen, and R. A. McLaughlin, “3D-printed micro lens-in-lens for in vivo multimodal microendoscopy”, *Small* **18**, 2107032 (2022).
- <sup>47</sup>A. Kubec, M.-C. Zdora, U. T. Sanli, A. Diaz, J. Vila-Comamala, and C. David, “An achromatic X-ray lens”, *Nature Communications* **13**, 1305 (2022).
- <sup>48</sup>J. K. Hohmann and G. von Freymann, “Influence of direct laser written 3D topographies on proliferation and differentiation of osteoblast-like cells: Towards improved implant surfaces”, *Advanced Functional Materials* **24**, 6573–6580 (2014).
- <sup>49</sup>J. Jang, J.-y. Kim, Y. C. Kim, S. Kim, N. Chou, S. Lee, Y.-H. Choung, S. Kim, J. Brugger, H. Choi, and J. H. Jang, “A 3D micro scaffold cochlear electrode array for steroid elution”, *Advanced Healthcare Materials* **8**, 1900379 (2019).
- <sup>50</sup>Q. Akolawala, M. Rovituso, H. H. Versteeg, A. M. R. Rondon, and A. Accardo, “Evaluation of proton-induced DNA damage in 3D-engineered glioblastoma microenvironments”, *ACS Applied Materials & Interfaces* **14**, 20778–20789 (2022).

- <sup>51</sup>A. D. Lantada, S. Hengsbach, and K. Bade, “Lotus-on-chip: Computer-aided design and 3D direct laser writing of bioinspired surfaces for controlling the wettability of materials and devices”, *Bioinspiration & Biomimetics* **12**, 066004 (2017).
- <sup>52</sup>H. Yu, Q. Zhang, and M. Gu, “Three-dimensional direct laser writing of biomimetic neuron structures”, *Optics Express* **26**, 32111–32117 (2018).
- <sup>53</sup>Y. Wang, Z. Li, M. Elhebeary, R. Hensel, E. Arzt, and M. T. A. Saif, “Water as a “glue”: Elasticity-enhanced wet attachment of biomimetic microcup structures”, *Science Advances* **8**, eabm9341 (2022).
- <sup>54</sup>D. Serien and K. Sugioka, “Fabrication of three-dimensional proteinaceous micro- and nano-structures by femtosecond laser cross-linking”, *Opto-Electronic Advances* **1**, 180008–1 (2018).
- <sup>55</sup>O. Kufelt, A. El-Tamer, C. Sehring, S. Schlie-Wolter, and B. N. Chichkov, “Hyaluronic acid based materials for scaffolding via two-photon polymerization”, *Biomacromolecules* **15**, 650–659 (2014).
- <sup>56</sup>A. Berg, R. Wyrwa, J. Weisser, T. Weiss, R. Schade, G. Hildebrand, K. Liefeth, B. Schneider, R. Ellinger, and M. Schnabelrauch, “Synthesis of photopolymerizable hydrophilic macromers and evaluation of their applicability as reactive resin components for the fabrication of three-dimensionally structured hydrogel matrices by 2-photon-polymerization”, *Advanced Engineering Materials* **13**, B274–B284 (2011).
- <sup>57</sup>C. Loebel, N. Broguiere, M. Alini, M. Zenobi-Wong, and D. Eglin, “Microfabrication of photo-cross-linked hyaluronan hydrogels by single- and two-photon tyramine oxidation”, *Biomacromolecules* **16**, 2624–2630 (2015).
- <sup>58</sup>O. Kufelt, A. El-Tamer, C. Sehring, M. Meißner, S. Schlie-Wolter, and B. N. Chichkov, “Water-soluble photopolymerizable chitosan hydrogels for biofabrication via two-photon polymerization”, *Acta Biomaterialia*, 186–195 (2015).
- <sup>59</sup>W. A. Green, *Industrial photoinitiators: A technical guide* (CRC Press, Boca Raton, FL, USA, 2010).
- <sup>60</sup>J. D. Joannopoulos, S. G. Johnson, J. N. Winn, and R. D. Meade, *Photonic crystals: Molding the flow of light* (Princeton University Press, Princeton, NJ, USA, 2011).
- <sup>61</sup>C. Kittel, *Introduction to solid state physics* (John Wiley & Sons, New York, USA, 1996).
- <sup>62</sup>I. A. Sukhoivanov and I. V. Guryev, *Photonic crystals: physics and practical modeling* (Springer, Heidelberg, Germany, 2009).
- <sup>63</sup>J.-M. Lourtioz, H. Benisty, V. Berger, J.-M. Gérard, D. Maystre, and A. Tchernokov, *Photonic crystals* (Springer, Heidelberg, Germany, 2005).
- <sup>64</sup>S. Noda, K. Tomoda, N. Yamamoto, and A. Chutinan, “Full three-dimensional photonic bandgap crystals at near-infrared wavelengths”, *Science* **289**, 604–606 (2000).

- <sup>65</sup>S. Wong, M. Deubel, F. Pérez-Willard, S. John, G. A. Ozin, M. Wegener, and G. von Freymann, “Direct laser writing of three-dimensional photonic crystals with a complete photonic bandgap in chalcogenide glasses”, *Advanced Materials* **18**, 265–269 (2006).
- <sup>66</sup>A. Bouzidi, D. Bria, A. Akjouj, Y. Pennec, and B. Djafari-Rouhani, “A tiny gas-sensor system based on 1D photonic crystal”, *Journal of Physics D: Applied Physics* **48**, 495102 (2015).
- <sup>67</sup>A. K. Goyal, H. S. Dutta, and S. Pal, “Recent advances and progress in photonic crystal-based gas sensors”, *Journal of Physics D: Applied Physics* **50**, 203001 (2017).
- <sup>68</sup>C. Jamois, R. B. Wehrspohn, L. C. Andreani, C. Hermann, O. Hess, and U. Gösele, “Silicon-based two-dimensional photonic crystal waveguides”, *Photonics and Nanostructures—Fundamentals and Applications* **1**, 1–13 (2003).
- <sup>69</sup>R. M. De La Rue and C. Seassal, “Photonic crystal devices: Some basics and selected topics”, *Laser & Photonics Reviews* **6**, 564–597 (2012).
- <sup>70</sup>D. S. Wiersma, “Disordered photonics”, *Nature Photonics* **7**, 188–196 (2013).
- <sup>71</sup>J. M. Schmitt and G. Kumar, “Turbulent nature of refractive-index variations in biological tissue”, *Optics Letters* **21**, 1310–1312 (1996).
- <sup>72</sup>A. Webb, *Introduction to biomedical imaging* (John Wiley & Sons, Hoboken, NJ, USA, 2022).
- <sup>73</sup>W. Rudolph and M. Kempe, “Trends in optical biomedical imaging”, *Journal of Modern Optics* **44**, 1617–1642 (1997).
- <sup>74</sup>C. Das, A. Trivedi, K. Mitra, and T. Vo-Dinh, “Short pulse laser propagation through tissues for biomedical imaging”, *Journal of Physics D: Applied Physics* **36**, 1714 (2003).
- <sup>75</sup>C. Elachi and J. J. Van Zyl, *Introduction to the physics and techniques of remote sensing* (John Wiley & Sons, Hoboken, NJ, USA, 2021).
- <sup>76</sup>G. L. Prost, *Remote sensing for geoscientists: Image analysis and integration* (CRC Press, Boca Raton, FL, USA, 2013).
- <sup>77</sup>V. Ossenkopf, “Effective-medium theories for cosmic dust grains”, *Astronomy and Astrophysics* **251**, 210–219 (1991).
- <sup>78</sup>W. Yang, B. Matsushita, J. Chen, K. Yoshimura, and T. Fukushima, “Retrieval of inherent optical properties for turbid inland waters from remote-sensing reflectance”, *IEEE Transactions on Geoscience and Remote Sensing* **51**, 3761–3773 (2012).
- <sup>79</sup>N. M. Lawandy, R. M. Balachandran, A. S. L. Gomes, and E. Sauvain, “Laser action in strongly scattering media”, *Nature* **368**, 436–438 (1994).



- 
- <sup>80</sup>D. S. Wiersma, “The physics and applications of random lasers”, *Nature Physics* **4**, 359–367 (2008).
- <sup>81</sup>Y. Lu, Z. Chen, L. Ai, X. Zhang, J. Zhang, J. Li, W. Wang, R. Tan, N. Dai, and W. Song, “A universal route to realize radiative cooling and light management in photovoltaic modules”, *Solar RRL* **1**, 1700084 (2017).
- <sup>82</sup>R. Y. M. Wong, C. Y. Tso, S. C. Fu, and C. Y. H. Chao, “Maxwell-Garnett permittivity optimized micro-porous PVDF/PMMA blend for near unity thermal emission through the atmospheric window”, *Solar Energy Materials and Solar Cells* **248**, 112003 (2022).
- <sup>83</sup>G. Shang, M. Eich, and A. Petrov, “Photonic glass based structural color”, *APL Photonics* **5**, 060901 (2020).
- <sup>84</sup>F. Sterl, E. Herkert, S. Both, T. Weiss, and H. Giessen, “Shaping the color and angular appearance of plasmonic metasurfaces with tailored disorder”, *ACS Nano* **15**, 10318–10327 (2021).
- <sup>85</sup>E. Herkert, F. Sterl, S. Both, S. G. Tikhodeev, T. Weiss, and H. Giessen, “Influence of structural disorder on plasmonic metasurfaces and their colors—A coupled point dipole approach: Tutorial”, *Journal of the Optical Society of America B* **40**, B59–B99 (2023).
- <sup>86</sup>G. Jacucci, J. Bertolotti, and S. Vignolini, “Role of anisotropy and refractive index in scattering and whiteness optimization”, *Advanced Optical Materials* **7**, 1900980 (2019).
- <sup>87</sup>J. Syurik, R. H. Siddique, A. Dollmann, G. Gomard, M. Schneider, M. Worgull, G. Wiegand, and H. Hölscher, “Bio-inspired, large scale, highly-scattering films for nanoparticle-alternative white surfaces”, *Scientific Reports* **7**, 46637 (2017).
- <sup>88</sup>L. M. Borgmann, S. Johnsen, C. Santos de Oliveira, J. Martins de Souza e Silva, J. Li, C. Kirchlechner, G. Gomard, G. Wiegand, and H. Hölscher, “Porous polymeric microparticles foamed with supercritical CO<sub>2</sub> as scattering white pigments”, *Bioinspiration & Biomimetics* **18**, 026011 (2023).
- <sup>89</sup>J. Yip, S.-P. Ng, and K. H. Wong, “Brilliant whiteness surfaces from electrospun nanofiber webs”, *Textile Research Journal* **79**, 771–779 (2009).
- <sup>90</sup>F. Zeighami and M. A. Tehran, “Developing optically efficient nanofiber coatings inspired by *Cyphochilus* white beetle”, *Journal of Industrial Textiles* **46**, 495–509 (2016).
- <sup>91</sup>B. K. Park, S. M. Han, and S. E. Han, “Surpassing *Cyphochilus* scales in optical scattering strength by well-controlled electrospun nanostructures”, *Optical Materials Express* **12**, 2529–2540 (2022).
- <sup>92</sup>J. Syurik, G. Jacucci, O. D. Onelli, H. Hölscher, and S. Vignolini, “Bio-inspired highly scattering networks via polymer phase separation”, *Advanced Functional Materials* **28**, 1706901 (2018).

- <sup>93</sup>W. Zou, L. Pattelli, J. Guo, S. Yang, M. Yang, N. Zhao, J. Xu, and D. S. Wiersma, “Biomimetic polymer film with brilliant brightness using a one-step water vapor-induced phase separation method”, *Advanced Functional Materials* **29**, 1808885 (2019).
- <sup>94</sup>B. Yu, Z. Huang, D. Fang, S. Yu, T. Fu, Y. Tang, and Z. Li, “Biomimetic porous fluoropolymer films with brilliant whiteness by using polymerization-induced phase separation”, *Advanced Materials Interfaces* **9**, 2101485 (2022).
- <sup>95</sup>D. T. Meiers, “Entwicklung und Analyse eines grundlegenden Modells weißer Käferschuppen”, Diploma thesis (Technische Universität Kaiserslautern, 2018).
- <sup>96</sup>H. L. Leertouwer, B. D. Wilts, and D. G. Stavenga, “Refractive index and dispersion of butterfly chitin and bird keratin measured by polarizing interference microscopy”, *Optics Express* **19**, 24061–24066 (2011).
- <sup>97</sup>B. T. Hallam, A. G. Hiorns, and P. Vukusic, “Developing optical efficiency through optimized coating structure: Biomimetic inspiration from white beetles”, *Applied Optics* **48**, 3243–3249 (2009).
- <sup>98</sup>L. E. McNeil and R. H. French, “Multiple scattering from rutile TiO<sub>2</sub> particles”, *Acta Materialia* **48**, 4571–4576 (2000).
- <sup>99</sup>M. F. Land, “The physics and biology of animal reflectors”, *Progress in Biophysics and Molecular Biology* **24**, 75–106 (1972).
- <sup>100</sup>A. R. Parker, D. R. McKenzie, and M. C. J. Large, “Multilayer reflectors in animals using green and gold beetles as contrasting examples”, *The Journal of Experimental Biology* **201**, 1307–1313 (1998).
- <sup>101</sup>J. A. Bossard, L. Lin, and D. H. Werner, “Evolving random fractal Cantor superlattices for the infrared using a genetic algorithm”, *Journal of the Royal Society Interface* **13**, 20150975 (2016).
- <sup>102</sup>A. Ishimaru, *Wave propagation and scattering in random media*, Vol. 2 (Academic Press, New York, USA, 1978).
- <sup>103</sup>L. Tsang, J. A. Kong, and R. T. Shin, *Theory of microwave remote sensing* (John Wiley & Sons, New York, USA, 1985).
- <sup>104</sup>L. Tsang, J. A. Kong, and K.-H. Ding, *Scattering of electromagnetic waves: Theories and applications* (John Wiley & Sons, New York, USA, 2004).
- <sup>105</sup>A. Ishimaru, “Theory and application of wave propagation and scattering in random media”, *Proceedings of the IEEE* **65**, 1030–1061 (1977).
- <sup>106</sup>A. Ishimaru, “Diffusion of light in turbid material”, *Applied Optics* **28**, 2210–2215 (1989).
- <sup>107</sup>Q. H. Liu, “The pseudospectral time-domain (PSTD) method: A new algorithm for solutions of Maxwell’s equations”, in *IEEE Antennas and Propagation Society International Symposium 1997. Digest*, Vol. 1 (IEEE, 1997), pp. 122–125.

- 
- <sup>108</sup>Q. H. Liu, “Large-scale simulations of electromagnetic and acoustic measurements using the pseudospectral time-domain (PSTD) algorithm”, *IEEE Transactions on Geoscience and Remote Sensing* **37**, 917–926 (1999).
- <sup>109</sup>M. I. Mishchenko, L. D. Travis, and D. W. Mackowski, “T-matrix computations of light scattering by nonspherical particles: A review”, *Journal of Quantitative Spectroscopy and Radiative Transfer* **55**, 535–575 (1996).
- <sup>110</sup>D. Theobald, D. Beutel, L. Borgmann, H. Mescher, G. Gomard, C. Rockstuhl, and U. Lemmer, “Simulation of light scattering in large, disordered nanostructures using a periodic T-matrix method”, *Journal of Quantitative Spectroscopy and Radiative Transfer* **272**, 107802 (2021).
- <sup>111</sup>K. S. Yee and J. S. Chen, “The finite-difference time-domain (FDTD) and the finite-volume time-domain (FVTD) methods in solving Maxwell’s equations”, *IEEE Transactions on Antennas and Propagation* **45**, 354–363 (1997).
- <sup>112</sup>P. Hank, F. Foschum, S. Geiger, and A. Kienle, “Efficient electrical field Monte Carlo simulation of coherent backscattering”, *Journal of Quantitative Spectroscopy and Radiative Transfer* **287**, 108230 (2022).
- <sup>113</sup>R. Schittny, A. Niemeyer, F. Mayer, A. Naber, M. Kadic, and M. Wegener, “Invisibility cloaking in light-scattering media”, *Laser & Photonics Reviews* **10**, 382–408 (2016).
- <sup>114</sup>B. Chen, K. Stamnes, and J. J. Stamnes, “Validity of the diffusion approximation in bio-optical imaging”, *Applied Optics* **40**, 6356–6366 (2001).
- <sup>115</sup>J. R. Lorenzo, *Principles of diffuse light propagation* (World Scientific, Singapore, 2012).
- <sup>116</sup>M. Xu, “Electric field Monte Carlo simulation of polarized light propagation in turbid media”, *Optics Express* **12**, 6530–6539 (2004).
- <sup>117</sup>J. Sawicki, N. Kastor, and M. Xu, “Electric field Monte Carlo simulation of coherent backscattering of polarized light by a turbid medium containing Mie scatterers”, *Optics Express* **16**, 5728–5738 (2008).
- <sup>118</sup>M. B. van der Mark, M. P. van Albada, and A. Lagendijk, “Light scattering in strongly scattering media: multiple scattering and weak localization”, *Physical Review B* **37**, 3575 (1988).
- <sup>119</sup>W.-F. Cheong, S. A. Prahl, and A. J. Welch, “A review of the optical properties of biological tissues”, *IEEE Journal of Quantum Electronics* **26**, 2166–2185 (1990).
- <sup>120</sup>L. G. Henyey and J. L. Greenstein, “Diffuse radiation in the galaxy”, *Astrophysical Journal* **93**, 70–83 (1941).
- <sup>121</sup>M. P. van Albada, B. A. van Tiggelen, A. Lagendijk, and A. Tip, “Speed of propagation of classical waves in strongly scattering media”, *Physical Review Letters* **66**, 3132 (1991).

- <sup>122</sup>C. M. Soukoulis, S. Datta, and E. N. Economou, “Propagation of classical waves in random media”, *Physical Review B* **49**, 3800 (1994).
- <sup>123</sup>M. Rothhammer, C. Zollfrank, K. Busch, and G. von Freymann, “Tailored disorder in photonics: Learning from nature”, *Advanced Optical Materials* **9**, 2100787 (2021).
- <sup>124</sup>D. J. Durian, “Influence of boundary reflection and refraction on diffusive photon transport”, *Physical Review E* **50**, 857 (1994).
- <sup>125</sup>J. X. Zhu, D. J. Pine, and D. A. Weitz, “Internal reflection of diffusive light in random media”, *Physical Review A* **44**, 3948 (1991).
- <sup>126</sup>S. E. Han, S. Atiganyanun, S. H. Lee, S. Cheek, and S. M. Han, “Determination of internal reflectance for photonic glasses”, *Physical Review B* **99**, 054206 (2019).
- <sup>127</sup>E. Alerstam, “Anisotropic diffusive transport: Connecting microscopic scattering and macroscopic transport properties”, *Physical Review E* **89**, 063202 (2014).
- <sup>128</sup>S. E. Han, “Transport mean free path tensor and anisotropy tensor in anisotropic diffusion equation for optical media”, *Journal of Optics* **22**, 075606 (2020).
- <sup>129</sup>E. Abrahams, P. W. Anderson, D. C. Licciardello, and T. V. Ramakrishnan, “Scaling theory of localization: Absence of quantum diffusion in two dimensions”, *Physical Review Letters* **42**, 673 (1979).
- <sup>130</sup>D. E. Khmel’nitskii, “Localization and coherent scattering of electrons”, *Physica B+C* **126**, 235–241 (1984).
- <sup>131</sup>R. Sapienza, S. Mujumdar, C. Cheung, A. G. Yodh, and D. Wiersma, “Anisotropic weak localization of light”, *Physical Review Letters* **92**, 033903 (2004).
- <sup>132</sup>M. Kaveh, M. Rosenbluh, I. Edrei, and I. Freund, “Weak localization and light scattering from disordered solids”, *Physical Review Letters* **57**, 2049 (1986).
- <sup>133</sup>P. W. Anderson, “Absence of diffusion in certain random lattices”, *Physical Review* **109**, 1492 (1958).
- <sup>134</sup>A. Lagendijk, B. van Tiggelen, and D. S. Wiersma, “Fifty years of Anderson localization”, *Physics Today* **62**, 24–29 (2009).
- <sup>135</sup>D. S. Wiersma, P. Bartolini, A. Lagendijk, and R. Righini, “Localization of light in a disordered medium”, *Nature* **390**, 671–673 (1997).
- <sup>136</sup>M. Störzer, P. Gross, C. M. Aegerter, and G. Maret, “Observation of the critical regime near Anderson localization of light”, *Physical Review Letters* **96**, 063904 (2006).
- <sup>137</sup>T. Sperling, W. Buehrer, C. M. Aegerter, and G. Maret, “Direct determination of the transition to localization of light in three dimensions”, *Nature Photonics* **7**, 48–52 (2013).
- <sup>138</sup>F. Scheffold, R. Lenke, R. Tweer, and G. Maret, “Localization or classical diffusion of light?”, *Nature* **398**, 206–207 (1999).

- 
- <sup>139</sup>T. Sperling, L. Schertel, M. Ackermann, G. J. Aubry, C. M. Aegerter, and G. Maret, “Can 3D light localization be reached in ‘white paint’?”, *New Journal of Physics* **18**, 013039 (2016).
- <sup>140</sup>T. Schwartz, G. Bartal, S. Fishman, and M. Segev, “Transport and Anderson localization in disordered two-dimensional photonic lattices”, *Nature* **446**, 52–55 (2007).
- <sup>141</sup>M. Segev, Y. Silberberg, and D. N. Christodoulides, “Anderson localization of light”, *Nature Photonics* **7**, 197–204 (2013).
- <sup>142</sup>A. Mafi, “Transverse Anderson localization of light: A tutorial”, *Advances in Optics and Photonics* **7**, 459–515 (2015).
- <sup>143</sup>U. K. Chettiar and N. Engheta, “Internal homogenization: Effective permittivity of a coated sphere”, *Optics Express* **20**, 22976–22986 (2012).
- <sup>144</sup>C. Brosseau, “Modelling and simulation of dielectric heterostructures: A physical survey from an historical perspective”, *Journal of Physics D: Applied Physics* **39**, 1277 (2006).
- <sup>145</sup>L. Schwartz, F. Brouers, A. V. Vedyayev, and H. Ehrenreich, “Comparison of the average-T-Matrix and coherent-potential approximations in substitutional alloys”, *Physical Review B* **4**, 3383 (1971).
- <sup>146</sup>D. Stroud, “Generalized effective-medium approach to the conductivity of an inhomogeneous material”, *Physical Review B* **12**, 3368 (1975).
- <sup>147</sup>J. Koringa, “Dispersion theory for electrons in a random lattice with applications to the electronic structure of alloys”, *Journal of Physics and Chemistry of Solids* **7**, 252–258 (1958).
- <sup>148</sup>J. L. Beeby, “Electronic structure of alloys”, *Physical Review* **135**, A130 (1964).
- <sup>149</sup>N. C. Kothari, “Effective-medium theory of a nonlinear composite medium using the T-matrix approach: Exact results for spherical grains”, *Physical Review A* **41**, 4486 (1990).
- <sup>150</sup>J. C. M. Garnett, “XII. Colours in metal glasses and in metallic films”, *Philosophical Transaction of the Royal Society A* **203**, 385–420 (1904).
- <sup>151</sup>P. Soven, “Coherent-potential model of substitutional disordered alloys”, *Physical Review* **156**, 809 (1967).
- <sup>152</sup>G. W. Milton, “The coherent potential approximation is a realizable effective medium scheme”, *Communications in Mathematical Physics* **99**, 463–500 (1985).
- <sup>153</sup>D. A. G. Bruggeman, “Berechnung verschiedener physikalischer Konstanten von heterogenen Substanzen. I. Dielektrizitätskonstanten und Leitfähigkeiten der Mischkörper aus isotropen Substanzen”, *Annalen der Physik* **416**, 636–664 (1935).
- <sup>154</sup>K. N. Rozanov, M. Y. Koledintseva, and J. L. Drewniak, “A mixing rule for predicting frequency dependence of material parameters in magnetic composites”, *Journal of Magnetism and Magnetic Materials* **324**, 1063–1066 (2012).

- <sup>155</sup>P. Mallet, C.-A. Guérin, and A. Sentenac, “Maxwell-Garnett mixing rule in the presence of multiple scattering: Derivation and accuracy”, *Physical Review B* **72**, 014205 (2005).
- <sup>156</sup>B. Abeles and J. I. Gittleman, “Composite material films: Optical properties and applications”, *Applied Optics* **15**, 2328–2332 (1976).
- <sup>157</sup>A. Spanoudaki and R. Pelster, “Effective dielectric properties of composite materials: The dependence on the particle size distribution”, *Physical Review B* **64**, 064205 (2001).
- <sup>158</sup>C. F. Bohren, “Applicability of effective-medium theories to problems of scattering and absorption by nonhomogeneous atmospheric particles”, *Journal of the Atmospheric Sciences* **43**, 468–475 (1986).
- <sup>159</sup>G. W. Milton, *The theory of composites* (Society for Industrial and Applied Mathematics (SIAM), Philadelphia, PA, USA, 2022).
- <sup>160</sup>A. H. Sihvola, “Self-consistency aspects of dielectric mixing theories”, *IEEE Transactions on Geoscience and Remote Sensing* **27**, 403–415 (1989).
- <sup>161</sup>C. F. Bohren and L. J. Battan, “Radar backscattering of microwaves by spongy ice spheres”, *Journal of Atmospheric Sciences* **39**, 2623–2628 (1982).
- <sup>162</sup>J. D. Jackson, *Classical Electrodynamics* (John Wiley & Sons, New York, USA, 1962).
- <sup>163</sup>V. A. Markel, “Introduction to the Maxwell Garnett approximation: Tutorial”, *Journal of the Optical Society of America A* **33**, 1244–1256 (2016).
- <sup>164</sup>W. T. Doyle, “Optical properties of a suspension of metal spheres”, *Physical Review B* **39**, 9852 (1989).
- <sup>165</sup>A. Lakhtakia, “Size-dependent Maxwell-Garnett formula from an integral equation formalism”, *Optik (Stuttgart)* **91**, 134–137 (1992).
- <sup>166</sup>C. A. Foss Jr., G. L. Hornyak, J. A. Stockert, and C. R. Martin, “Template-synthesized nanoscopic gold particles: Optical spectra and the effects of particle size and shape”, *The Journal of Physical Chemistry* **98**, 2963–2971 (1994).
- <sup>167</sup>H. Looyenga, “Dielectric constants of heterogeneous mixtures”, *Physica* **31**, 401–406 (1965).
- <sup>168</sup>G. A. Niklasson, C. G. Granqvist, and O. Hunderi, “Effective medium models for the optical properties of inhomogeneous materials”, *Applied Optics* **20**, 26–30 (1981).
- <sup>169</sup>G. Banhegyi, “Comparison of electrical mixture rules for composites”, *Colloid and Polymer Science* **264**, 1030–1050 (1986).
- <sup>170</sup>K. Yee, “Numerical solution of initial boundary value problems involving Maxwell’s equations in isotropic media”, *IEEE Transactions on Antennas and Propagation* **14**, 302–307 (1966).

- 
- <sup>171</sup>A. Taflove and M. E. Brodwin, “Numerical solution of steady-state electromagnetic scattering problems using the time-dependent Maxwell’s equations”, *IEEE Transactions on Microwave Theory and Techniques* **23**, 623–630 (1975).
- <sup>172</sup>D. Wilton and R. Mittra, “A new numerical approach to the calculation of electromagnetic scattering properties of two-dimensional bodies of arbitrary cross section”, *IEEE Transactions on Antennas and Propagation* **20**, 310–317 (1972).
- <sup>173</sup>B. H. McDonald and A. Wexler, “Finite-element solution of unbounded field problems”, *IEEE Transactions on Microwave Theory and Techniques* **20**, 841–847 (1972).
- <sup>174</sup>T. K. Wu and L. L. Tsai, “Numerical analysis of electromagnetic fields in biological issues”, *Proceedings of the IEEE* **62**, 1167–1168 (1974).
- <sup>175</sup>A. Taflove, S. C. Hagness, and M. Picket-May, “Computational electromagnetics: The finite-difference time-domain method”, in *The electrical engineering handbook*, edited by W.-K. Chen (Elsevier, Amsterdam, The Netherlands, 2005), pp. 629–670.
- <sup>176</sup>W. Yu and R. Mittra, “A conformal finite difference time domain technique for modeling curved dielectric surfaces”, *IEEE Microwave and Wireless Components Letters* **11**, 25–27 (2001).
- <sup>177</sup>D. E. Merewether, “Transient currents induced on a metallic body of revolution by an electromagnetic pulse”, *IEEE Transactions on Electromagnetic Compatibility*, 41–44 (1971).
- <sup>178</sup>G. Mur, “Absorbing boundary conditions for the finite-difference approximation of the time-domain electromagnetic-field equations”, *IEEE Transactions on Electromagnetic Compatibility*, 377–382 (1981).
- <sup>179</sup>R. Holland and J. W. Williams, “Total-field versus scattered-field finite-difference codes: A comparative assessment”, *IEEE Transactions on Nuclear Science* **30**, 4583–4588 (1983).
- <sup>180</sup>J.-P. Berenger, “A perfectly matched layer for the absorption of electromagnetic waves”, *Journal of Computational Physics* **114**, 185–200 (1994).
- <sup>181</sup>S. D. Gedney, “An anisotropic perfectly matched layer-absorbing medium for the truncation of FDTD lattices”, *IEEE Transactions on Antennas and Propagation* **44**, 1630–1639 (1996).
- <sup>182</sup>R. Y. Rubinstein and D. P. Kroese, *Simulation and the Monte Carlo method* (John Wiley & Sons, Hoboken, NJ, USA, 2016).
- <sup>183</sup>M. Dobbs and J. B. Hansen, “The HepMC C++ Monte Carlo event record for high energy physics”, *Computer Physics Communications* **134**, 41–46 (2001).
- <sup>184</sup>I. Lux, *Monte Carlo particle transport methods* (CRC Press, Boca Raton, FL, USA, 2018).

- <sup>185</sup>L. Wang, S. L. Jacques, and L. Zheng, “MCML—Monte Carlo modeling of light transport in multi-layered tissues”, *Computer Methods and Programs in Biomedicine* **47**, 131–146 (1995).
- <sup>186</sup>Q. Fang and D. A. Boas, “Monte Carlo simulation of photon migration in 3D turbid media accelerated by graphics processing units”, *Optics Express* **17**, 20178–20190 (2009).
- <sup>187</sup>P. Glasserman, *Monte Carlo methods in financial engineering* (Springer, Heidelberg, Germany, 2004).
- <sup>188</sup>A. H. Hielscher, R. E. Alcouffe, and R. L. Barbour, “Comparison of finite-difference transport and diffusion calculations for photon migration in homogeneous and heterogeneous tissues”, *Physics in Medicine & Biology* **43**, 1285 (1998).
- <sup>189</sup>B. C. Wilson and G. Adam, “A Monte Carlo model for the absorption and flux distributions of light in tissue”, *Medical Physics* **10**, 824–830 (1983).
- <sup>190</sup>S. A. Prahl, “A Monte Carlo model of light propagation in tissue”, in *Dosimetry of laser radiation in medicine and biology*, Vol. 10305 (SPIE, 1989), pp. 105–114.
- <sup>191</sup>D. A. Boas, J. P. Culver, J. J. Stott, and A. K. Dunn, “Three dimensional Monte Carlo code for photon migration through complex heterogeneous media including the adult human head”, *Optics Express* **10**, 159–170 (2002).
- <sup>192</sup>J. Mościński, M. Bargieł, Z. A. Rycerz, and P. W. M. Jacobs, “The force-biased algorithm for the irregular close packing of equal hard spheres”, *Molecular Simulations* **3**, 201–212 (1989).
- <sup>193</sup>A. Bezrukov, M. Bargieł, and D. Stoyan, “Statistical analysis of simulated random packings of spheres”, *Particle & Particle Systems Characterization* **19**, 111–118 (2002).
- <sup>194</sup>S. Torquato, T. M. Truskett, and P. G. Debenedetti, “Is random close packing of spheres well defined?”, *Physical Review Letters* **84**, 2064 (2000).
- <sup>195</sup>M. Thiel and M. Hermatschweiler, “Three-dimensional laser lithography: A new degree of freedom for science and industry”, *Optik & Photonik* **6**, 36–39 (2011).
- <sup>196</sup>M. Thiel, J. Fischer, G. von Freymann, and M. Wegener, “Direct laser writing of three-dimensional submicron structures using a continuous-wave laser at 532 nm”, *Applied Physics Letters* **97**, 221102 (2010).
- <sup>197</sup>J. Fischer and M. Wegener, “Three-dimensional optical laser lithography beyond the diffraction limit”, *Laser & Photonics Reviews* **7**, 22–44 (2013).
- <sup>198</sup>S. Maruo, O. Nakamura, and S. Kawata, “Three-dimensional microfabrication with two-photon-absorbed photopolymerization”, *Optics Letters* **22**, 132–134 (1997).
- <sup>199</sup>J. B. Mueller, J. Fischer, F. Mayer, M. Kadic, and M. Wegener, “Polymerization kinetics in three-dimensional direct laser writing”, *Advanced Materials* **26**, 6566–6571 (2014).



- 
- <sup>200</sup>E. H. Waller and G. von Freymann, “Spatio-temporal proximity characteristics in 3D  $\mu$ -printing via multi-photon absorption”, *Polymers* **8**, 297 (2016).
- <sup>201</sup>G. de Miguel, G. Vicidomini, B. Harke, and A. Diaspro, “Linewidth and writing resolution”, in *Three-Dimensional Microfabrication Using Two-photon Polymerization* (Elsevier, Amsterdam, The Netherlands, 2016), pp. 190–220.
- <sup>202</sup>C. Jörg, “Interfaces and defects in topological model systems of 3D micro-printed waveguides”, PhD thesis (Technische Universität Kaiserslautern, 2019).
- <sup>203</sup>L. Lepetit, G. Chériaux, and M. Joffe, “Linear techniques of phase measurement by femtosecond spectral interferometry for applications in spectroscopy”, *Journal of the Optical Society of America B* **12**, 2467–2474 (1995).
- <sup>204</sup>R. C. R. Pompe, D. T. Meiers, W. Pfeiffer, and G. von Freymann, “Weak localization enhanced ultrathin scattering media”, *Advanced Optical Materials* **10**, 2200700 (2022).
- <sup>205</sup>V. V. Bassarab, V. A. Shalygin, A. A. Shakhmin, V. S. Sokolov, and G. I. Kropotov, “Spectroscopy of a borosilicate crown glass in the wavelength range of 0.2  $\mu\text{m}$ –15 cm”, *Journal of Optics* **25**, 065401 (2023).
- <sup>206</sup>C. Xu and W. W. Webb, “Measurement of two-photon excitation cross sections of molecular fluorophores with data from 690 to 1050 nm”, *Journal of the Optical Society of America B* **13**, 481–491 (1996).
- <sup>207</sup>D. A. Oulianov, I. V. Tomov, A. S. Dvornikov, and P. M. Rentzepis, “Observations on the measurement of two-photon absorption cross-section”, *Optics Communications* **191**, 235–243 (2001).
- <sup>208</sup>A. Nag and D. Goswami, “Solvent effect on two-photon absorption and fluorescence of rhodamine dyes”, *Journal of Photochemistry and Photobiology A: Chemistry* **206**, 188–197 (2009).
- <sup>209</sup>P. Sengupta, J. Balaji, S. Banerjee, R. Philip, G. R. Kumar, and S. Maiti, “Sensitive measurement of absolute two-photon absorption cross sections”, *The Journal of Chemical Physics* **112**, 9201–9205 (2000).
- <sup>210</sup>M. Sheik-Bahae, A. A. Said, T.-H. Wei, D. J. Hagan, and E. W. van Stryland, “Sensitive measurement of optical nonlinearities using a single beam”, *IEEE Journal of Quantum Electronics* **26**, 760–769 (1990).
- <sup>211</sup>H. J. Eichler and J. Eichler, *Laser: Bauformen, Strahlführung, Anwendungen* (Springer, Heidelberg, Germany, 2015).
- <sup>212</sup>P. Laures, “Geometrical approach to Gaussian beam propagation”, *Applied Optics* **6**, 747–755 (1967).
- <sup>213</sup>G. Tsigaridas, M. Fakis, I. Polyzos, M. Tsibouri, P. Persephonis, and V. Giannetas, “Z-scan analysis for near-Gaussian beams through Hermite–Gaussian decomposition”, *Journal of the Optical Society of America B* **20**, 670–676 (2003).

- <sup>214</sup>G. Boudebs, V. Besse, C. Cassagne, H. Leblond, and C. B. de Araújo, “Nonlinear characterization of materials using the  $D4\sigma$  method inside a  $z$ -scan  $4f$ -system”, *Optics Letters* **38**, 2206–2208 (2013).
- <sup>215</sup>C. A. Grimes and D. M. Grimes, “Permeability and permittivity spectra of granular materials”, *Physical Review B* **43**, 10780 (1991).
- <sup>216</sup>P. Yazhgur, G. J. Aubry, L. S. Froufe-Pérez, and F. Scheffold, “Light scattering from colloidal aggregates on a hierarchy of length scales”, *Optics Express* **29**, 14367–14383 (2021).
- <sup>217</sup>P. Yazhgur, G. J. Aubry, L. S. Froufe-Pérez, and F. Scheffold, “Scattering phase delay and momentum transfer of light in disordered media”, *Physical Review Research* **4**, 023235 (2022).
- <sup>218</sup>H. J. Cha, J. Hedrick, R. A. DiPietro, T. Blume, R. Beyers, and D. Y. Yoon, “Structures and dielectric properties of thin polyimide films with nano-foam morphology”, *Applied Physics Letters* **68**, 1930–1932 (1996).
- <sup>219</sup>M. D. Anguelova, “Complex dielectric constant of sea foam at microwave frequencies”, *Journal of Geophysical Research: Oceans* **113** (2008).
- <sup>220</sup>D. Stroud and F. P. Pan, “Self-consistent approach to electromagnetic wave propagation in composite media: Application to model granular metals”, *Physical Review B* **17**, 1602 (1978).
- <sup>221</sup>S. Torquato and J. Kim, “Nonlocal effective electromagnetic wave characteristics of composite media: Beyond the quasistatic regime”, *Physical Review X* **11**, 021002 (2021).
- <sup>222</sup>H. Yu, D. Liu, Y. Duan, and Z. Yang, “Applicability of the effective medium theory for optimizing thermal radiative properties of systems containing wavelength-sized particles”, *International Journal of Heat and Mass Transfer* **87**, 303–311 (2015).
- <sup>223</sup>K. K. Karkkainen, A. H. Sihvola, and K. I. Nikoskinen, “Effective permittivity of mixtures: numerical validation by the FDTD method”, *IEEE Transactions on Geoscience and Remote Sensing* **38**, 1303–1308 (2000).
- <sup>224</sup>E. Lidorikis, S. Egusa, and J. D. Joannopoulos, “Effective medium properties and photonic crystal superstructures of metallic nanoparticle arrays”, *Journal of Applied Physics* **101**, 054304 (2007).
- <sup>225</sup>D. T. Meiers and G. von Freymann, “Mixing rule for calculating the effective refractive index beyond the limit of small particles”, *Optics Express* **31**, 32067–32081 (2023).
- <sup>226</sup>C. F. Bohren and D. P. Gilra, “Extinction by a spherical particle in an absorbing medium”, *Journal of Colloid and Interface Science* **72**, 215–221 (1979).
- <sup>227</sup>P. Chýlek and V. Srivastava, “Dielectric constant of a composite inhomogeneous medium”, *Physical Review B* **27**, 5098 (1983).

- 
- <sup>228</sup>C. F. Bohren and D. R. Huffman, *Absorption and scattering of light by small particles* (John Wiley & Sons, New York, USA, 1983).
- <sup>229</sup>C. R. Simovski, “On electromagnetic characterization and homogenization of nanostructured metamaterials”, *Journal of Optics* **13**, 013001 (2010).
- <sup>230</sup>W. Śmigaj and B. Gralak, “Validity of the effective-medium approximation of photonic crystals”, *Physical Review B* **77**, 235445 (2008).
- <sup>231</sup>D. R. Smith, S. Schultz, P. Markoš, and C. M. Soukoulis, “Determination of effective permittivity and permeability of metamaterials from reflection and transmission coefficients”, *Physical Review B* **65**, 195104 (2002).
- <sup>232</sup>S. O’Brien and J. B. Pendry, “Photonic band-gap effects and magnetic activity in dielectric composites”, *Journal of Physics: Condensed Matter* **14**, 4035 (2002).
- <sup>233</sup>G. Jacucci, L. Schertel, Y. Zhang, H. Yang, and S. Vignolini, “Light management with natural materials: From whiteness to transparency”, *Advanced Materials* **33**, 2001215 (2021).
- <sup>234</sup>T. Gric, S. G. Sokolovski, N. Navolokin, O. Semyachkina-Glushkovskaya, and E. U. Rafailov, “Metamaterial formalism approach for advancing the recognition of glioma areas in brain tissue biopsies”, *Optical Materials Express* **10**, 1607–1615 (2020).
- <sup>235</sup>T. Gric and E. Rafailov, “On the effective medium theory to study the dielectric response of the cancerous biological tissue”, in *Quantum Sensing and Nano Electronics and Photonics XVIII*, Vol. 12009 (SPIE, 2022), pp. 126–129.
- <sup>236</sup>N. A. Campbell, B. Williamson, and R. J. Heyden, *Biology: Exploring life* (Pearson Prentice Hall, Boston, USA, 2006).
- <sup>237</sup>Q. Cassar, S. Caravera, G. MacGrogan, T. Bücher, P. Hillger, U. Pfeiffer, T. Zimmer, J.-P. Guillet, and P. Mounaix, “Terahertz refractive index-based morphological dilation for breast carcinoma delineation”, *Scientific Reports* **11**, 6457 (2021).
- <sup>238</sup>M. Schmid, D. Ludescher, and H. Giessen, “Optical properties of photoresists for femtosecond 3D printing: Refractive index, extinction, luminescence-dose dependence, aging, heat treatment and comparison between 1-photon and 2-photon exposure”, *Optical Materials Express* **9**, 4564–4577 (2019).
- <sup>239</sup>W. Mecklenbräuker and F. Hlawatsch, *The Wigner distribution: Theory and applications in signal processing* (Elsevier, Amsterdam, The Netherlands, 1997).
- <sup>240</sup>K. M. M. Prabhu, *Window functions and their applications in signal processing* (CRC Press, Boca Raton, FL, USA, 2014).
- <sup>241</sup>F. A. Pinheiro, “Statistics of quality factors in three-dimensional disordered magneto-optical systems and its applications to random lasers”, *Physical Review A* **78**, 023812 (2008).

- <sup>242</sup>M. Mascheck, S. Schmidt, M. Silies, T. Yatsui, K. Kitamura, M. Ohtsu, D. Leipold, E. Runge, and C. Lienau, “Observing the localization of light in space and time by ultrafast second-harmonic microscopy”, *Nature Photonics* **6**, 293–298 (2012).
- <sup>243</sup>H. Cao, J. Y. Xu, D. Z. Zhang, S.-H. Chang, S. T. Ho, E. W. Seelig, X. Liu, and R. P. H. Chang, “Spatial confinement of laser light in active random media”, *Physical Review Letters* **84**, 5584 (2000).
- <sup>244</sup>S. Derakhshanfar, R. Mbeleck, K. Xu, X. Zhang, W. Zhong, and M. Xing, “3D bio-printing for biomedical devices and tissue engineering: A review of recent trends and advances”, *Bioactive Materials* **3**, 144–156 (2018).
- <sup>245</sup>M. Rothhammer, P. Strobel, C. Zollfrank, and C. Urmann, “Biocompatible coatings based on photo-crosslinkable cellulose derivatives”, *International Journal of Biological Macromolecules*, 126063 (2023).
- <sup>246</sup>J. Torgersen, X.-H. Qin, Z. Li, A. Ovsianikov, R. Liska, and J. Stampfl, “Hydrogels for two-photon polymerization: A toolbox for mimicking the extracellular matrix”, *Advanced Functional Materials* **23**, 4542–4554 (2013).
- <sup>247</sup>S. You, J. Li, W. Zhu, C. Yu, D. Mei, and S. Chen, “Nanoscale 3D printing of hydrogels for cellular tissue engineering”, *Journal of Materials Chemistry B* **6**, 2187–2197 (2018).
- <sup>248</sup>D. T. Meiers, M. Rothhammer, M. Maier, C. Zollfrank, and G. von Freymann, “Utilizing the sensitization effect for direct laser writing in a novel photoresist based on the chitin monomer N-acetyl-D-glucosamine”, *Advanced Engineering Materials* **25**, 2201688 (2023).
- <sup>249</sup>C. Y. She, N. D. Dinh, and A. T. Tu, “Laser raman scattering of glucosamine N-acetylglucosamine, and glucuronic acid”, *Biochimica et Biophysica Acta - General Subjects* **372**, 345–357 (1974).
- <sup>250</sup>S. Belfer, Y. Purinson, and O. Kedem, “Surface modification of commercial polyamide reverse osmosis membranes by radical grafting: An ATR-FTIR study”, *Acta Polymerica* **49**, 574–582 (1998).
- <sup>251</sup>J. A. Alkrad, Y. Mrestani, D. Stroehl, S. Wartewig, and R. Neubert, “Characterization of enzymatically digested hyaluronic acid using NMR, Raman, IR, and UV–Vis spectroscopies”, *Journal of Pharmaceutical Biomedical Analysis* **31**, 545–550 (2003).
- <sup>252</sup>Q. Wang, L. Ren, C. Xu, Z. Zhai, J.-a. Zhou, Y. Yao, H. Xia, and Y. Wang, “Synthesis and characterization of glucosamine modified poly(ethylene glycol) hydrogels via photopolymerization”, *Journal of Applied Polymer Science* **128**, 89–96 (2013).
- <sup>253</sup>X. Chen, Y. Liu, F. M. Kerton, and N. Yan, “Conversion of chitin and N-acetyl-D-glucosamine into a N-containing furan derivative in ionic liquids”, *RSC Advances* **5**, 20073–20080 (2015).

- <sup>254</sup>Y. Ji, X. Yang, Z. Ji, L. Zhu, N. Ma, D. Chen, X. Jia, J. Tang, and Y. Cao, “DFT-calculated IR spectrum amide I, II, and III band contributions of N-methylacetamide fine components”, *ACS Omega* **5**, 8572–8578 (2020).
- <sup>255</sup>S. Bonnin, F. Besson, M. Gelhausen, S. Chierici, and B. Roux, “A FTIR spectroscopy evidence of the interactions between wheat germ agglutinin and N-acetylglucosamine residues”, *FEBS Letters* **456**, 361–364 (1999).
- <sup>256</sup>K. H. Sizeland, K. A. Hofman, I. C. Hallett, D. E. Martin, J. Potgieter, N. M. Kirby, A. Hawley, S. T. Mudie, T. M. Ryan, R. G. Haverkamp, and M. H. Cumming, “Nanostructure of electrospun collagen: do electrospun collagen fibers form native structures?”, *Materialia* **3**, 90–96 (2018).
- <sup>257</sup>Y. Du, H. Zang, Y. Feng, K. Wang, Y. Lv, and Z. Liu, “Efficient catalytic system for converting N-acetyl-D-glucosamine into valuable chemical 3-acetyl-amino-5-acetylfuran”, *Journal Molecular Liquids* **347**, 117970 (2022).
- <sup>258</sup>T. Cebe, N. Ahuja, F. Monte, K. Awad, K. Vyavhare, P. Aswath, J. Huang, M. Brotto, and V. Varanasi, “Novel 3D-printed methacrylated chitosan-laponite nanosilicate composite scaffolds enhance cell growth and biomineral formation in MC3T3 pre-osteoblasts”, *Journal of Materials Research* **35**, 58–75 (2020).
- <sup>259</sup>C. Steinbeck and S. Kuhn, “NMRShiftDB—compound identification and structure elucidation support through a free community-built web database”, *Phytochemistry* **65**, 2711–2717 (2004).
- <sup>260</sup>E. Khor, H. Wu, L. Y. Lim, and C. M. Guo, “Chitin-methacrylate: Preparation, characterization and hydrogel formation”, *Materials* **4**, 1728–1746 (2011).
- <sup>261</sup>C.-H. Dang, C.-H. Nguyen, T.-D. Nguyen, and C. Im, “Synthesis and characterization of N-acyl-tetra-O-acyl glucosamine derivatives”, *RSC Advances* **4**, 6239–6245 (2014).
- <sup>262</sup>P. Kiefer, V. Hahn, M. Nardi, L. Yang, E. Blasco, C. Barner-Kowollik, and M. Wegener, “Sensitive photoresists for rapid multiphoton 3D laser micro- and nanoprinting”, *Advanced Optical Materials* **8**, 2000895 (2020).
- <sup>263</sup>A. Mauri, P. Kiefer, P. Neidinger, T. Messer, N. M. Bojanowski, L. Yang, S. Walden, A.-N. Unterreiner, C. Barner-Kowollik, M. Wegener, W. Wenzel, and M. Kozłowska, “Two- and three-photon processes in photoinitiators for 3D laser printing”, Preprint, <https://doi.org/10.21203/rs.3.rs-1797484/v1> (2022).
- <sup>264</sup>G. Rist, A. Borer, K. Dietliker, V. Desobry, J. P. Fouassier, and D. Ruhlmann, “Sensitization of  $\alpha$ -aminoketone photoinitiators: A time-resolved CIDNP and laser spectroscopy investigation”, *Macromolecules* **25**, 4182–4193 (1992).
- <sup>265</sup>D. Serien and S. Takeuchi, “Two-photon direct laser writing for proteinaceous microstructures with additional sensitizer”, *Journal of Laser Micro/Nanoengineering* **12**, 80 (2017).

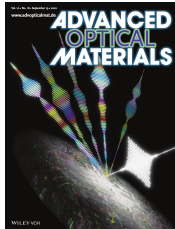
- <sup>266</sup>K. J. Schafer, J. M. Hales, M. Balu, K. D. Belfield, E. W. van Stryland, and D. J. Hagan, “Two-photon absorption cross-sections of common photoinitiators”, *Journal of Photochemistry and Photobiology A: Chemistry* **162**, 497–502 (2004).
- <sup>267</sup>J. Li, L. Qiu, C.-S. Poon, and U. Sunar, “Analytical models for time-domain diffuse correlation spectroscopy for multi-layer and heterogeneous turbid media”, *Biomedical Optics Express* **8**, 5518–5532 (2017).
- <sup>268</sup>M. Hohmann, M. Späth, D. Ni, D. Dörner, B. Lengenfelder, F. Klämpfl, and M. Schmidt, “Random laser as a potential tool for the determination of the scattering coefficient”, *Biomedical Optics Express* **12**, 5439–5451 (2021).
- <sup>269</sup>J. Y. Y. Loh, A. Mohan, A. G. Flood, G. A. Ozin, and N. P. Kherani, “Waveguide photoreactor enhances solar fuels photon utilization towards maximal optoelectronic–photocatalytic synergy”, *Nature Communications* **12**, 402 (2021).
- <sup>270</sup>L. Kassa-Baghdouche and E. Cassan, “Mid-infrared gas sensor based on high-Q/V point-defect photonic crystal nanocavities”, *Optical and Quantum Electronics* **52**, 260 (2020).
- <sup>271</sup>B. Zeng, Z. Cai, J. Lalevée, Q. Yang, H. Lai, P. Xiao, J. Liu, and F. Xing, “Cytotoxic and cytocompatible comparison among seven photoinitiators-triggered polymers in different tissue cells”, *Toxicology in Vitro* **72**, 105103 (2021).
- <sup>272</sup>M. Rothhammer, D. T. Meiers, M. Maier, G. von Freymann, and C. Zollfrank, “Initiator-free photo-cross-linkable cellulose-based resists for fabricating submicron patterns via direct laser writing”, *Journal of the Optical Society of America B* **40**, 849–855 (2023).
- <sup>273</sup>N. B. Cramer, J. P. Scott, and C. N. Bowman, “Photopolymerizations of thiol-ene polymers without photoinitiators”, *Macromolecules* **35**, 5361–5365 (2002).
- <sup>274</sup>A. S. Quick, J. Fischer, B. Richter, T. Pauloehrl, V. Trouillet, M. Wegener, and C. Barner-Kowollik, “Preparation of reactive three-dimensional microstructures via direct laser writing and thiol-ene chemistry”, *Macromolecular Rapid Communications* **34**, 335–340 (2013).
- <sup>275</sup>S. Grauzeliene, A. Navaruckiene, E. Skliutas, M. Malinauskas, A. Serra, and J. Ostrauskaite, “Vegetable oil-based thiol-ene/thiol-epoxy resins for laser direct writing 3D micro-/nano-lithography”, *Polymers* **13**, 872 (2021).
- <sup>276</sup>A. Bagheri and J. Jin, “Photopolymerization in 3D printing”, *ACS Applied Polymer Materials* **1**, 593–611 (2019).
- <sup>277</sup>O. C. J. Andrén and M. Malkoch, “Facile thiolation of hydroxyl functional polymers”, *Polymer Chemistry* **8**, 4996–5001 (2017).

## Publications

Parts of this thesis have been published in scientific journals and presented on international conferences and symposia. Related publications have been partly published in scientific journals as well.

### Publications in scientific journals (peer-reviewed)

- <sup>204</sup>R. C. R. Pompe\*, D. T. Meiers\*, W. Pfeiffer, and G. von Freymann, “Weak localization enhanced ultrathin scattering media”, *Advanced Optical Materials* **10**, 2200700 (2022).



- <sup>248</sup>D. T. Meiers\*, M. Rothhammer\*, M. Maier, C. Zollfrank, and G. von Freymann, “Utilizing the sensitization effect for direct laser writing in a novel photoresist based on the chitin monomer N-acetyl-D-glucosamine”, *Advanced Engineering Materials* **25**, 2201688 (2023).



- <sup>272</sup>M. Rothhammer\*, D. T. Meiers\*, M. Maier, G. von Freymann, and C. Zollfrank “Initiator-free photo-cross-linkable cellulose-based resists for fabricating submicron patterns via direct laser writing”, *Journal of the Optical Society of America B* **40**, 849–855 (2023).

- <sup>225</sup>D. T. Meiers and G. von Freymann, “Mixing rule for calculating the effective refractive index beyond the limit of small particles”, *Optics Express* **31**, 32067–32081 (2023).

---

\*these authors contributed equally

## Conference/symposium contributions as speaker

### Invited talks

D. T. Meiers, R. C. R. Pompe, W. Pfeiffer, M. Rothhammer, M. Maier, C. Zollfrank, and G. von Freymann, “Nature—an inexhaustible source of inspiration for materials and functional structures”, Symposium on the Honour of the 80th Birthday of Geoffrey Ozin, online (2023)

D. T. Meiers, R. C. R. Pompe, W. Pfeiffer, and G. von Freymann, “Effective refractive index determination and light propagation mechanisms in natural scattering media”, META 2023 (13th International Conference on Metamaterials, Photonic Crystals and Plasmonics), Paris, France (2023)

D. T. Meiers, M.-C. Heep, J. Hering, C. Jörg, J. Schulz, and G. von Freymann, “From structural color to brilliant whiteness—biomimetic photonic crystals with tailored disorder”, Symposium on Direct Write, Optical, Ion and Electron Beam Lithography, Klosterneuburg, Austria (2019)

### Talks

D. T. Meiers and G. von Freymann, “Novel mixing rule evaluating the effective refractive index beyond the restriction of very small sphere sizes”, DisoMAT 2023 (2<sup>nd</sup> International School and Conference on Disorder in Materials Science), Plankstetten, Germany (2023)

D. T. Meiers, M. Rothhammer, M. Maier, C. Zollfrank, and G. von Freymann, “Direct laser writing suitable resist based on the monomeric unit of chitin”, SPIE Photonics West 2023, San Francisco, USA (2023)

D. T. Meiers, R. C. R. Pompe, W. Pfeiffer, and G. von Freymann, “20% of brilliant white beetle scales’ reflectance via resonant coherent light scattering”, SPIE Photonics West 2022, San Francisco, USA (2022)

D. T. Meiers, R. C. R. Pompe, W. Pfeiffer, and G. von Freymann, “Manipulation of reflectance and photon lifetime distribution in strongly scattering structures by tailoring structural properties”, SPIE Photonics West 2021, online (2021)

D. T. Meiers, M.-C. Heep, and G. von Freymann, “A simple model mimicking the optical properties of white beetles”, DisoMAT 2019 (1<sup>st</sup> International School and Conference on Disorder in Materials Science), Postdam, Germany (2019)



## Related publications

### Peer-reviewed

<sup>25</sup>D. T. Meiers\*, M.-C. Heep\*, and G. von Freymann, “Invited article: Bragg stacks with tailored disorder create brilliant whiteness”, *APL Photonics* **3**, 100802 (2018).

### Others

<sup>95</sup>D. T. Meiers, “Entwicklung und Analyse eines grundlegenden Modells weißer Käferschuppen”, Diploma thesis (Technische Universität Kaiserslautern, 2018).

---

\*these authors contributed equally



# Curriculum vitae

## Education

2019–2023	<b>Doctoral studies</b> RPTU Kaiserslautern-Landau (formerly TU Kaiserslautern)
2013–2018	<b>Diploma in Physics (equiv. to M.Sc., graduated with honors)</b> Thesis title: “Entwicklung und Analyse eines grundlegenden Modells weißer Käferschuppen” TU Kaiserslautern
2005–2013	<b>Higher education entrance qualification (Abitur)</b> Hochwald Gymnasium Wadern

## Employment history

01/2020–11/2023	<b>Research fellow</b> RPTU Kaiserslautern-Landau
04/2019–12/2019	<b>Research assistant</b> TU Kaiserslautern
12/2017–03/2018	<b>Tutor</b> TU Kaiserslautern
06/2017–09/2017	<b>Research assistant</b> TU Kaiserslautern



## Acknowledgements

I would like to express my sincere thanks to all those who have contributed to the success of this work.

First of all, I would like to thank Prof. Georg von Freymann for making this thesis possible, for his always excellent support, for supervising my thesis, and for the many opportunities to present my work at conferences around the world. In addition, I would like to thank Prof. Artur Widera for taking time to co-refer my thesis.

A big thank you goes to all current and former members of the “AG Optische Technologien und Photonik” for the pleasant atmosphere, the many vivid discussions, the constant willingness to help, and the great time I spent with you. Further thanks go to Heike Buchinger for her excellent support in all bureaucratic matters and to Matthias Fischer, who is always on the spot when there is a technical problem to solve.

A big thank you also goes to all my collaborators with whom I have worked on various projects, in particular Ruben Pompe, Maximilian Rothhammer, Maximilian Maier, and the corresponding group leaders. Our fantastic cooperation was not only a lot of fun but has also contributed a lot to the success of this thesis.

I would also like to thank Ruben Pompe, Julian Schulz, Kristin Köhl, Max Rothhammer, and Malte Koster for the diligent proofreading of my work and the many helpful comments. In addition, I would like to thank the team of the Nanostructuring Center (NSC) at the RPTU Kaiserslautern-Landau for their support with SEM.

Last but not least, I would like to say a special thank you to my parents Robert and Astrid, my brother Marvin, and my fiancée Michelle for all your support, the countless good times, and being the counterbalance to the sometimes stressful everyday life.

Thank you all!